Physical interpretation of coarse-grained bead-spring models of complex fluids

by

Kirill Titievsky

Submitted to the Department of Chemical Engineering
in partial fulfillment of the requirements for the degree of

Doctor of Philosophy

at the

MASSACHUSETTS INSTITUTE OF TECHNOLOGY

February 2009

Author . . . .
Department of Chemical Engineering
Jan 14, 2009

Certified by . . . .
Gregory C. Rutledge
Lammot du Pont Professor of Chemical Engineering
Thesis Supervisor

Certified by . . . .
Paul I. Barton
Lammot du Pont Professor of Chemical Engineering
Thesis Supervisor

Accepted by . . . .
William M. Deen
Chairman, Department Committee on Graduate Theses

Physical interpretation of coarse-grained bead-spring models of complex fluids

by

Kirill Titievsky

Submitted to the Department of Chemical Engineering
on Jan 14, 2009, in partial fulfillment of the
requirements for the degree of
Doctor of Philosophy

Abstract

Bulk properties and morphology of block copolymers and polymer blends are highly sensitive to processing history due to small free energy differences among various stable and metastable states. Consequently, modeling these materials requires accounting for both thermal fluctuations and non-equilibrium processes. This has proven to be challenging with traditional approaches of energy minimization and perturbation in field theories. At the same time, simulations of highly coarse-grained particle-based models, such as lattice chain Monte Carlo and bead-spring simulations, have emerged as a promising alternative. The application of these methods, however, has been hampered by a lack of clear physical interpretation of model parameters.

This dissertation gives a rigorous interpretation to such coarse-grained models. First, a general thermodynamic approach to analyzing and comparing coarse-grained particle models is developed. Second, based on the analysis, a specific particle-based model is constructed so that it is unambiguously related to the standard Gaussian chain model and related field theories at realistic molecular weights. This model is complementary to field theoretic polymer simulations, which are computationally prohibitive for realistic molecular weights. Several applications of the model are demonstrated, including: fluctuation corrections to mean-field theories of block copolymers as well as a detailed investigation of the key effects governing the self-assembly of diblock copolymers confined in cylinders such as fibers or pores. The latter application introduces a novel impenetrable wall boundary model designed to attenuate effects of the walls on the total monomer density. The general approach and the specific models proposed here will find immediate application in modeling effects of flow, metastability, and thermal fluctuations on the morphology of complex fluids with molecular weights of $10^4 - 10^6$ g/mol using lattice and continuous space molecular simulations.

Thesis Supervisor: Gregory C. Rutledge
Title: Lammot du Pont Professor of Chemical Engineering

Thesis Supervisor: Paul I. Barton
Title: Lammot du Pont Professor of Chemical Engineering

Acknowledgments

This thesis is a culmination of efforts by many people. I am grateful more than I can say to:

Greg Rutledge for patiently trying and succeeding, despite my best efforts, in teaching me what I know about how science is done.

Ken Beers for teaching me to solve problems numerically.

Paul Barton for giving me a chance to be a part of his fantastic reseach group, as brief as my stay was.

Ed Feng for sympathyzing actively.

Erik Allen, Thierry Savin, Sam Ngai, Frederyk Ngantung for inspiration and company.

My grandmother, Dozya Titievsky, for letting me take my chances.

My grandfather, Aleksandr Tsitrin, for teaching me patience.

My gradmother, Dina Semenchyuk, for teaching me discipline.

My dad, Aleksey Titievsky, for making me curious.

My mom, Anna Titievskaya, for reminding me to stay human.

Rosemary, Leo, and Lola for being constant sources of happiness.

Contents

List of Figures

14

List of Tables

1

Introduction

1.1 Motivation

Common polymers blends and block copolymers self-assemble into heterogeneous and, in the case of block copolymers, periodic structures with dimensions between 10 nm and 1 μm. Consequently, these materials have many applications including plastics and rubbers with improved mechanical properties, barrier and conductive materials with non-isotropic properties, and electronic and photonic devices [7, 8].

Over the last twenty years, explicit simulation of systems of coarse-grained particle polymers (CGPP) have emerged as a promising approach to studying phase behavior and non-equilibrium properties of such complex polymer fluids. In these simulations, a polymer molecule is represented as 10 - 100 point masses connected by spring bonds and interacting through short-range potentials that describe the compressibility of the material and the miscibility of the component chemical species. CGPP simulation models include the classical lattice chain models as well as a number of continuous-space bead-spring models. By sacrificing all chemically-specific information, these models make it feasible to simulate cooperative phenomena that occur at the scale of hundreds to thousands of molecules and take anywhere from microseconds to weeks in real materials.

These phenomena in CGPP models are possible to simulate with relatively modest

computational resources. A number of researchers have investigated the phase behavior of various CGPP model block copolymers and homopolymer/polymer blends demonstrating many of the experimentally-observed complex ordered and metastable morphologies. In the case of diblock copolymers, the relative stability of the equilibrium phases in CGPP models have also been found to agree with experimental results under a wide range of compositions and relative miscibility of the components [9, 10]. CGPP model copolymers have also been shown to exhibit more subtle physically realistic features related to thermal fluctuations, such as stretching of diblock copolymers in super-critical (homogeneous) phases and an increase in critical Flory-Huggins miscibility parameter [11, 12]. CGPP simulations are also successful in non-equilibrium situations, as illustrated by the shear alignment of phase-segregated diblock copolymers observed in simulations of Guo and Kremer [13].

Despite these encouraging results, the practical applications of CGPP models are limited by the lack of a precise relationship between the model parameters and physical properties of specific materials. In particular, existing literature does not provide a systematic way to assign a molecular weight to the model polymers, nor are there rigorous quantitative ways to justify and select among the various non-bond interaction potentials used in these models. Yet, the ability to chose these model variables systematically is crucial since the material properties of polymer blends and block copolymers are known to be highly sensitive to the molecular weight. The rich variety of stable block copolymer morphologies means that small changes in composition, molecular weight, or temperature of a given block copolymer may cause an unwanted phase transition [14]. Furthermore, these materials are commonly trapped in metastable states due to the small differences between the free energies of the stable morphologies and slow relaxation kinetics [7, 8]. The nature of these metastable states is determined by shear, surface interactions, or other external influences necessary during manufacturing processes.

The alternative to explicit chain simulations in studying collective behavior in complex fluids are field theories based on the standard Gaussian chain model (GCM). The GCM formalizes the notion that molecular-scale features are independent of monomer structure by treating each molecule as the continous path of a random flight in a chemical potential field due to other polymers. While GCM is highly successful in many respects, quantifying effects of thermal fluctuations as well as modeling non-equilibrium situations with this approach has proven to be very challenging [15]. The approximations necessary to deal with these

problems complicate the interpretation of the disagreements between experimental data and the model, notably in composition and temperature dependence of the Flory-Huggins miscibility parameters [10, 16].

Thus, there is a need for a practical computational approach to sampling thermal fluctuations in polymers of realistic molecular weights in both equilibrium and potentially non-equilibrium simulations. While explicit chain simulations have been cited as the promising alternative [10, 15], there is a need for a systematic way of comparing the variety of these models in the current literature to each other and real polymers.

1.2 Objectives

This dissertation addresses this by pursuing three specific aims:

1. A clear systematic basis for comparing various CGPP models.

2. A CGPP model that is physically meaningful, reliable, and still practical.

3. An application showcasing and testing the theory and models developed above.

Achieving these aims will serve as the necessary initial step towards reliable particle-based models of complex fluids.

1.3 Approach

The central hypothesis of this work is that it is possible to express the parameters of a CGPP model precisely in terms of the standard Gaussian chain model. Block copolymers, rather than blends, become the focus of this dissertation because they are particularly convenient to simulate and pose some well-documented questions that have not been adequately answered by existing theories. The finite length scale and periodicity of the structure arising in these materials, due to the fact that the immiscible blocks are covalently connected, allows the simulations of phase transitions in these systems to be carried out with a relatively small number of molecules. At the same time, the nature of these correlations is known to broaden the critical region in these systems considerably, making not only energy minima but also thermal fluctuations important in determining the phase behavior.

1.4 Overview

The core of this dissertation consists of three studies, Chapters 3 – 5, that explore the phase behavior of blends of interacting particles, CGPP block copolymers, and block copolymers in cylindrical confinement. A more detailed overview of the background for this study, expanding on the topics mentioned in this introduction is also included in Chapter 2. The first half of this work, including 3 and 4 is focused on establishing the parametrization approach and developing and testing the simulation methodology. The second half of the thesis, including the end of 4 and Chapter 5 showcases the applications of the resulting simulation method.

Chapter 2 establishes the context for the following studies, including the specific challenges posed by block copolymers, by reviewing the advantages and shortcomings of the existing coarse-grained polymer models in some detail. The chapter discusses the standard Gaussian chain model (GCM), specific CGPP models, and ways in which they have been parametrized.

Chapter 3 is a study of blends of particles interacting through various potentials used in CGPP models, without considering bonds. The aim of this chapter is to express the phase behavior of these blends in the common terms of Flory-Huggins miscibility parameters and isothermal compressibility. This chapter identifies the major factors determining how the phase behavior of such blends depends on the choice of the interaction potentials and means for minimizing these differences. The key finding of this chapter is that the deviation of the phase diagram of these models from the Flory-Huggins mean field theory is mainly determined by the range of the interaction potentials relative to the particle spacing.

Chapter 4 generalizes and refines the above approach for block copolymers. In this chapter, the way in which bonds contribute to model-specific features of block copolymer phase behavior is examined in terms of the local and long-range correlations due to bonds. Based on these considerations, a computationally convenient bead-spring model that minimizes these model-specific features is constructed and compared in detail to experimental data and polymer field theories. The significance of these results is in demonstrating that a CGPP model may be constructed in a way that enables such direct comparisons to data on specific polymer systems.

Chapter 5 applies this block copolymer model to a detailed study of symmetric diblock

copolymer behavior in cylindrical confinement. The study is motivated by active experimental and theoretical work on the subject that revealed both intriguing and complex phase behavior and failure of standard approaches to describe some of the observations. The results showcase the importance of physically realistic parameter choices in detecting the finer features of phase behavior and explain some of the puzzling experimental observations.

All in all, these results comprise a cohesive CGPP simulation methodology that is firmly grounded in experimental data and the broader context of existing polymer theories. This claim and its implications for extending the modeling efforts described here to more sophisticated systems, including blends and non-equilibrium studies, are discussed in the concluding Chapter 7.

2

Background

Abstract

This chapter explores in detail current models of complex polymer fluids, mentioned in the Introduction. The focus is on clarifying the nature of the limitations of existing methods in order to highlight the opportunities and possible approaches to be pursued in this dissertation and subsequent work. While excellent qualitative results have been obtained, adequate treatment of thermal fluctuations remains the central challenge in the Gaussian chain models and uncertain physical interpretation remains the chief problem with explicit chain simulations.

2.1 Notation and conventions

In this work, k_B refers to the Boltzmann constant, and T to the thermodynamic temperature. Wherever $k_B T$ is not explicitly specified, it is assumed that the energy units are chosen so that $k_B T = 1$. "Density" is assumed to refer to number of objects per volume, unless otherwise noted. All coordinates are specified in three-dimensional real space. As usual, bold lower case letters indicate vectors $\mathbf{x} = (x_1, x_2, x_3)$.

2.2 The Gaussian chain model

The central idea of the most successful polymer models is that sufficiently long molecules may be studied without regard for their specific molecular structure. A concrete instance of

this idea that has been highly successful in modeling complex polymer fluids is the Gaussian chain model (GCM). In this section, the GCM is introduced briefly, largely on references [17, 18, 19], where the formal presentation of this material may be found. It solutions and the applicability to real polymer chains is then discussed informally.

2.2.1 Formal definition

Consider a system of n chains, each composed of $N \gg 1$ monomers, in a volume V and a temperature $k_B T$. Each monomer is point mass at a position, $\mathbf{x}_\alpha(t)$, where α is a chain index and t is the index of a monomer in a given chain. Let the set of all monomer coordinates be denoted Γ. Furthermore, different chemical species are identified by assigning a type label, $K_\alpha(t)$ which may be either A or B, to each monomer.

The free energy of the system of chains is composed of bond-related and non-bond, or excluded volume, interactions

$$\frac{U(\Gamma)}{k_B T} = U_b(\Gamma) + U_{nb}\left[\varrho_A(\mathbf{x}; \Gamma), \varrho_B(\mathbf{x}; \Gamma)\right] \tag{2.1}$$

The bonds between the particles are assumed to be harmonic springs so that the bond contribution is

$$U_b(\Gamma) = \sum_{\alpha=1}^{n} \sum_{i=2}^{N} \frac{3}{2a_0^2} (\mathbf{x}_\alpha(i) - \mathbf{x}_\alpha(i-1))^2 \tag{2.2}$$

The non-bond interactions are written in terms of density fields of each type of the monomer

$$U_{nb}[\varrho_A(\mathbf{x}; \Gamma), \varrho_B(\mathbf{x}; \Gamma)] = \frac{\zeta}{2\bar{\rho}} \int (\varrho_A + \varrho_B)^2 \, d\mathbf{x} + \frac{\chi}{2} \int \varrho_A \varrho_B \, d\mathbf{x} \tag{2.3}$$

where the integrals are carried out over the volume of the system, $\bar{\rho} = nN/V$, and explicit arguments of the density fields were dropped for brevity. The first term assigns energetic penalties to fluctuations in total density and the second term penalizes contacts between particles of different types. The scales of these energy penalties, ζ and χ, are referred to as the Helfand incompressibility parameter and the Flory-Huggins miscibility parameter [20], correspondingly.

2.2.2 Physical reasoning behind GCM

GCM makes sense as a description of a real polymer chain if each monomer corresponds to a very long section of a real chain. Consider such a long polymer segment, made up of N' chemical repeat units. Let the microstate of this chain segment be defined by a Γ_i be the set of coordinates describing the (microstate) of this chain section. Also, let the macroscopic state of the chain section be given in terms of the following thermodynamic variables: the position of its first monomer in space, $\mathbf{x}_j$; its end-to-end vector, pointing from the first to the last monomer, $\mathbf{r}$, and the energy associated with non-bond interactions of this chain, μ_i.

If $N' \gg 1$, we may treat the chain as a macroscopic system in the sense that the thermodynamic variables associated with it have small normally distributed fluctuations with a standard deviation proportional to $\sqrt{N}$ and much smaller than the mean values [21]. In a fluid where the chain is highly mobile, we expect the average end-to-end vector, $\langle \mathbf{r}_i \rangle \to 0$, corresponding to the probability distribution

$$P(\mathbf{r}_\alpha(i)) \approx \left(\frac{3}{2a_0^2 N'} \right)^{3/2} \exp\left(-\frac{3}{2} \frac{\mathbf{r}_\alpha(i)^2}{a_0^2 N'} \right) \quad \text{for} \quad N' \gg 1 \tag{2.4}$$

Note that this is as standard result for random walk models of polymers, where a_0 is known as the Kuhn, or statistical, segment length [19]. This immediately explains the Harmonic spring bond model used in Eq. 2.2.

Similar logic may be applied to the free energy associated with non-bond interactions. When a chain consists of only a few monomers, each monomer will interact with others in an entirely different way, depending on the precise relative positions of the atoms in the system. However, when $N \gg 1$, the monomers of the chain sample greater and greater fraction of all possible relative conformations, and corresponding energies. Thus, the energy of the chain approaches an average value which in an isotropic fluid should depend only on the position of the chain, $\mathbf{x}_i$, and the macroscopic state of the system which is specified by the monomer density ρ and the temperature $k_B T$ in the canonical ensemble.

Thus, we may write μ_i as a function of local monomer density and temperature $\mu(\rho, k_B T)$. In a system where two types of monomer are allowed, μ_i depends on the density of each component: $\mu_i = \mu(\rho_A, \rho_B, k_B T)$. In GCM a particularly simple, linear form of $\mu(\rho_A, \rho_B, k_B T)$

is assumed. The energy of each monomer of type A is taken to be

$$\mu(\rho_A, \rho_B, k_B T) \frac{\bar{\rho}}{k_B T} = \zeta(\rho_A + \rho_B) + \chi \rho_B \tag{2.5}$$

Eq. 2.3 may be recovered from this expression by allowing the densities to vary with position and noting that the number of A monomers in a differential volume $\mathrm{d}\mathbf{x}$ at $\mathbf{x}$ is $\rho_A(\mathbf{x})\,\mathrm{d}\mathbf{x}$. (Note that the factor of $1/2$ before the first term in Eq. 2.3 is necessary to avoid double counting interactions.)

The fluctuations in μ_i should scales as the square root of the total number of other chains with which a given chain interacts. A variable commonly used to characterized this number is the dimensionless chain density, C, which is the average number of chains in the volume equal to the cube of the radius of gyration, R_g of a chain:

$$C = R_g^3 \frac{\bar{\rho}}{N} \tag{2.6}$$

where $\bar{\rho}$ is the volume and ensemble average monomer density. The standard deviation of fluctuations in μ_i, therefore, should scale as $\sqrt{C}$.

Overall, the GCM energy model corresponds to a situation where each molecule is so large that any section of it may be associated with a local environment which itself is a macroscopic thermodynamic system with well-defined state variables and small, Gaussian fluctuations. Under these conditions, the behavior of any polymer may be formulated in terms of variables that do not explicitly depend on the specific molecular structure of a molecule. In case of real molecules, this implies the limit of infinitely long molecules, but may be expected to hold approximately for finite molecular weights.

2.2.3 Evaluating the GCM model

The GCM partition function

Thermodynamic averages characterizing a macroscopic system are given by its partition function. In case of a GCM complex fluid, the partition function is defined as

$$\mathcal{Z}(\chi, \zeta) = \int \exp\left(-U_b(\Gamma) - U_{nb}[\varrho_A(\mathbf{x}; \Gamma), \varrho_B(\mathbf{x}; \Gamma)]\right)\,\mathrm{d}\Gamma \tag{2.7}$$

Notice that the ensemble average composition in the system may be inferred from the derivatives of $\mathcal{Z}$:

$$-\frac{\partial \mathcal{Z}}{\partial \chi} = \frac{1}{\bar{\rho}} \langle \varrho_A(\mathbf{x}; \Gamma) \varrho_B(\mathbf{x}; \Gamma) \rangle \tag{2.8}$$

$$-\frac{\partial \mathcal{Z}}{\partial \zeta} = \frac{1}{2\bar{\rho}} \langle (\varrho_A(\mathbf{x}; \Gamma) + \varrho_B(\mathbf{x}; \Gamma))^2 \rangle \tag{2.9}$$

In general, these equations do not specify a unique set of fields. To solve this problem, it is useful to consider a restricted partition function, where the system is sampled only over the states where some function, $f(\Gamma)$ of the microstate takes on the value ϕ:

$$\mathcal{Z}(\chi, \zeta, \phi) = \int \exp \left(-U_b(\Gamma) - U_{nb}[\varrho_A(\mathbf{x}; \Gamma), \varrho_B(\mathbf{x}; \Gamma)] \right) \delta(f(\Gamma) - \phi) \, d\Gamma \tag{2.10}$$

where δ is the Dirac function.

Mean field solution to GCM

The most common and successful approach to evaluating the partition function in many statistical mechanics problems, including the GCM, is to neglect thermal fluctuations and considering the mean-field limit. This assumption is the basis for the well-known self-consistent field theory (SCFT) of Helfand *et al.*[2, 20]. The solution may alternatively be seen as an analogue of ground-state approximations in quantum physics and minimum free energy solutions [17]. Strictly speaking, the approach applies in the limit $N \rightarrow \infty$ and corresponds to the limit of very large molecular weights in real polymers.

Specifically, it is assumed that the ensemble average density fields maybe used in place of instantaneous fields in the non-bond energy term in . Eq. 2.3:

$$U_{nb}[\varrho_A(\mathbf{x}; \Gamma), \varrho_B(\mathbf{x}; \Gamma)] = U_{nb}[\rho_A(\mathbf{x}), \rho_B(\mathbf{x})] \tag{2.11}$$

where

$$\rho_K(\mathbf{x}) = \langle \varrho_K(\mathbf{x}; \Gamma) \rangle \tag{2.12}$$

To avoid trivial constant composition solutions due to averaging of degenerate states differing by phase shift and orientation, the density fields may be assumed to have a specific form, such as a Fourier series with a fixed phase shift and symmetry [2].

The mean field assumption eliminates the dependence of the non-bond U_{nb} term on chain coordinates, Γ. Thus, the partition function of each chain may be evaluated independently. This reduces the problem to that of a random walk in an externally imposed field. For a system of identical block copolymer chains, for example, it may be shown that

$$\frac{\mathcal{Z}(\chi,\zeta)}{\mathcal{Z}(0,0)} = \left(\frac{1}{V}\int q(\mathbf{x},1)\,\mathrm{d}\mathbf{x}\right)^n \tag{2.13}$$

where the restricted single chain partition function, $q(\mathbf{x},t)$, is approximately given by the Fokker-Planck equation for $N \gg 1$

$$\frac{\partial q(\mathbf{x},t)}{\partial t} = \frac{a_0^2 N}{6}\nabla^2 q(\mathbf{x},t) - \left[\frac{N}{2\bar{\rho}}\sum_{K\in\{A,B\}}(\zeta + J_K(tN)\chi)\rho_K(\mathbf{x})\right]q(\mathbf{x},t) \tag{2.14}$$

with $q(\mathbf{x},0) = 0$ and $J_K(tN) = 1$ when the type of the (tN)-th monomer along the chain is not equal to K and zero otherwise. The derivation of this equation is analogous to the derivation of the Schr odinger's equation of a quantum particle from the path-integral formulation as described by Feynman [22]. With this approximation, equations 2.7 through 2.9 may be solved either iteratively, as in classical SCFT [2], or as a minimization problem [18].

The mean-field solution is found to be fully specified by the composition of the system, χN and ζN.

Thermal fluctuations

While mean field solutions are generally accurate, accumulating experimental and theoretical evidence indicates that in complex polymer fluids thermal fluctuations have significant effects [3, 17]. Two approaches have been used to account for the fluctuations in the partition function integral: low-order perturbation approximations [17] and numerical field theoretic simulation [18]. All these methods are based on the following formal means of decoupling individual chain partition functions from each other.

First, Eq. 2.7 is rewritten as a functional integral

$$\mathcal{Z}(\chi,\zeta) = \int \exp\left(U_b(\Gamma) - U_{nb}\left[\rho_A(\mathbf{x}),\rho_B(\mathbf{x})\right]\right)\prod_K \delta\left[\rho_K(\mathbf{x}) - \varrho_K(\mathbf{x};\Gamma)\right]\,\mathrm{d}\Gamma\mathrm{D}\rho_A\mathrm{D}\rho_B \tag{2.15}$$

where $\delta[f(\mathbf{x})]$ is a functional version of the Dirac function, that enforces the identify $f(\mathbf{x}) = 0$ pointwise for any argument function f. This decouples the integrals over the components of the individual chain, and the integration over Γ for a given trial set of fields $\rho_K(\mathbf{x})$ may be carried out the same way as in the mean field case.

Second, in order to actually perform the calculations δ functionals are then rewritten using their inverse Fourier transforms, which introduces a set of so called auxiliary fields, w_K:

$$\delta[f(\mathbf{x})] = \int \exp\left(-i \int f(\mathbf{x}) w_K(\mathbf{x}) \, \mathrm{d}\mathbf{x}\right) \mathrm{D}w_K \tag{2.16}$$

This allows the $\mathcal{Z}(\chi, \zeta)$ to be rewritten in the form of a functional integral over density and auxiliary fields, rather than chain coordinates

$$\mathcal{Z}(\chi, \zeta) = \int \cdots \int \exp\left(-H_e[w_A, w_B, \rho_A, \rho_B]\right) \mathrm{D}\rho_A \mathrm{D}\rho_B \mathrm{D}w_A \mathrm{D}w_B \tag{2.17}$$

where $H_e[\cdots]$ is an effective Hamiltonian the precise form of which is not essential for the present purposes. In practice, the integration over the density fields may be carried out analytically for GCM, simplifying the problem [18]. The effective Hamiltonian may then be sampled over the auxiliary fields numerically. Several algorithms to do this have been advanced by Fredrickson *et al.*[18, 23] and are known as field theoretic simulation (FTPS).

A number of studies evaluate this partition function by the saddle point method, which relies on expanding the effective Hamiltonian about its saddle point (or the mean-field , in this case) value up the first order term in some small parameter. As noted by Wang [17], the BLHF (Brazovskii-Leibler-Helfand-Fredrickson) theory and the latter correction by Barrat and Fredrickson [3], assume a convenient, although physically reasonable, form of the perturbation term. Wang offers a more general solution [17].

The small parameter in this case may be taken as some power of the inverse dimensionless chain density , $1/C^\nu$, $\nu > 0$ and C is the number of average number of chains per unperturbed $(\chi = 0)$ radius of gyration of a chain

$$C = (a_0\sqrt{N/6})^3 \frac{\rho}{N} = \frac{1}{6^{3/2}} a_0^3 \rho \sqrt{N} \tag{2.18}$$

Thus, for example, Fredrickson and Helfand show that fluctuation correction to the mean field critical value of the χ in symmetric diblock copolymers scales as $1/C^{2/3} \propto 1/N^{1/3}$ [24]

2.3 Explicit chain simulations

2.3.1 Definition and specific examples

Explicit chain simulation, including continuous space and lattice methods, rely on a polymer model very similar to GCM, with the biggest difference being that N is always finite and usually of order 10. Consider the same system as in Section 2.2.1: n chains, each composed of N monomers, in a volume V and a temperature $k_B T$. Each monomer is point mass at a position, $\mathbf{x}_\alpha(t)$, where α is a chain index and t is the index of a monomer in a given chain. Let the set of all monomer coordinates be denoted Γ. Furthermore, different chemical species are identified by assigning a type label, $K_\alpha(t)$ which may be either A or B, to each monomer.

The Hamiltonian of this system using three terms: bond interactions reflecting the molecular topology; homogeneous, or type-independent, non-bond interactions that reflect the compressibility of the system; and excess non-bond interactions that reflect the immiscibility of the two types of blocks:

$$H(\Gamma) = H_b(\Gamma) + H_h(\Gamma) + H_{AB}(\Gamma) \tag{2.19}$$

$$H_b = \sum_{(i,j)\in\mathbb{B}} f_b(r_{ij}/a_0) \tag{2.20}$$

$$H_h = \sum_{i,j\in\mathbb{I},i>j} \epsilon_h K(r_{ij}/\sigma) \tag{2.21}$$

$$H_{AB} = \sum_{i\in\mathbb{I}_A,j\in\mathbb{I}_B} \epsilon_{AB} K(r_{ij}/\sigma) \tag{2.22}$$

$$r_{ij} \equiv |\mathbf{x}_j - \mathbf{x}_i|$$

where $\mathbb{B}$ is the set of all unique pairs of indices of particles connected to each other by bonds; $\mathbb{I}$ is the set of all particle indices; and $\mathbb{I}_K$ is the set of indices of all the particles of type K; and a_0 is the characteristic bond length and σ is the range of the potentials. Further, the shape of the potentials is defined by the kernel function $K(r)$, assumed to be spherically symmetric and if the norm exists normalized so that $\int K(r) 4\pi r^2 \, dr = 1$.

Various methods are distinguished by the shape of the kernel, $K(r)$, and the specific bond model, $f_b(r)$. The model of Grest *et al.*[12] use the so called FENE bond model and

shifted Lennard-Jones kernel:

$$f_{b,FENE}(r) = \begin{cases} -\frac{k}{\ln}(1 - r^2) & \text{if } r \leq 1, \\ \infty & \text{if } r > 1. \end{cases} \tag{2.23}$$

$$K_{Grest}(r) = \begin{cases} -4(r^{-12} - r^{-6} + 1/4) & \text{if } r \leq r_c \\ 0 & r > r_c \end{cases} \tag{2.24}$$

Dissipative particle dynamics (DPD) simulations of Groot and Madden [9] rely on harmonic spring bonds and quadratic potentials:

$$f_b(r) = \frac{3}{2a_0}r^2 \tag{2.25}$$

$$K_{DPD}(r) = \frac{15}{2\pi r_c^3}(1 - x/r_c)^2 \quad \text{where} \quad x \in [0, r_c) \tag{2.26}$$

Schultz *et al.*use a more complicated model that combines hard core repulsion with a DPD-like square potential. Continuous space models are typically evaluated in canonical molecular dynamics simulations, although Monte Carlo sampling methods are equally applicable.

Lattice chain simulations may be seen, such as those in [10, 25, 26], as the bead-spring model in a discrete space of monomer positions. Generally, the kernel $K(r)$ in these simulations is a uniform distribution on a sphere, so that the potential values are the same for all interacting neighbors and bonds energies are chosen so that only extension beyond a coordination shell are too unlikely to count. The discontinuous nature of the space requires that a Monte Carlo algorithm be used to sample these systems. The advantage of such a formulation is both is that the phase space of positions is much smaller that the potentials take on only pre-determined values, considerably reducing the expense of the energy calculations. The central disadvantage of these methods are not possible to extend to non-equilibrium simulations in a straightforward way.

2.3.2   Single chain in mean field (SCMC) simulations

Recently, M uller *et al.*have posited that CGPP simulations described above may be seen as discretizations of the GCM model [27]. The theory, referred to as SCMC, rests on the the approximation of explicit definition of the instantaneous density fields in the GCM on

a grid of points $\{\mathbf{y}_i\}$:

$$\rho_K(\mathbf{y}_i)- = \sum_{j \in \mathbb{I}_K} W(\mathbf{y}_i - \mathbf{x}_j) \tag{2.27}$$

where W is some function that distributes the mass of the particle among the grid points. The excess non-bond interaction energy of the system may then be estimated as

$$H_{AB}(\Gamma) \approx \chi \bar{\rho} \int \rho_A(\mathbf{y}) \rho_B(\mathbf{y}) \mathrm{d}\mathbf{y} \tag{2.28}$$

where the integral is carried out approximately on the discrete grid. Whith this definition, the microstates Γ of the chains may be sampled by Monte Carlo methods and retain a direct connection to GCM.

M uller's work anticipates most of the ideas introduced in this dissertation. Methodologically, it is precisely the field-mediated method for estimating long-range contributions to electrostatic interactions in molecular simulations (with Ewald summations being the most famous of these methods). This approach has been described in detail by Hockney and Eastwood three decades ago [28].

While the instantanous value of $H_{AB}(\Gamma)$ maybe adequately estimated by M uller's method, the average properties may be dramatically affected by correlations in particle positions or, equivalently, density fields. This fact is neglected in M uller's approach, and more generally the methods described by Hockney and Eastwood, due to the adoption of the mean-field view. As the success of mean field theories indicates, this is often adequate in the case of block copolymers. However, as will be shown in the following chapters, one of the the key difference distinguishing various discrete representations of GCM is the treatment of local correlations among particles or, equivalently, in density fields. Therefore, as M uller *et al.*explicitly state, their approach is a means of approximationg the mean field version of GCM. The concern of this thesis is rigorous understanding CGPP without the mean-field assumptions.

2.3.3 Parametrization approaches

Aside from M uller's conceptual interpretation of CGPP as a discretization of mean-field GCM, two approaches have been taken to parametrize bead-spring models: bottom-up and top-down. The bottom-up approach is to associate the particle positions in the bead-spring

model to specific points on a specific molecular model. The interaction potentials may then be chosen to minimize the difference in some property, generally the pair correlation function between the exact and bead-spring model. The most general formulation of the bottom-up approach is the PRISM theory of Curro and Schweizer, [29, 30]. These authors derive an expression for the non-bond interaction potentials in terms of the generalized Ornstein-Zernike direct correlation functions under a closure assumption about the shape of either the potentials or the correlation functions. While this is a valid approach, it is not useful for our purposes since it does not identify general, model-independent features of models.

A simpler bottom-up approach, noted by Grest *et al.*[12] and Fried and Binder [11] is that

$$\chi \approx \frac{\epsilon_{AB}}{\bar{\rho}} \int K(r) g_{AB}(r) 4\pi r^2 \, \mathrm{d}r \tag{2.29}$$

where $g_{AB}(r)$ is the radial distribution function for A-B pairs of monomers. This, in fact, is the approach taken in this thesis. What makes this work necessary is that the authors do not systematically study the properties of the radial distribution function itself in any detail. Thus, Grest *et al.*[12] use the overall radial distribution function, measured without distinguishing particle types. Fried and Binder and all lattice chain simulation studies of blends and block copolymers to my knowledge follow Flory [1] in making a mean-field assumption in estimating the value of χ, which boils down to the same thing: $g_{AB}(r) = g_{AA}(r) = g_{BB}(r)$ regardless of the value of ϵ_{AB}.

The alternative, top-down approach is to adjust model parameters to match predictions macroscopic parameters from the GCM model. For example, Grest *et al.*[12] estimate the value of the Flory-Huggins χ parameter from the structure function in their bead-spring simulations by fitting it it to the mean-field ($\chi \to 0$) GCM scattering function related to χ by de Gennes. The approach taken by Groot *et al.* is to identify the critical value of ϵ_{AB} in a blend of disconnected monomers with the Flory mean-field prediction of $\chi_c = 2$ and assume that this value remains the same for polymers using the same ϵ_h and ϵ_{AB}.

2.4 Key results

2.4.1 Qualitative phase behavior

Mean-field GCM solutions have served as the foundation for our the current understanding of the thermodynamics of complex polymer fluids. Flory's original mean-field treatment of the lattice chain blends has since been confirmed to constitute the mean field solutions for GCM blends [17]. Edwards has applied the approach to the equilibrium properties of polymer solutions [31]. A number of SCFT studies of block copolymers culminated in a complete phase diagram of diblock copolymers by Matsen and Bates [2], which since held up to experimental test [32, 33]. The work work has since been significantly extended to homopolymer/polymer blends and other block copolymers [18, 23].

The phase diagram of diblocks and blends of lattice and continuous space explicit chain models has been explored in several studies, demonstrating overall agreement with SCFT along with significant discrepancies. Groot and Madden demonstrated the existence of all stable diblock phases predicted by SCFT, except the BCC symmetry, in 10 particle DPD diblocks with C 1. Vassiliev and Matsen have reported a detailed phase diagram of lattice diblocks that is qualitatively similar to the SCFT phase diagram [10]. These authors, however, do not observe the gyroid , citing finite-size and metastability problems. Also, spherical phases are not observed due to large thermal fluctuations.

Düchs *et al.*have studied the fluctuation-corrected phase diagram of diblock/homopolymer emulsions [34]. Dotera reports lattice chain simulations of triblock/homopolymer mixtures where transitions among three tricontinuous phase: gyroid, diamond, and primitive [25]. Simulations of diblock copolymers with small particle inclusions have been carried in hard-sphere diblocks by Schultz *et al.*[35] as well as mean-field GCM theory by Thompson *et al.*[36].

During the last several years, there has been a steadily increased interest in morphology of complex polymer fluids in confinement. Mean-field GCM calculations and experimental evidence indicated that confinement dramatically increases the number and variety of stable block copolymer morphologies [37]. The most extensive investigation of these morphologies has been performed using lattice chain MC simulations [38].

2.4.2   Quantitative features

In addition to the overall phase diagrams, several predictions of the details of the structure, either in as explicit fields or as structure factor are worth mentioning. Helfand *et al.*applied SCFT to study the interface widths in blends with some success [20]. Another innovation by Helfand and Wasserman was to introduce the narrow interphase approximation (NIA), which they used to study the variation in domain sizes with the Flory-Huggins miscibility parameter and chain length in block copolymers at strong segregation [39, 40, 41].

In the opposite limit, the application of the mean-field assumption to homogeneous (supercritical) blends and block copolymers resulted in explicit expressions for the scattering functions of these materials in terms of the Flory-Huggins χ parameter. The RPA structure functions are explicitly related to the Flory-Huggins χ miscibility parameter, and therefore, has served as the common approach to estimating this parameter in recent years [16]. Note that the main consequence of the mean-field assumption in this case is all the chains find themselves in a perfectly homogeneous environment and are not perturbed by the immiscibility of different components. These theories are referred to as the random phase approximation and were initially developed by de Gennes for blends [17].

The effects of fluctuations have been treated approximately in blends by, for example, Wang [17] and in block copolymers by the BLHF theory and Barrat and Fredrickson [3, 24]. Both theories have shown that the critical regime, where significant transient composition fluctuations are present, is significant in both blends and block copolymers. Both theories provide corrections to the RPA structure function. The Barrat-Fredrickson work in particular has accounted for the increase in the peak wavelength of the scattering function associated with chain stretching due transient composition fluctuation in diblocks [42] and observed in lattice chain simulations [11]. Unfortunately, Wang's results have not been systematically applied to interpretation of blend data.

2.5   Remaining problems and opportunities

2.5.1   Non-equilibrium simulations

The general consensus in the literature appears to be that the DPD method of Groot *et al.*is the most promising approach to non-equilibrium simulations of complex polymeric fluids [9, 18, 43]. This conclusion is mainly based on the fact that the DPD algorithm

conserves momentum precisely. Beyond this technically correct assertion, no systematic studies comparing rheology of DPD polymers to experimental data is available. Grest *et al.*also argue for the promise of their own approach, described above and demonstrate shear induced alignment of lamellar structure with the direction of shear in simulations of dumb-bell molecules ordered into a [12, 44]. Similar effects have been demonstrated by Fraaije *et al.*[45], who have proposed a scheme to couple a dynamic model to a mean-field GCM model. Aside from these proof-of-concept studies, the field of systematic non-equilibrium simulation of complex fluids is largely unexplored.

2.5.2 Inconsistencies in Flory-Huggins χ values

The central difficulty of applying the GCM is that measured χ values have been found to depend on the method of measurement, composition, and temperature. Typically, the range of variation in χ with these parameters is between 20-50%. For example, Flory summarizes measurements obtained through vapor pressure measurements for polymer blends where χ rises or falls with concentration [1]. Maurer *et al.*have systematically compred measurements of χ for blends and diblock copolymers of the same two components based on matching of RPA structure factors in blends and diblocks and from matching of BLHF and mean field critical points in diblocks [16]. Again, inconsistencies of order 10-20% were found. Because all of these methods rely on approximate treatment of fluctuation effects, it is not apparent if these result reflect a fundamental limitation of the GCM or artifacts of neglecting fluctuation corrections [10, 17].

Similar or more dramatic inconsistencies are observed when these theories are applied to explicit chain simulations. Grest *et al.*the between the estimate obtained a difference of roughly 25% in values of χ for a single simulation between the results obtained by fitting the RPA structure function to the simulation results and Eq. 2.29. Unfortunately, the authors do not elaborate on how this difference may be controlled.

Results are considerably worse in lattice and DPD simulations. DPD calculations reveal that the ratio between the critical values of the χ parameters between monomer blends and diblock copolymers is about four times the anticipated mean field values [9]. Similarly, the Matsen and Vassiliev [10] observe critical points in diblock copolymers several times the mean-field predictions. In both cases, the results may be explained by the extremely low chain density, $C \approx 1$, which should make the mean-field results uncertain for both blends

or diblock copolymers.

Thus, the uncertainty in the Flory-Huggins χ parameters in explicit simulation systems obtained with current methods cannot be reliably characterized beyond an order-of-magnitude estimate. The problem is compounded by smaller, but still significant inconsistencies in experimentally measured χ parameters. This calls for more rigorous treatment of fluctuations in both explicit chain simulations and GCM.

2.5.3 Difficulty in sampling fluctuations

A significant drawback of both the perturbation schemes (BLHF) and FTPS is that they are generally limited to chain densities much larger than common diblock copolymer systems. Typical experimental block copolymers have dimensionless chain densities $C \in (2, 10)$ [32, 33, 42, 46]. In the case of BLHF and the Barrat-Fredrickson perturbations treatments of diblocks, the approximations are rigorously justified only for C of order 10^4 or greater.

Due to computational restrictions, FTPS have only been demonstrated for $C > 10$ and in only by restricting fluctuations to two-dimensions [15, 18, 23]. In fact, the majority of reported FTPS simulations are limited to two-dimensional studies. The computational expense of these simulations also precludes rigorous treatment of the convergence in resolution (regularization).

In contrast, explicit chain simulation include fluctuations naturally. Therefore, with clearly defined parameters, they may provide a better means of sampling fluctuations.

2.5.4 Regularization

Functional integrals arising in field theories such as Eq. 2.17 are meaningful only over some well-defined space of functions. In practice, the set of possible functions is restricted to have wavelengths greater than a cutoff wavelength, σ. The process of introducing such a cutoff is referred to as regularization (or, often, renormalization). Fredrickson *et al.*have shown that the chemical potential in GCM in general diverges with as $\sigma \to 0$, while taking σ to be insufficiently small results in artifacts in composition profiles [18, 47].

In FTPS this is achieved implicitly by evaluating the field integrals on a finite grid [18]. In analytical perturbation schemes, the approach is to either keep the cutoff wavelength as an explicit parameter, as done by Wang [17] and [48], or sample fluctuations only over a minimal basis set, *e.g.*a single plane wave, as done in the BLHF theory [3]. The latter

approach, clearly, is particularly susceptible to artifacts of the specific assumptions of the regularization, as illustrated, for example, by the differences between the critical point predictions in BLHF and the Barrat-Fredrickson corrections [3].

While these difficulties may, in general, be avoided by systematic treatment of convergence in observable quantities with σ, the work of Fredrickson *et al.*[47] on a homopolymer solution in a θ-solvent is, to my knowledge, the only GCM study where this is actually done. Thus, regularization adds an additional source of uncertainty in GCM treatment of fluctuations, providing an additional incentive to develop rigorous parametrization of explicit chain simulations.

3

Mixtures of interacting particles with well-defined Flory-Huggins χ miscibility parameters

Abstract

This article proposes a systematic, quantitative treatment of the problem of associating a scalar Flory-Huggins-like χ parameter directly with the interaction potentials in a binary mixture of point particles. This work fulfills the need for a general, quantitative way to compare χ values in explicitly simulated ensembles of lattice and off-lattice polymer models with field theoretic calculations. Emphasis is placed on constructing particle models where χ is relatively well-defined. In general, χ is defined through pair correlation functions, whose thermal fluctuations are coupled to local average composition and composition gradients. This implies that χ is composition-dependent even in the simplest particle models. At the same time, by quantifying this effect, it is found that composition independent χ may be defined to within a few percent for cases where the range of the potential is large relative to the interparticle distance. An explicit formula for χ in terms of interaction potentials is given. (This chapter has been published as an article in the *Journal of Chemical Physics* [49].)

3.1   Introduction

Structure and miscibility of block copolymers and polymer blends are modeled using either field theories or explicit simulations of highly simplified polymers of interacting particles.

Both approaches have resulted in some excellent qualitative predictions of polymer behavior [3, 11, 18, 23, 50]. However, making reliable quantitative predictions remains difficult and is currently an area of significant interest [18]. Historically, polymer miscibility has been described in term of the Flory-Huggins χ parameter. This parameter is defined in the context of field theories of polymer fluids and is a measure of excess chemical potential due to unfavorable interactions between monomers of different types. Determination of χ in both real and simplified particle-based model polymer systems is a key challenge in the quantitative interpretation of model results.

The literature on the fundamental relationship between χ and microscopic properties of fluids is substantial, but fragmented and limited to providing estimates with significant uncertainties. First of all, there is some ambiguity in the meaning of χ within the field theoretic context. Originally, χ arose in a mean-field treatment of lattice fluids by Flory and Huggins and was later adopted in mean-field theories of the standard Gaussian chain model, namely, self-consistent field theory. Since the mean-field assumption in these theories corresponds to the limit of infinite molecular weight [18], the assumptions about local structure of the polymer become irrelevant. As a consequence, macroscopic definitions of thermodynamic quantities, such as particle density and chemical potentials, apply at all relevant length scales.

The same cannot be said of finite chains in explicit polymer simulations and, more recently, in generalized field theoretic polymer simulations (FTPS). For example, Vassiliev and Matsen point out that local lattice artifacts preclude a direct identification of χ in lattice chain and Gaussian chain models, which are the basis for FTPS [51]. Binder and Müller reach the same conclusion by pointing out that local composition fluctuations are expected to affect the validity of the Flory mean-field expression for lattice fluids in real simulations [52]. Finally, Wang shows that a careful treatment of the standard Gaussian chain model introduces significant renormalization corrections into the traditional field theoretic χ compared to the usual Flory-Huggins definition and de Gennes' random phase approximation (RPA) expression for structure factor, which is used to measure χ experimentally.

The situation is even less clear in off-lattice particle-based models. For example, Curro and Schweizer argue that a natural extension of the Flory mean field approach makes χ simply proportional to the norm of the excess interaction potential between monomers of different types [30]. This leads to an error in χ of an order of magnitude or more. The errors

are attributed to renormalization implicit in classic mean field theories and are discussed in a more general setting by Wang [17]. Grest *et al.* adopted a formula similar to Curro and Schweizer's, but with the excess potential reweighted by the monomer radial distribution function [12]. This accounts for the effect of correlations among particles and brings the expression in closer correspondence to the classic Flory-Huggins result, as recast by Muller *et al.*[52, 53]. As a result of this renormalization, the difference between predicted and measured χ is only about 25% in the model system studied by Grest *et al.*While this is a significant improvement, the authors point out that their expression for χ is only a lower bound and perform no further error analysis.

The most sophisticated method of obtaining χ values from microscopic considerations is based on the PRISM theory of Curro and Schweizer [29, 30]. These authors derive an expression for χ in terms of the generalized Ornstein-Zernike direct correlation functions under a number of approximations, including the random phase approximation (RPA). This expression, however, is of limited use for quantitative prediction of scalar χ parameters. Firstly, PRISM predicts a wavelength-dependent, rather than scalar, χ. Secondly, it is difficult to asses the quantitative implications of the model assumptions, particularly RPA and the closure approximation. Moreover, these assumptions complicate extrapolation, particularly for block copolymers where the RPA breaks down under experimentally important conditions [42]. Finally, the theory does not predict the correlation functions themselves.

This article focuses on clarifying the relationship between potentials in simple particle-based models and the χ parameter used in standard polymer field theories. The primary motivation for this study is an attempt to construct a coarse-grained particle based model of block copolymers that could be unambiguously compared to field theoretic results on finite chains. Also, isolating the factors determining whether χ is a constant should improve our understanding of the non-trivial dependence of experimentally measured χ parameters on thermodynamic state variables. Specifically, the goal is to obtain a class of particle models where χ parameters are well-defined scalar constants, insensitive to composition and temperature. Moreover, χ should be given quantitatively by a simple expression in terms of the particle interaction potentials. Understanding the conditions required for such a simple definition to hold is the key result of this paper.

In order to avoid the cascade of approximations that complicates matters in the studies above, a very direct approach is adopted here. A binary mixture of particles distinguished

only by labels, A and B, and penalty potentials for AB interaction is considered. First, the χ is explicitly defined using a standard field theoretic formula for the excess energy of interactions between two unlike particles. Next, the same excess energy is written as an ensemble average of the Hamiltonian of a particle system over all particle coordinates consistent with a given set of density fields. The conditions required for this ensemble average to reduce to the field theoretic form are characterized. Under these conditions, χ is readily identified. The accuracy of the resulting expression for χ is tested by comparing binary coexistence curves for a number of lattice and off-lattice model mixtures. Finally, the implications for experimental measurement of χ and for construction of particle-based models, as well as connections to the literature mentioned above, are discussed.

3.2 Background and definitions

All energies are expressed in the units of $k_B T$, the Boltzmann constant multiplied by the thermodynamic temperature. Averages of functions over the system volume are denoted by a bar over the function symbol. For example, $\bar{\rho}$ is the bulk average density. Bold letters are used for position vectors in three-dimensional space and corresponding italic symbols for the magnitudes of these vectors, *e.g.* $r = |\mathbf{r}|$.

The particle system considered here consists of n point particles of identical mass, m, in a fixed volume V at a constant temperature T. A particle may be of either type A or B. The position of particle i is denoted as $\mathbf{x}_i$ and symbol Γ is used as a short hand for coordinates of all the particles in the system. The Hamiltonian of the system consists of homogeneous and heterogeneous parts. The homogeneous part, $H_h(\Gamma)$ is independent of particle types, while the heterogeneous part, $H_{AB}(\Gamma)$, is the extra energy penalty due to interactions among particles of different types. Both parts are given in terms of spherically symmetric pair potentials

$$H(\Gamma) = H_h(\Gamma) + H_{AB}(\Gamma) \tag{3.1}$$

$$H_h(\Gamma) = \frac{1}{2} \sum_{i,j \in \mathbb{I}} u_h(r_{ij}) \tag{3.2}$$

$$H_{AB}(\Gamma) = \sum_{i \in \mathbb{I}_A} \sum_{j \in \mathbb{I}_B} u_{AB}(r_{ij}) \tag{3.3}$$

$$r_{ij} \equiv |\mathbf{x}_i - \mathbf{x}_j| \tag{3.4}$$

44

Here, $\mathbb{I}$ is the set of indices of all the particles, while $\mathbb{I}_K$ is the set of indices of all particles of type K.

In the field representation of the system, the state variables are number density fields of the particles of different types, $\rho_A(\mathbf{x})$ and $\rho_B(\mathbf{x})$, specified for all points $\mathbf{x}$ in the system volume. The homogeneous interactions are assumed to be sufficiently strong that the system is incompressible [18, 20]

$$\rho_A(\mathbf{x}) + \rho_B(\mathbf{x}) = \bar{\rho} \equiv n/V \tag{3.5}$$

The field theoretic analogue of the heterogeneous part of the Hamiltonian is given as a functional of the density fields,

$$U_{AB}[\rho_A, \rho_B] = \frac{\chi}{\bar{\rho}} \int \rho_A(\mathbf{x})\rho_B(\mathbf{x})\,\mathrm{d}\mathbf{x} \tag{3.6}$$

where χ is the field theoretic analogue of the Flory-Huggins parameter. $U_{AB}[\rho_A, \rho_B]$ is an average of $H_{AB}(\Gamma)$ over all arrangements of particles consistent with the given density fields, ρ_A and ρ_B. Now Equation 3.6 may be used as the definition of χ for the present purposes, assuming that $U_{AB}[\rho_A, \rho_B]$ is calculated independently, $e.g.$directly in the particle model. It turns out to be convenient to use the perfectly homogeneous system as the reference state, since it is the deviation of the system from this state that is of interest. Therefore, the following definition is adopted

$$\chi \equiv \bar{\rho} \frac{U_{AB}[\rho_A, \rho_B] - U_{AB}[\bar{\rho}_A, \bar{\rho}_B]}{\int (\rho_A(\mathbf{x})\rho_B(\mathbf{x}) - \bar{\rho}_A\bar{\rho}_B)\,\mathrm{d}\mathbf{x}} \tag{3.7}$$

The rest of this paper is devoted to obtaining a simple expression for $U_{AB}[\rho_A, \rho_B]$ directly from the particle model and to understanding the properties of the result.

3.3 Theory

3.3.1 Connecting field and particle models

Obtaining an explicit expression for $U_{AB}[\rho_A, \rho_B]$ directly from the particle system Hamiltonian, $H(\Gamma)$, requires two definitions. First, a density field $\rho_K(\mathbf{x})$ must be obtained in terms of the particle coordinates and, second, a mechanism for averaging $H_{AB}(\Gamma)$ only over Γ consistent with a given set of fields must be formalized.

Let the function $\varrho_K(\mathbf{x}; \Gamma)$ associate density fields with instantaneous particle coordinates, Γ. In FTPS literature it is customary to use the "exact" density field

$$\varrho_K^*(\mathbf{x}; \Gamma) = \sum_{i \in \mathbb{I}_K} \delta(\mathbf{x}_i - \mathbf{x}) \tag{3.8}$$

The asterisk identifies this particular definition of $\varrho_K(\mathbf{x}; \Gamma)$. Unfortunately, this definition makes it impossible to attain exact equality between $\varrho_K(\mathbf{x}; \Gamma)$ and any smooth $\rho_K(\mathbf{x})$. Thus, sampling smooth density fields requires additional renormalization. Theoretical foundations and algorithms for doing this are matter of current research [18, 47].

This difficulty may be avoided by defining $\varrho_K(\mathbf{x}; \Gamma)$ to be smooth. One way to accomplish this is to convolve the exact density field with a smoothing function $W(\mathbf{x}; s)$:

$$\varrho_K(\mathbf{x}; \Gamma) \equiv \varrho_K^*(\mathbf{x}; \Gamma) * W(\mathbf{x}; s) = \sum_{i \in \mathbb{I}_K} W(\mathbf{x}_i - \mathbf{x}; s) \tag{3.9}$$

The smoothing function may be any proper probability density distribution whose width is characterized by the parameter s. In effect, the above convolution is a generalization of a simple frequency cutoff, with s corresponding to the cutoff wavelength. The smoothing function is generally an arbitrary object, whose choice should not influence the macroscopic predictions of the model. Before discussing a definition of the smoothing further, however, it is important to clarify its role in the model.

The above definition of the density fields allow $U_{AB}[\rho_A, \rho_B]$ to be written explicitly as an ensemble average of $H_{AB}(\Gamma)$:

$$U_{AB}[\rho_A, \rho_B] = \left\langle H_{AB}(\Gamma) \prod_{K=A,B} \delta[\rho_K(\mathbf{x}) - \varrho_K(\mathbf{x}; \Gamma)] \right\rangle_\Gamma \tag{3.10}$$

$$\langle f(\Gamma) \rangle_\Gamma \equiv \frac{\int f(\Gamma) \exp[-U(\Gamma)] \, d\Gamma}{\int \exp[-U(\Gamma)] \, d\Gamma} \tag{3.11}$$

$$\delta[f(\mathbf{x})] \equiv \delta\left(\int f(\mathbf{x})^2 \, d\mathbf{x} \right) \tag{3.12}$$

Here, $f(\mathbf{x})$ and $f(\Gamma)$ indicate any scalar real functions of the corresponding arguments and $\delta[f(\mathbf{x})]$ is the functional version of the Dirac δ function used to enforce equality between two fields. (See [18] for a slightly different definition of the δ functional.) Thus, the δ functionals restrict the ensemble to only those Γ that are consistent with the given density

46

fields $\rho_A(\mathbf{x})$ and $\rho_B(\mathbf{x})$. Now, χ may be calculated, at least in principle, by substituting the above expression for $U_{AB}[\rho_A, \rho_B]$ into Equation 3.7.

Before attempting any calculations of χ, however, it is useful to recast the energy expression in a way that separates contributions of long and short range fluctuations in component density fields. Consider rewriting $H_{AB}(\Gamma)$ as

$$H_{AB}(\Gamma) \equiv \int \varrho_A^*(\mathbf{x}; \Gamma) \varrho_B^*(\mathbf{x}+\mathbf{r}; \Gamma) u_{AB}(\mathbf{r}) \, d\mathbf{x} \, d\mathbf{r} \tag{3.13}$$

$$= \int \varrho_A(\mathbf{x}; \Gamma) \varrho_B(\mathbf{x}+\mathbf{r}; \Gamma) G_{AB}(\mathbf{x}, \mathbf{r}; \Gamma) u_{AB}(\mathbf{r}) \, d\mathbf{x} \, d\mathbf{r} \tag{3.14}$$

Here an *instantaneous pair density function*, $G_{AB}(\mathbf{x}, \mathbf{r}; \Gamma)$, is introduced

$$G_{AB}(\mathbf{x}, \mathbf{r}; \Gamma) = \frac{\varrho_A^*(\mathbf{x}; \Gamma) \varrho_B^*(\mathbf{x}+\mathbf{r}; \Gamma)}{\varrho_A(\mathbf{x}; \Gamma) \varrho_B(\mathbf{x}+\mathbf{r}; \Gamma)} \tag{3.15}$$

Thus, $G_{AB}(\mathbf{x}, \mathbf{r}; \Gamma)$ captures the small wavelength information about particle positions, extracted from the density fields $\varrho_K(\mathbf{x})$ by the frequency cutoff in Equation 3.9.

Now Equation 3.10 allows the explicit dependence of the integrand on particle coordinates, Γ, to be isolated in the pair density function:

$$U_{AB}[\rho_A, \rho_B] = \int \rho_A(\mathbf{x}) \rho_B(\mathbf{x}+\mathbf{r}) G_{AB}(\mathbf{x}, \mathbf{r}) u_{AB}(\mathbf{r}) \, d\mathbf{x} \, d\mathbf{r} \tag{3.16}$$

$$G_{AB}(\mathbf{x}, \mathbf{r}) = \left\langle G_{AB}(\mathbf{x}, \mathbf{r}; \Gamma) \prod_{K=A,B} \delta[\rho_K(\mathbf{x}) - \varrho_K(\mathbf{x}; \Gamma)] \right\rangle_\Gamma \tag{3.17}$$

Here, $G_{AB}(\mathbf{x}, \mathbf{r})$ is the ensemble average pair density (referred to as simply "pair density" from here on). Thus, the pair density will become a central object of study in this article.

Physically, $G_{AB}(\mathbf{x}, \mathbf{r}) \rho_B(\mathbf{x})$ corresponds to the density of B particles at $\mathbf{x}+\mathbf{r}$ given that the density of B and A particles at $\mathbf{x}$ is $\rho_B(\mathbf{x})$ and $\bar{\rho} - \rho_B(\mathbf{x})$, respectively. Thus, $G_{AB}(\mathbf{x}, \mathbf{r})$ reflects local correlations among particles, while the smooth density fields describe the long range ones. It is crucial to note that $G_{AB}(\mathbf{x}, \mathbf{r})$ contains only the high frequency Fourier components regardless of the long range structure in the system.

The last issue to resolve before the above Equation 3.16 is complete is to define the smoothing function, $W(\mathbf{x}; s)$. A particularly convenient definition is implicit: $W(\mathbf{x}; s)$ is such a function that makes $G_{AB}(\mathbf{x}, \mathbf{r})$ be equal to the pair density function in a pure system (or one with $u_{AB}(r) = 0$) measured without any frequency cutoff. Mathematically this is

expressed as

$$G_{AB}(\mathbf{x}, \mathbf{r}) = \lim_{u_{AB}(r) \to 0} \left\langle \frac{\varrho_A^*(\mathbf{x})\varrho_B^*(\mathbf{x}+\mathbf{r})}{\bar{\rho}_A \bar{\rho}_B} \right\rangle_\Gamma \qquad (3.18)$$

Defined this way, $G_{AB}(\mathbf{x}, \mathbf{r})$ captures all interparticle correlations in homogeneous and pure systems. More generally, the penalty potential, $u_{AB}(r)$, is assumed to manifest itself only in composition variations at the length scale much longer than the length scale of interparticle correlations in pure systems. This means that locally, the interparticle correlations are assumed to be dominated by the homogeneous potential, $u_h(r)$, and unperturbed by $u_{AB}(r)$. Thus, the contributions of density correlations characteristic of pure systems are contained in $G_{AB}(\mathbf{x}, \mathbf{r})$ and isolated from any effects of the penalty potential, $u_{AB}(r)$. This is the same sort of separation of the two contributions to $U_{AB}[\rho_A, \rho_B]$ used in the renormalization scheme proposed by Alexander-Katz *et al.*in the context of FTPS [47].

In general, $u_{AB}(r)$ may very well change both the local and long range structure of the fluid. In this case, however, the very notion of a coarse-grained model that considers only the long-range properties of the system is suspect. Therefore, Equation 3.18 is consistent with the intuition behind the notion of χ as well as smooth density fields (*i.e.* that pure systems and ideal mixtures are characterized by constant component densities). The form of $W(\mathbf{x}; s)$ this equation implies may depend on $u_{AB}(r)$ and, hence, local composition. However, this is a limitation of the broader idea of decoupling the long and short range structure separately, rather than of this particular definition.

While actually calculating this version of $G_{AB}(\mathbf{x}, \mathbf{r})$ is elementary in simulations, an equivalent measurement may be impossible in real systems. For the case where each particle represents a section of a polymer chain, the $\epsilon_{AB} = 0$ state may be possible to estimate by reducing the molecular weight of whole chains and so increasing the translational entropy, leading to effective homogenization.

Finally, with the smoothing function, $W(\mathbf{x}; s)$, defined, Equation 3.16 may be used to calculate χ corresponding to any given particle model directly. For example, $U_{AB}[\rho_A, \rho_B]$ along with the density fields themselves may be measured in a molecular dynamics simulations and results substituted into Equation 3.7. Measuring χ at a single set of conditions using such a procedure is, however, of limited use since it does not guarantee that the results may be extrapolated to other conditions. Therefore, the following sections focus on simplifying Equation 3.7 and characterizing the conditions under which it allows straightforward

extrapolation of χ from simple calibration experiments to more complex systems.

3.3.2   Composition independent χ

The field energy in Equation 3.10 is particularly simple under two assumptions: (1) macroscopic composition variations occur on a sufficiently large scale that $\rho_B(\mathbf{x} + \mathbf{r}) \approx \rho_B(\mathbf{x})$ wherever $u_{AB}(\mathbf{r})$ is appreciable; (2) differences between particle types do not affect local correlations, making $G_{AB}(\mathbf{x}, \mathbf{r})$ entirely independent of the local composition. In this section, the implications of these assumptions are considered, while the next is dedicated to the consequences of relaxing them.

The second assumption allows $G_{AB}(\mathbf{x}, \mathbf{x} + \mathbf{r})$ to be replaced by its volume average, $\bar{G}_{AB}(\mathbf{r})$ carried out at any composition, including a pure system. Together with the first, this neatly transforms Equation 3.10 into the form of Equation 3.6:

$$U_{AB}[\rho_A, \rho_B] = \int \bar{G}_{AB}(\mathbf{r}) u_{AB}(\mathbf{r}) \mathbf{r} \, d\mathbf{x} \, d\mathbf{r} \int \rho_A(\mathbf{x}) \rho_B(\mathbf{x}) \, d\mathbf{x} \tag{3.19}$$

$$\bar{G}_{AB}(\mathbf{r}) \equiv \frac{1}{V} \int G_{AB}(\mathbf{x}, \mathbf{r}) \, d\mathbf{x} \tag{3.20}$$

This allows χ to be immediately identified as

$$\chi = \bar{\rho} \int \bar{G}_{AB}(\mathbf{r}) u_{AB}(\mathbf{r}) \, d\mathbf{r} \tag{3.21}$$

or, for systems with spherically symmetric interactions,

$$\chi = \bar{\rho} \int g(r) u_{AB}(r) 4\pi r^2 \, dr \tag{3.22}$$

where $g(r)$ is just the radial distribution function for a pure system.

The importance of this expression is that it is purely microscopic. More precisely, it yields χ that is independent of composition. Moreover, this is precisely the formula used by Grest *et al.*as a lower bound for χ in off-lattice simulations [12]. Moreover, Muller *et al.*show that this reduces precisely to the Flory-Huggins mean field expression for lattice fluids [52, 53]. Therefore, the case case considered in this section is a generalization of the Flory-Huggins mean-field approximation. The following section relaxes this approximation.

49

3.3.3   Dependence of χ on composition

Recall that the composition-independent Equation 3.21 for χ obtained in the previous section relies on neglecting dependence of the pair correlation function on composition as well as the composition gradients. These assumptions are relaxed in this section, leading to composition dependence of χ. This analysis is a key contribution of this paper.

Composition dependence of $G_{AB}(\mathbf{x}, \mathbf{r})$

There are two qualitatively different ways in which the pair density, $G_{AB}(\mathbf{x}, \mathbf{r})$, and therefore χ, may be coupled to the local average composition, expressed by the density fields $\rho_A(\mathbf{x})$ and $\rho_B(\mathbf{x})$. First, the penalty potential, $u_{AB}(r)$, may strongly affect the volume average $\bar{G}(\mathbf{x})$; second, it may affect fluctuations in $G_{AB}(\mathbf{x}, \mathbf{r})$ about the average.

One condition under which $\bar{G}_{AB}(\mathbf{r})$ is affected by the composition is for $u_{AB}(r)$ to be comparable to $u_h(r)$. Immiscible small molecule liquids are examples where $u_{AB}(r)$ must be comparable to $u_h(r)$ to cause phase segregation despite the high translational entropy. This, of course, does not have to be the case in model fluids. More importantly, this does not have to be the case for particles representing large sections of macromolecules. In this case, phase segregation may be achieved with much lower $u_{AB}(r)$ since polymerization dramatically lowers the translational entropy. In fact, this property of polymer systems is precisely what has made coarse-grained models so successful.

Another situation where the pair density function inextricably depends on composition is if the A and B particles are distinguished only by the particle type label and penalty potential, $u_{AB}(r)$. This may include a difference in mass or a difference in AA and BB homogeneous potentials. This is a particularly important case since even the mean field χ becomes dependent on composition. Moreover, real molecules nearly always differ geometrically. In a simple particle model considered here, however, asymmetry is eliminated by definition, and effects of the penalty potential $u_{AB}(r)$ on local correlations may be mitigated by choosing $u_h(r) \gg u_{AB}(r)$.

Decoupling the AB radial distribution function from the composition is not sufficient for the fluctuations in the radial distribution function, $G_{AB}(\mathbf{x}, \mathbf{r}) - \bar{G}(\mathbf{r})$, to be independent of the composition. The importance of fluctuations has been recognized qualitatively (*e.g.*appendix of [52]), but not studied systematically. Systematic understanding of these

fluctuation effects is essential for mitigating the corresponding uncertainty in χ.

For simplicity, consider a symmetric AB Flory-Huggins lattice fluid mixture, essentially corresponding to a crystal where the magnitude of $u_h(r)$ is sufficiently high to overcome thermal fluctuations. $U_{AB}(\Gamma)$ in this case is strictly a function of the number of AB interactions. If $\epsilon_{AB} \to 0$ and the particle labels are assigned at random, the mean field approximation must evidently apply. Introducing an energy penalty for interactions must necessarily shift the average number of AB interactions below the mean field limit, reducing the exact χ in Equation 3.7 below the mean field estimate of Equation 3.21.

Note that as the concentration of A particles decreases, AA contacts become increasingly rare as each A particle is surrounded by B particles. Therefore, the lower the concentration of the minority component, the less the fluctuations affect the number of AB contacts per minority component particle. Consequently, the decrease in $U_{AB}[\rho_A, \rho_B]$ per A particle is greater for more symmetric mixtures. As a consequence, thermal fluctuations in the pair density function stabilize concentrated phases with respect to dilute ones. This is consistent with the finding that fluctuations increase the effective χ parameter required to achieve phase segregation in model polymer systems, including the standard Gaussian chains [17, 24].

Thus, thermal fluctuations in pair density lead to composition dependence of χ even for the simplest lattice fluids of entirely symmetric particles. Attenuating these fluctuations requires a large number of interactions per particle. In real systems, this corresponds to a particle that represents a long polymer and in model systems potentials with ranges large relative to the average interparticle spacing. Determining just how large the range of these potentials must be and, ultimately, whether the fluctuations may be attenuated is a task for numerical simulations, described later in the text.

Non-local effects

The other assumption necessary for Equation 3.21 to hold is that the variations in smooth density fields may be neglected at the scale comparable to the range of the interaction potential. This is unjustified in at least two important cases: moderately and weakly segregated block copolymers and polymer interfaces. While Helfand and Tagami [20] conclude that the non-local effects are often negligible if the local scale is taken to be comparable to the size of the chemical repeat unit, this argument may not stand for coarse-grained models

where each chain is represented by a relatively small number of particles.

To simplify the analysis of the effect, assume that $G_{AB}(\mathbf{x}, \mathbf{r})$ is statistically independent from composition and spherically symmetric. Therefore, it may be replaced by a radial distribution function $g(r)$ in Equation 3.10. In Appendix 3.7.1, it is shown that by introducing a Taylor expansion of the density fields in $\mathbf{r}$ about a common point, χ is approximately

$$\chi \approx \bar{\rho} \int g(r) u_{AB}(r) 4\pi r^2 \, dr \left(1 - \frac{1}{2} \frac{\sigma^2}{\lambda^2} \right) \tag{3.23}$$

$$\lambda^2 \equiv \frac{\int (\rho_A(\mathbf{x}) - \bar{\rho}_A)(\rho_B(\mathbf{x}) - \bar{\rho}_B) \, d\mathbf{x}}{\int \nabla \rho_A(\mathbf{x}) \cdot \nabla \rho_B(\mathbf{x}) \, d\mathbf{x}} \tag{3.24}$$

$$\sigma^2 \equiv \frac{\int g(r) u_{AB}(r) r^2 4\pi r^2 \, dr}{\int g_{AB}(r) u_{AB}(r) 4\pi r^2 \, dr} \tag{3.25}$$

Here, σ and λ are the characteristic length scales of the interparticle correlations, described by the ideal radial distribution function $g(r)$, and of the variations in the component density fields, respectively.

To clarify the meaning of the composition field length scale λ, consider a two phase fluid with domains of constant composition of characteristic size L connected by an interface of width l with a linear composition gradient. In this case, λ is given by $\lambda \approx \sqrt{Ll}$. Another example is a fluid with a sinusoidal plane wave composition field, $\lambda = l/\sqrt{2\pi}$, where l is the wavelength of the component density fields (see Section 3.4.3).

There are two qualitative aspects of the above results that are worth emphasizing. Firstly, Equation 3.21 always overestimates χ for systems with appreciable gradients in composition. Secondly, the non-local correction term to χ depends on a macroscopic property λ, which itself is determined by the magnitude of AB interactions. Therefore, the non-local corrections to χ in a particle system may be determined only after its macroscopic state has been determined. This is in contrast to the strictly microscopic nature of Equation 3.21.

3.3.4 Questions for simulations

To review the results so far, it has been shown that χ is composition-independent and given by the strictly microscopic mean-field Equation 3.21 if $u_h(r) \gg u_{AB}(r)$ and there is a large number of interacting neighbors per particle, $\sigma^3 \bar{\rho} \gg 1$. Reducing the magnitude of non-specific interactions or the range of the potentials leads to a decrease in χ or, alternatively,

an increase in the mean field, or "effective", χ required to produce a given degree of phase segregation.

Moreover, when the the length scale of composition variation and local particle correlations come to within an order of magnitude of each other, χ is reduced by an amount inversely proportional to the square of their ratio. This non-local correction is by definition macroscopic and may be calculated for a particle system only once its equilibrium state is known.

The challenge now is to quantify the former two effects and verify that Equation 3.23 describes the latter accurately. This is done here by numerical simulations. Specifically, the aims of the following numerical studies are

1. Determine just how great a difference between $u_h(r)$ and $u_{AB}(r)$ is required to suppress the effect of $u_{AB}(r)$ on the average pair density

2. Quantify the effect of fluctuations in the pair density on χ and determine the extent to which they may be suppressed

3. Test the accuracy of the non-local corrections in Equation 3.23

The first two issues are addressed by examining phase behavior of binary mixtures, where no long range composition gradients exist away from the critical point. In order to study the second, a system with artificially imposed long range composition variations is constructed in order to control them precisely.

3.4 Methods

3.4.1 Potentials

Binary mixtures of particles interacting through Lennard-Jones (LJ), Yukawa (Y), Gaussian (G), and uniform (C) potentials are considered. These potentials are given as:

$$LJ(r) = 4\epsilon \left[\left(\frac{s}{r} \right)^{12} - \left(\frac{s}{r} \right)^6 \right] \tag{3.26}$$

$$Y(r) = \epsilon \frac{3}{2\pi r} \exp\left(-\frac{r}{\sqrt{6}s} \right) \tag{3.27}$$

$$G(r) = \epsilon \sqrt{\frac{3}{2\pi s^2}}^{-3} \exp\left(-\frac{3r^2}{2s^2} \right) \tag{3.28}$$

$$C(r) = \begin{cases} \epsilon \frac{9\sqrt{15}}{100\pi s^3}, & \text{if } r < \frac{5}{\sqrt{15}}s \\ 0, & \text{otherwise} \end{cases} \tag{3.29}$$

Energy scale ϵ and width parameter s corresponding to u_h and u_{AB} are labelled by the corresponding subscripts when the distinction is relevant. Also, for normalizable potentials, U, G and Y, s is the standard deviation of the potential and ϵ is its norm (in three dimensions).

Generally, both $u_h(\mathbf{r})$ and $u_{AB}(\mathbf{r})$ are assumed to have the same form; however, one system with Lennard-Jones $u_h(\mathbf{r})$ and Yukawa $u_{AB}(\mathbf{r})$ is also examined.

These potentials were chosen for the following reasons. Uniform potentials correspond to the standard Flory-Huggins lattice fluid and other Ising-like models [1]. The Gaussian potential is representative of the soft interactions used in highly coarse-grained bead-spring polymer models [9, 54, 55]. The Yukawa potential was recently found to account for interactions between styrene and methyl-styrene monomers in experiments by Zirkel *et al.*based on the PRISM [56]. Finally, the Lennard-Jones potential is the basis for the Kremer-Grest polymer model and is generally a standard benchmark for particle models [57].

3.4.2 Determination of coexistence curves

Binary coexistence compositions were calculated using the semigrand canonical Monte Carlo (SGCMC) method of Miguel *et al.*[58]. In this method, only one of the two coexisting homogeneous phases must be simulated, so that no long range composition gradients need

be considered. For this study, the translation and particle type exchange moves were chosen at random, with approximately equal probability (except for lattice models where no displacement moves were allowed). All systems were simulated for about 10^7 moves, with acceptance rates around 50%. Thus, each particle underwent about 10^4 type changes and translations. Simulations were performed with 1000 particles with $\bar{\rho} = 1$ and $s = 1$ for all potentials. To maintain incompressibility, ϵ_h was chosen to be at least 20 times ϵ_{AB}; however, $\epsilon_h = 1$ was used for the LJ potential. The output of each set of simulations is a symmetric histogram of compositions, $f_A = n_A/(n_A + n_B)$. To speed up convergence, the histograms were symmetrized by counting $1 - f_A$ as a separate sample whenever a composition f_A was observed. The equilibrium coexistence composition for a macroscopic system was estimated as the most frequently observed composition [43, 58].

3.4.3   Mixture with externally imposed field

In order to examine non-local corrections, a plane wave composition profile was imposed on a mixture in a standard canonical molecular dynamics simulation(MD, [43]). Specifically, at each time step a random number η, uniform on $[0, 1)$ was generated for each particle. If $\eta < 0.5(1 + \sin(2\pi x/l))$, where x is the particle position along the x-axis, the particle was assigned type A; otherwise it was assigned type B. This resulted in a plane wave composition field

$$\rho_A(\mathbf{x}) = 0.5 + 0.5\bar{\rho}\sin(2\pi x/l)) \tag{3.30}$$

Such composition variation is encountered, for example, in weakly and moderately segregated block copolymer blends [2]. In this case, the composition field wavelength is given by $\lambda^2 = l^2/2\pi$.

Gaussian $u_h(r)$ and $u_{AB}(r)$ were used (Equation 3.28), with $\epsilon_h = 20$ and $\epsilon_{AB} = 2$. The order of magnitude difference between these scales was assumed to approximate incompressibility (this is checked separately in the Results section). Particle density, $\bar{\rho}$, and potential width, s, were set to one. Simulations were performed with 1000 particles for $l \leq 10s$ and $(l/s)^3$ particles for larger wavelengths.
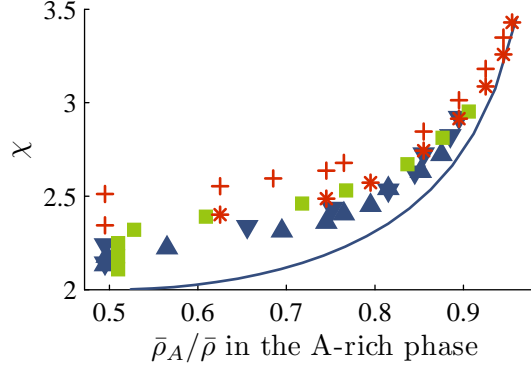
Figure 3-1: Equilibrium composition of symmetric binary fluids: BCC ($*$) and cubic ($+$) lattice fluids; off-lattice fluids with Gaussian u_h and u_{AB} ($\blacksquare$); Yukawa u_{AB} and Lennard-Jones u_h ($\blacktriangledown$); Yukawa u_h and u_{AB} ($\blacktriangle$). Flory-Huggins mean field result is plotted for comparison as the solid line [1]: $\chi_{MF}(f_A) = \ln[(1 - f_A)/f_A]/(1 - 2f_A)$.

3.4.4   Results

Binary mixture with homogeneous phases

The SGCMC simulations described above produced equilibrium coexistence compositions of the two phases in a symmetric binary mixture with interactions potentials of a fixed form, over a range of ϵ_{AB} (the magnitude of the penalty potential). While two systems with the same ϵ_{AB} but different shapes of the potentials cannot be compared directly, calculating χ values corresponding to the two systems using Equation 3.21 makes a quantitative comparison possible. Figure 3-1 shows that the coexistence compositions of the fluids examined here are in close agreement when plotted against χ. All the curves lie within about 15% of each other. This consistency is remarkable considering that it was achieved for a range of lattice, soft, and hard-core fluids without any adjustable parameters.

While consistency of these results is very important from the practical standpoint, even more significant is that the discrepancies among the curves are precisely as anticipated in Section 3.3.3. First note that all systems appear to converge in the dilute limit, where all interacting neighbors of the minority component are of the same kind, regardless of the exact composition. Second, the degree of deviation from the mean field result increases with decreasing coordination number, and hence, magnitude of fluctuations in the composition of the system of interacting neighbors of any given particle. Thus, each particle in the cubic system interacts with only six neighbors and falls farthest from the mean-field result. At

the other end of the spectrum are the Lennard-Jones and Yukawa systems, which have relatively large radii of interaction ($\sigma \approx 2s$ in both systems) and consequently large number of interactions per particle. The Gaussian system, with $\sigma \approx 1.1s$, falls in the middle along with the BCC lattice system, which also has an intermediate coordination number. Finally, the importance of fluctuations in pair density is further corroborated by the dramatic increase in accuracy of the χ predicted by Equation 3.21 with increasing width of the interaction potentials (*e.g.*number of neighbors per particle) for the Gaussian system. This result is shown in Figure 3-2.
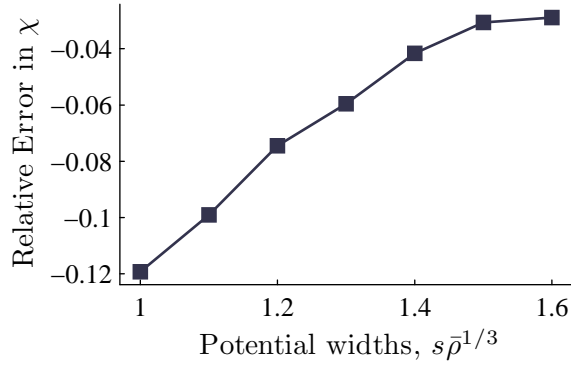
Figure 3-2: Relative error in χ values predicted by Equation 3.21 compared to Equation 3.6 as a function of the potential width (related to the number of interacting neighbors per particle). Here $\chi \approx 2$, $\epsilon_h = 100$ corresponding to a single homogeneous phase; $s_{AB} = s_h = s$

The distortion of the AB radial distribution function relative to the AA one appears to have a noticeable, but small effect in this set of simulations. The effect should be most apparent in the dilute regime, where the number of solute-solvent (AB) interactions per solute particle is maximized. Yet, this is not the case, suggesting that ϵ_h values were indeed sufficiently high in these simulations. Furthermore, examining the AB radial distribution functions in Figure 3-3 for the Gaussian and LJ-Yukawa systems (near the critical point) shows very little difference between the two. (These plots would not account for two and three-dimensional changes in the pair density.) Nevertheless, as Figure 3-4 shows, the error in χ for the Gaussian system appears to decrease linearly with the logarithm of ϵ_h. The dependence has important implications for simulations, where smaller values of ϵ_h should reduce the stiffness of the equations of motion, making sampling and equilibration easier. Thus, on one hand, ϵ_h values may be reduced to some extent without significant loss of accuracy, but on the other, enormous increase in stiffness is required to achieve any
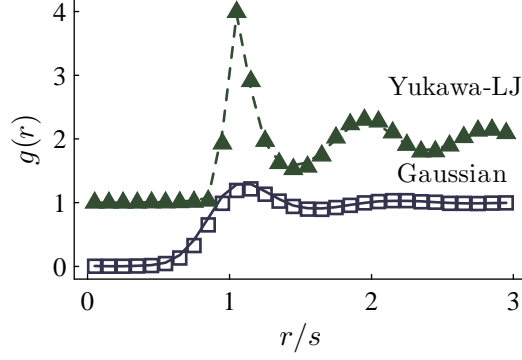
Figure 3-3: Comparison of AB radial distribution functions with $\chi \approx 2$ (points) and $\chi = 0$ (lines) for Gaussian and Yukawa-LJ systems.

improvement in the accuracy of χ values obtained from Equation 3.21.
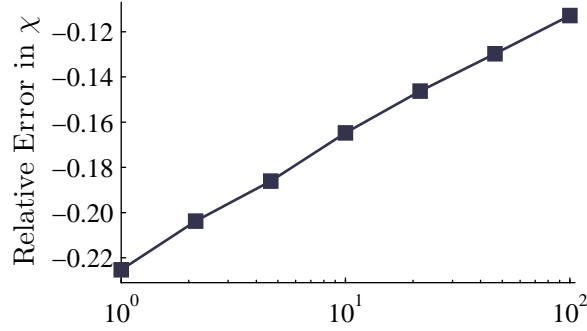
Figure 3-4: Error in χ predicted by Equation 3.21 as a function of the homogeneous potential strength, ϵ_h. Here $\chi \approx 1.9$ corresponding to $\epsilon_{AB} \approx 2 - 3$. Gaussian potentials.

Finally, it should be noted that doubling the system size did not significantly change the phase diagram for the LJ-Yukawa and cubic lattice systems (results not shown), relegating possible finite size artifacts to small corrections. Also, by definition, the SGCMC simulations deal with homogeneous phases excluding non-local corrections.

3.4.5 Non-local effects

Figure 3-5 compares the exact χ values to the estimates obtained from Equation 3.23 for a binary mixture with plane wave composition field (see Section 3.4.3). The results are in close agreement even when σ and λ become comparable.

There are, however, discrepancies of as much as 10%. This error may be attributed to the poor quality of low-order Taylor approximations of the sine function. To test this
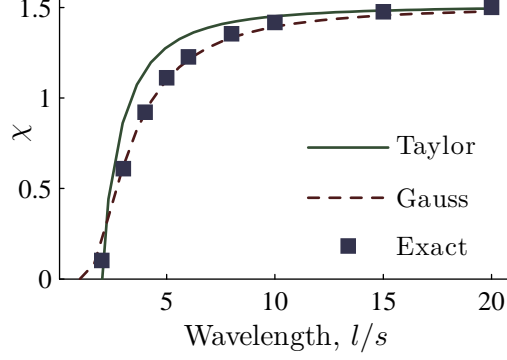
Figure 3-5: Comparison of the exact χ Equation 3.7 to the approximate equations Eq. 3.23 ("Taylor") and Eq. 3.31 ("Gauss"). Results are for a symmetric mixture with binary interactions and an externally imposed plane wave composition field with wavelength l.

hypothesis an alternative expression for χ was obtained without invoking Taylor expansions by taking advantage of the particularly simple features of this system (refer to Appendix 3.7.2 for derivation):

$$\chi \approx \bar{\rho} \int g(r) u_{AB}(r) 4\pi r^2 \, \mathrm{d}r \exp\left(-\frac{2\pi^2 \sigma^2}{3l^2}\right) \tag{3.31}$$

Figure 3-5 shows this to be a much more precise estimate for the particular case of sinusoidal composition fields. It is also straightforward to check that the expression is nearly identical to Equation 3.23 up to terms of order $(\sigma/\lambda)^4$.

Overall, these results confirm that Equation 3.23 is a good estimate of χ. Moreover, Equation 3.31 is an even better estimate in the special case of plane wave composition fields and soft interactions.

3.5 Discussion

The results presented above are put in perspective by considering each particle as a coarse-grained representation of a large section of a polymer chain. The range, s, of effective interaction potentials should be comparable to the radius of gyration of the chains, R_g, and the interactions themselves may be taken to be roughly Gaussian. Now, the number of interactions per particle may be described by $s^3 \bar{\rho} = n/V R_g^3$. Incidentally, this is precisely the Ginsburg parameter, C, defined by Ganesan *et al.*as a measure of the importance of thermal fluctuations in determining phase behavior of blends and block copolymers [18]. Figure 3-2

indicates that $s^3\bar{\rho}$ must be of order one, with $s^3\bar{\rho} = 1$ corresponding to approximately 10% error in the mean-field χ. Thus, for a typical synthetic polymer, each particle must represent at least 100–1000 repeat units. This number is estimated by calculating the Ginsburg parameter, the chain density, defined above using Kuhn segment length and density data for typical polymers. This is comparable to the molecular weights of whole molecules used in many experimental studies, particularly those of block copolymers. In other words, achieving even a relatively modest level of uncertainty in experimental values of χ requires a model with extremely low resolution. Note that considering long chains also allows the $\epsilon_{AB} \ll \epsilon_h$ condition to be satisfied.

The general idea emerging from these considerations is that the notion of a scalar, composition independent χ parameter strictly applies to particle systems only when the mean field approximation holds and only when particles of different types are distinguished exclusively by their type labels and the penalty potential. What is lost in using a single scalar parameter to describe excess interactions between particles is the coupling between the pair density and composition. Accounting for these effects makes χ composition dependent, in agreement with experimental evidence. While this idea is not new, a crucial point made by the above analysis is that composition dependence of χ does not have to arise from complex, chemically-specific interactions among polymers, as suggested by [16, 30]. The composition dependence of experimentally measured χ values in real and model systems can be attributed to the fact that the particles corresponding to realistic monomers or even polymers generally interact with too few other particles at a time for the mean-field assumption to apply. Unlike a model where mean-field behavior is directly assumed to apply locally (*e.g.* as in standard field theories), a particle system may compensate for an increase in the penalty potential $u_{AB}(r)$ through local correlations, damping the change in the macroscopic state of the system and apparent χ values. Thus, experimental measurements of χ based on matching mean-field theory predictions, such as critical points or the de Gennes RPA structure functions, are expected to overestimate χ. Direct evidence for this has been provided by Kremer and Grest, who determined both the mean field χ and the de Gennes' RPA value for a particular model polymer and found the latter to be about 25% higher than the former [52]. This is also consistent with analyses of fluctuations in field theories of the standard Gaussian chain model, which predict an increase in the apparent critical χ values with decreasing molecular weight for both block copolymers and blends [3, 17].

The results presented here also enrich the explanation of composition and temperature dependence of χ parameters proposed by Curro and Schweizer based on PRISM. Very broadly, Curro and Schweizer implicitly relate the effective χ to particle radial distribution functions through Ornstein-Zernike direct correlation functions. While Curro and Schweizer suggest that this relationship should simplify studying the dependence of χ on thermodynamic parameters of a system, they do not address the issue of composition dependence specifically in any detail. In this study, the arguments are somewhat more direct, leading to more explicit conclusions. First, as shown above, the behavior of particles representing finite sections of real chains are strongly affected by fluctuations. This lowers the actual χ by an extent quantified in a number of test cases and predicted qualitatively in general. Second, most real monomers that would correspond to a model particle have different mass, different statistical segment lengths, and are unlikely to have strictly spherically symmetric interactions. Therefore, their radial distribution functions are likely to depend on composition even if thermal fluctuations are neglected.

In the PRISM, the temperature dependence of experimental χ values is obtained from the specific form of the PRISM structure function, neglecting the temperature dependence of direct correlation functions themselves. In the present analysis, if the potentials and radial distribution functions are assumed to be temperature-independent, Equation 3.21 implies directly that $\chi \propto 1/T$. This is somewhat complicated by the temperature dependence of the radial distribution functions and the free-energy-like nature of the potentials, if they are to be obtained from more detailed polymer models. Nevertheless, it is important to emphasize that χ depends on temperature even if the potentials and correlations do not.

Fortunately, the above conclusions still leave room for particle models constructed specifically to have a relatively well-defined χ value and therefore quantitatively comparable to traditional field theories. This opens the possibility of rigorously supplanting field theoretic polymer simulation studies beyond the mean field limit with simple bead-spring dynamic models, such as the Kremer-Grest or dissipative particle dynamics soft particle models [9, 55]. The results presented here indicate that the error in the mean field Equation 3.23 may be reduced to only a few percent by using a model with a relatively broad potential, $s \approx 1.5\bar{\rho}^{-1/3}$, and a one to two orders of magnitude difference between the strengths of the homogeneous and heterogeneous potentials, $\epsilon_h/\epsilon_{AB} \approx 10 - 100$. While such models may not be entirely realistic physically, they may be effective computational analogues to the

field theoretic simulations.

Note that in this case, a significant trade-off between resolution and reliability emerges. If too few particles are used to represent a molecule or too large an interaction radius, non-local corrections to χ become important. While Equations 3.23 or 3.31 may be used to compensate for this to some extent, they too should fail for small enough difference in scales.

Nevertheless, constructing a coarse-grained particle-based model of a heterogeneous polymer blend with χ parameters specified to within a few percent now appears feasible.

3.6   Conclusions

The aim of this article has been to characterize the conditions required for a particle system to have a well-defined χ. In summary, these conditions are: the particles of different types are distinguished only by their labels and the penalty potential; the number of interactions per particle is large; the energetic difference between particles of different types is too small to distort local correlations; and the scale of interparticle correlations is much smaller than the scale of long-range composition gradients. Together, these conditions affect a mean-field environment for each particle and make it possible to associate a constant, composition independent χ value as it is used in common field theories. These conditions are not realistic in physical systems, which explains composition and temperature dependence of experimentally measured χ values.

Overall, many of the ideas gathered here have been long recognized. The contribution of this article, however, is in systematizing and quantifying their consequences in a single, generalized framework treating lattice, hard and soft-core particle models on the same terms. An important result of this systematic analysis is the clear delineation between models where χ is well-defined and physically realistic particle models. This should be of interest in any attempt to compare an explicit simulation of an ensemble of polymers with traditional field theories.

3.7 Appendix

3.7.1 Non-local corrections to χ

This section explains calculations leading to Equation 3.23. The starting point for these calculations is Equation 3.16 with $g(r)$ used instead of the full pair density for simplicity.

$$U_{AB}[\rho_A, \rho_B] = \int \rho_A(\mathbf{x} - \mathbf{r}/2)\rho_B(\mathbf{x} + \mathbf{r}/2)g(|\mathbf{r}|)u_{AB}(\mathbf{r}) \, \mathrm{d}\mathbf{r} \, \mathrm{d}\mathbf{x} \qquad (3.7\text{-}1)$$

Here, the $\mathbf{x}$ coordinate has been redefined to symmetrize the equation. Now if both density fields are replaced by their Taylor expansions around $\mathbf{x}$, only the terms even in the components of the vector $\mathbf{r}$, contribute to the ensemble average energy in Equation 3.10. This leads to

$$U_{AB}[\rho_A, \rho_B] = \int \rho_A(\mathbf{x})\rho_B(\mathbf{x}) \, \mathrm{d}\mathbf{x} \int g(|\mathbf{r}|)u_{AB}(\mathbf{r}) \, \mathrm{d}\mathbf{r}$$
$$- \frac{1}{2}\nabla\rho_A(\mathbf{x}) \cdot \nabla\rho_B(\mathbf{x}) \int g(|\mathbf{r}|)u_{AB}(\mathbf{r})|\mathbf{r}|^2 \, \mathrm{d}\mathbf{r} \quad (3.7\text{-}2)$$

Therefore, the excess field energy with respect to the ideal mixture reference state is given by

$$\Delta U_{AB}[\rho_A, \rho_B] = U_{AB}[\rho_A, \rho_B] - U_{AB}[\bar{\rho}_A, \bar{\rho}_B] \qquad (3.7\text{-}3)$$

$$= \int (\rho_A(\mathbf{x}) - \bar{\rho}_A)(\rho_B(\mathbf{x}) - \bar{\rho}_B) \, \mathrm{d}\mathbf{x} \int g(|\mathbf{r}|)u_{AB}(\mathbf{r}) \, \mathrm{d}\mathbf{r} \, \mathrm{d}\mathbf{r}$$
$$- \frac{1}{2}\nabla\rho_A(\mathbf{x}) \cdot \nabla\rho_B(\mathbf{x}) \int g(|\mathbf{r}|)u_{AB}(\mathbf{r})|\mathbf{r}|^2 \, \mathrm{d}\mathbf{r} \quad (3.7\text{-}4)$$

where the excess density fields are defined as $\rho_K(\mathbf{x}) \equiv \rho_K(\mathbf{x}) - \bar{\rho}_K$ for $K = A, B$. Substituting this expression into Equation 3.7 yields Equation 3.23.

3.7.2 Special case of sinusoidal composition fields

Taylor expansions in the above analysis turn out to be an unnecessary approximation for the mixture with plane wave composition fields and a soft interaction potential, such as in

the case described in Section 3.4.3. Consider estimating $u_{AB}(\mathbf{r})g(r)$ as a Gaussian function

$$u_{AB}^*(\mathbf{r}) \equiv g_{AB}(\mathbf{r})u_{AB}(\mathbf{r}) \tag{3.7-5}$$

$$u_{AB}^*(\mathbf{r}) = \chi \left(\frac{3}{2\pi\sigma^2} \right)^{\frac{3}{2}} \exp \left(-\frac{3\mathbf{r}^2}{2\sigma^2} \right) \tag{3.7-6}$$

$$\chi \equiv \int u_{AB}(r)g(r)\,\mathrm{d}\mathbf{r} \tag{3.7-7}$$

Here σ is given by Equation 3.25. Figure 3-6 shows this estimate of $u_{AB}(\mathbf{r})g(r)$ to be at least a reasonable approximation.
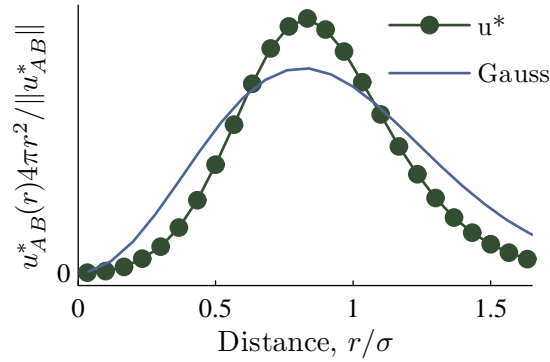
Figure 3-6: Comparison of $u^*(\mathbf{r}) = g(\mathbf{r})u_{AB}(\mathbf{r})$ to the Gaussian distribution, both integrated over spherical angular coordinates and normalized to unity in $\mathbf{r}$. The system is described in Section 3.4.3

Equation 3.16 may now be evaluated analytically for plane wave fields, resulting in

$$\frac{\Delta U_{AB}[\rho_A, \rho_B]}{\chi} = \int \Delta\rho_A(\mathbf{x})u_{AB}^*(\mathbf{x} - \mathbf{y})\Delta\rho_B(\mathbf{y})\,\mathrm{d}\mathbf{x}\,\mathrm{d}\mathbf{y} \tag{3.7-8}$$

$$= \int (0.5\sin(2\pi x/l))^2 \exp \left(-\frac{2\pi^2\sigma^2}{3l^2} \right)\,\mathrm{d}\mathbf{x} \tag{3.7-9}$$

Substituting this into Equation 3.7 results in

$$\chi = \exp \left(-\frac{2\pi^2\sigma^2}{3l^2} \right) \int g(|\mathbf{r}|)u_{AB}(|\mathbf{r}|)\,\mathrm{d}\mathbf{r} \tag{3.7-10}$$

Also, expressing l in terms of λ and Taylor-expanding the exponential yields

$$\chi \approx \left(1 - 0.524\frac{\sigma^2}{\lambda^2} \right) \int u_{AB}(|\mathbf{r}|)g(|\mathbf{x}|)\,\mathrm{d}\mathbf{x} \tag{3.7-11}$$

64

very nearly recovering the original estimate, Equation 3.23.

4

A bead-spring polymer model with well-defined Flory-Huggins miscibility and chain density

Abstract

We propose a direct interpretation of a family of coarse-grained bead-spring block copolymer models with soft non-bond interactions in terms of the standard Gaussian chain model (GCM). Specifically, we show that under conditions of sufficiently low resolution and high chain density, interaction parameters in the particle model may be expressed in terms of the Flory-Huggins miscibility parameter, the Helfand compressibility parameter, and the dimensionless chain density to within a controllable and generally acceptable tolerance. A close agreement of the prediction of the model with field theoretic results and experimental data on critical behavior of symmetric diblocks, including the critical miscibility, scattering function amplitude, and periodicity of the structure are demonstrated. Our approach is distinguished from similar efforts in that it does not rely on matching of macroscopic properties, but a direct microscopic interpretation of the GCM parameters. Such parametrization makes straightforward molecular dynamics simulations of bead-spring chains a complementary but independent alternative to field theoretic simulations. These explicit chain simulations offer significant practical advantages in sampling thermal fluctuations in systems of moderate molecular weight and, potentially, in non-equilibrium situations without sacrificing thermodynamic rigour.

4.1 Introduction

Our understanding of polymer blends and block copolymers rests largely on the observation that many molecular scale features of these systems may be described by macroscopic parameters, abstracting from the details of molecular structure. This property allows us to infer the behavior of one polymer system based on observations of another physical, or more commonly, highly simplified coarse-grained theoretical model polymer system. Making such inferences, however, requires a way to relate the microscopic parameters defining the nature of the model system to those of the system whose properties are desired.

In practice, coarse-grained models are parametrized by matching a thermodynamic property under a set of conditions where measurements are readily accessible. For example, a common way to measure the Flory-Huggins miscibility parameter, χ, used in the standard Gaussian chain model (GCM [18]) involves matching the low frequency tail of the scattering function of a material to the analytical estimate available under the nearly ideal mixing conditions, or random phase approximation (RPA). Another technique involves matching critical temperature at a single point or as a function of molecular weight [3, 9, 12, 16, 17]. Another, classic example of such extrapolation is the Flory mean-field estimate of site coupling parameters in lattice chain models, which estimates the energy of an immiscible lattice chain system based on the ideal mixture limit [1, 17].

While usually effective, these means of measuring model parameters assume that the measured parameter values remain valid away from the conditions used for parametrization. The uncertainty involved in such extrapolation is difficult to predict and often leads to significant inconsistencies among various models and measurements on real polymers. For example, the RPA is found to be too restrictive for many common polymer systems, resulting in differences in Flory-Huggins parameters measured in blends and block copolymers of the same components [16, 17]. Similar problems are observed in polymer simulations, such as the polymer dissipative particle dynamics (PDPD) model of Groot *et al.*[9] or lattice chain simulations of, for example, Matsen *et al.*[10, 51]. In case of the PDPD, χ parameters estimated by matching critical points in blends of monomers were found to predict the critical point in block copolymers at a value of χ as much as four times greater than the commonly accepted mean-field estimate of Liebler. The same discrepancy is found in lattice chain simulations by Matsen , who follow Flory [1] in extrapolating the χ values from the

ideal mixture limit to block copolymers.

Avoiding such discrepancies requires a more direct relationship between the microscopic parameters of the model and those of a real systems than matching of a single thermodynamic property affords. In this article, we focus on defining such relationships among members of a class of coarse-grained bead-spring block copolymers with soft repulsive non-bond interactions of varying range and number of particles representing each chain. The choice of this type of model is motivated by the work of Grest *et al.*and Fredrickson *et al.*who have argued that continuous space coarse-grained particle-based models have a number of practical advantages over the more traditional lattice and field-theoretic models [12, 18]. For example, isobaric ensemble studies are easier to formulate in continuous space particle system than in lattice chain models, which is crucial in studying intrinsically non-isotropic ordered phases of block copolymers. Compared to field theoretic approaches, particle simulations are simpler to extend to non-equilibrium situations as well as to measurement of dynamic properties [18]. We chose to focus on block copolymers rather than blends for two reasons. Firstly, the length scale of order parameter fluctuations in block copolymer is bounded by the molecular dimensions, making precise simulation of critical behavior possible with small periodic systems. Secondly, the widely acknowledged importance of thermal fluctuations in block copolymers has lead to considerably more significant errors in the traditional approaches to modeling block copolymers than in blends [3, 17].

The central hypothesis of our study is that it is possible to parametrize the bead-spring models in a way that would establish both clear relationships among them and the extent to which their behavior is universal. At the same time, we seek a parametrization scheme that is sufficiently simple not to compromise the practical advantages of the particle simulations. Specifically, we attempt to express the particle model parameters in terms of the composition, radius of gyration, the Flory-Huggins miscibility parameter, compressibility, and dimensionless chain density that fully define block copolymer behavior in the GCM [18]. Emphasis is placed on the relationship between the Flory-Huggins χ parameter associated with the non-bond interaction potentials in the particle model. One reason we chose the GCM as the standard is that GCM is the foundation for the most widely used field theories of block copolymers, including the classical self-consistent field theory of Helfand *et al.*[20] and the more recent field theoretic simulation methods of Fredrickson *et al.*[18]. Equally compelling is the fact that GCM is the ultimate macroscopic model, abstracting from the

specific molecular structure entirely. Rather than dealing with individual molecules, the GCM is formulated in terms of monomer density and chemical potential fields. Thus, GCM may be said to contain only universal features of polymer behavior. Consequently, to the extent that a beads-spring block copolymer may be considered universal, it should be possible to map directly onto GCM.

Our approach to this challenge of relating particle and field theoretic parameters is an extension of a similar analysis we have performed for binary blends of particles [49] (also the preceeding chapter of this thesis). In that study, we reduced the problem to examining the effect of incompatibility between species on the particle radial distribution function. Generalizing the approach to polymers poses two major challenges, which we address first analytically and then in simulations. Firstly, we must address the effect of bonds on particle position correlations. Secondly, we must develop an explicit definition of the macroscopic density fields. In our previous study, we followed the GCM literature in defining macroscopic density fields as instantaneous local averages. This led to the introduction of an implicit density smoothing function, which effectively enforces a frequency cutoff. Since the previous study dealt mainly with homogeneous phases, there was no need for detailed examination of the density averaging function. In block copolymers, however, molecular scale variation in composition is the central feature of the phase behavior. Therefore, precise measurement of macroscopic density fields is essential.

4.2 Theory

4.2.1 Particle and field models

The system of interest here is a monodisperse set of n block copolymer chains, each made up of N monomers, confined to volume V and characterized by temperature T. All monomers are point particles of identical mass, m. Each particle is described by an index i, position $\mathbf{x}_i$, and a type label $K_i \in \{A, B\}$. The first $f_A N$ monomers along each chain are of type A and the rest are of type B. Let Γ be the set of all particle coordinates and Ω be the phase space of Γ. To simplify notation, we express all energies in units of $k_B T$, all masses in units of m, and all lengths in units of characteristic interparticle spacing $1/\bar{\rho}^{1/3} = (V/n)^{1/3}$.

Following Grest *et al.*[12], we compose the Hamiltonian of this system using three terms: bond interactions reflecting the molecular topology; homogeneous, or type-independent,

non-bond interactions that reflect the compressibility of the system; and excess non-bond interactions that reflect the immiscibility of the two types of blocks:

$$H(\Gamma) = H_b(\Gamma) + H_h(\Gamma) + H_{AB}(\Gamma) \tag{4.2-1}$$

$$H_b = \sum_{(i,j)\in\mathbb{B}} k\, r_{ij}^2 \tag{4.2-2}$$

$$H_h = \sum_{i,j\in\mathbb{I},i>j} \epsilon_h K(r_{ij}) \tag{4.2-3}$$

$$H_{AB} = \sum_{i\in\mathbb{I}_A,j\in\mathbb{I}_B} \epsilon_{AB} K(r_{ij}) \tag{4.2-4}$$

$$r_{ij} \equiv |\mathbf{x}_j - \mathbf{x}_i|$$

where $\mathbb{B}$ is the set of all unique pairs of indices of particles connected to each other by bonds; $\mathbb{I}$ is the set of all particle indices; and $\mathbb{I}_K$ is the set of indices of all the particles of type K. Further, the shape of the potentials is defined by the kernel function $K(r)$, assumed to be spherically symmetric and normalized so that $\int K(r)4\pi r^2\, \mathrm{d}r = 1$. Here we use a purely repulsive Gaussian kernel similar to those in references [55, 59],

$$K(r) \equiv \left(\frac{3}{2\pi\sigma^2}\right)^{\frac{3}{2}} \exp\left(-\frac{3r^2}{2\sigma^2}\right) \tag{4.2-5}$$

rather than the hard-core one used by Grest *et al.*[12]. Finally, let $P(\Gamma)$ be the probability density function for $\Gamma \in \Omega$, given as $P(\Gamma) \equiv Z^{-1}\exp(-H(\Gamma))$ where Z is the partition function such that $\int_\Omega P(\Gamma)\, \mathrm{d}\Gamma = 1$.

The macroscopic counterpart of this particle model, the GCM, is generally formulated as a field theory, describing the state of the same system in terms of monomer density fields $\rho_A(\mathbf{x})$ and $\rho_B(\mathbf{x})$ and their probability density functional $P[\rho_A, \rho_B] = Z_f^{-1}\exp(-U[\rho_A, \rho_B])$. Z_f is the partition function of $P[\rho_A, \rho_B]$ with respect to the density fields, such that the functional integral $\iint P[\rho_A, \rho_B]\, \mathrm{d}\rho_A\, \mathrm{d}\rho_B = 1$. The monomer density fields are assumed to be "smooth" in a sense to be defined shortly. The effective free energy associated with the

pair of fields is composed of terms analogous to those of $H(\Gamma)$:

$$U = U_b + U_h + U_{AB} \tag{4.2-6}$$

$$U_h = \frac{\zeta}{2\bar{\rho}} \int (\rho_A(\mathbf{x}) + \rho_B(\mathbf{x}))^2 \, d\mathbf{x} \tag{4.2-7}$$

$$U_{AB} = \frac{\chi}{\bar{\rho}} \int \rho_A(\mathbf{x}) \rho_B(\mathbf{x}) \, d\mathbf{x} \tag{4.2-8}$$

where $\bar{\rho}$ is the volume average particle density, nN/V; χ is the Flory-Huggins composition field coupling parameter; and ζ is the Helfand incompressibility parameter [20]. The free energy associated with conformational entropy of the chains, $U_b[\rho_A, \rho_B]$, cannot generally be evaluated analytically. It is, however, fully determined by the by the unperturbed radius of gyration of the chains, $R_g \equiv a\sqrt{N/6}$, where a is the root-mean-squared bond length measured in the homopolymer limit, where $f_A = 0$ or 1 [18].

Field theoretic calculations generally rely on evaluating various properties of $P[\rho_A, \rho_B]$ by means other than direct sampling of $P[\rho_A, \rho_B]$. We refer the reader to comprehensive review articles [18, 23] for details of field theoretic calculations and mention some key observations here. Commonly, only the mean field solution, which in this case is also minimizes the free energy, of the macroscopic model is obtained. The mean field solution is fully determined by χN, R_g, f_A, and monomer density, $\bar{\rho}$. The Ginsburg parameter characterizing the extent of thermal fluctuations around the mean field solution is the dimensionless chain density

$$C = \frac{n}{V} R_g^3 \tag{4.2-9}$$

4.2.2 Miscibility

Expressing the miscibility of A and B particles in the bead-spring model in terms of the GCM requires a way to associate smooth density fields with instantaneous particle coordinates. Here we assume that these fields are given by some function $\rho_K(\mathbf{x}; \Gamma)$ for $K \in (A, B)$. Specific examples of how such a function can be defined are discusseed at the end of this section. In the meantime, we proceed to define χ by setting the excess energy terms associated with the miscibility in the two models equal as follows

$$\langle H_{AB}(\Gamma) \rangle_{\Omega[\rho_A, \rho_B]} = U_{AB}[\rho_A(\mathbf{x}), \rho_B(\mathbf{x})] \equiv \frac{\chi}{\bar{\rho}} \int \rho_A(\mathbf{x}) \rho_B(\mathbf{x}) \, d\mathbf{x} \tag{4.2-10}$$

Here the shorthand $\langle \cdot \rangle_{\Omega[\rho_A,\rho_B]}$ is used for an ensemble average carried out over only the part of the phase space Ω of the particle positions where $\rho_K(\mathbf{x}; \Gamma) = \rho_K(\mathbf{x})$ for $K \in (A, B)$. To make use of the above identity of non-bond excess energies, we rewrite the ensemble average of the Hamiltonian in terms of the radial distribution function, $g_{AB}(r)$ for A-B particle pairs and the macroscopic density fields

$$\langle H_{AB}(\Gamma) \rangle_{\Omega[\rho_A,\rho_B]} \equiv \epsilon_{AB} \iint \rho_A(\mathbf{x}) \rho_B(\mathbf{x}) g_{AB}(r) K(r) 4\pi r^2 \, \mathrm{d}r \, \mathrm{d}\mathbf{x} \qquad (4.2\text{-}11)$$

where $r = |\mathbf{r}|$. The radial distribution function $g_{AB}(r)$ may be formally defined in terms of exact density fields, $\rho_K^*(\mathbf{x})$, which represent each particle as a three-dimensional version of the Dirac δ function, as follows

$$g_{AB}(r) = \mathcal{W}\left[\rho_A^*(\mathbf{x}) \rho_B^*(\mathbf{x} + \mathbf{r}))\right] \qquad (4.2\text{-}12)$$

$$\rho_K^*(\mathbf{x}) \equiv \sum_{i \in \Gamma_K} \delta(\mathbf{x} - \mathbf{x}_i) \quad \forall \quad K \in (A, B) \qquad (4.2\text{-}13)$$

where $\mathcal{W}[f]$ is a linear operator mapping any well-behaved function $f(\mathbf{x}, \mathbf{r})$ onto a spherically symmetric function of r as

$$\mathcal{W}[f(\mathbf{x}, \mathbf{r})] \equiv \frac{\iint \langle f(\mathbf{x}, \mathbf{r}) \rangle_{\Omega[\rho_A,\rho_B]} \delta(|\mathbf{r}| - r) \, \mathrm{d}\mathbf{r} \, \mathrm{d}\mathbf{x}}{\int \rho_A(\mathbf{x}) \rho_B(\mathbf{x}) \, \mathrm{d}\mathbf{x}} \qquad (4.2\text{-}14)$$

The expected ensemble average of the Hamiltonian given in Eq. 4.2-4 is recovered by substituting the definitions in equations 4.2-12 through 4.2-14 into Eq. 4.2-11. The benefit of these manipulations is that the microscopic details of the bead-spring model are encapsulated in $g_{AB}(r)$.

It is convenient to take this encapsulation process one step further by factoring out the integral over r from Eq. 4.2-11

$$\langle H_{AB}(\Gamma) \rangle_{\Omega[\rho_A,\rho_B]} \equiv \epsilon_{AB} \xi \int \rho_A(\mathbf{x}) \rho_B(\mathbf{x}) \, \mathrm{d}\mathbf{x} \qquad (4.2\text{-}15)$$

where the correlation integral ξ is defined as

$$\xi \equiv \int g_{AB}(r) K(r) 4\pi r^2 \, \mathrm{d}r \qquad (4.2\text{-}16)$$

Finally, this allows us to define the χ miscibility parameter for a given bead-spring model in terms of the correlation integral

$$\chi \equiv \epsilon_{AB}\xi\bar{\rho} \qquad (4.2\text{-}17)$$

.

A particularly convenient and common way to estimate ξ is to assume that the correlation integral, ξ_0 measured when $\epsilon_{AB} = 0$ does not change as ϵ_{AB} is increased. We will refer to ξ_0 as the "homogeneous" approximation. This is the approximation made by, for example, Flory [1] and Binder $et\ al.$[52] in lattice models and by Grest $et\ al.$[12] in bead-spring simulations. If the correlations due to bonds may be neglected, this is equivalent to taking $g_{AB}(r) = g_{AA}(r)$ in a single component fluid. Otherwise, this assumption may be seen as an ideal mixture approximation, where the interparticle correlations are dominated by the non-specific interactions and are independent of miscibility. Consequently, χ is strictly proportional to ϵ_{AB} across the whole range of miscibility (see, for example, [49]).

As we have argued previously [49], excess AB repulsion does affect the interparticle correlations even when the non-specific interactions are dominant ($\epsilon_{AB} \ll \epsilon_h$). The corrections to the homogeneous approximation, ξ_0, of the correlation integral may be separated into contributions ξ_{nl} and ξ_l from long-range and local correlations, correspondingly:

$$\xi = \xi_0 + \xi_l + \xi_{nl} \qquad (4.2\text{-}18)$$

$$\xi_0 = \lim_{\epsilon_{AB}\to 0} \mathcal{W}\left[\rho_A^*(\mathbf{x})\rho_B^*(\mathbf{x}+\mathbf{r})\right] \qquad (4.2\text{-}19)$$

$$\xi_{nl}[\rho_A,\rho_B] = \mathcal{W}\left[\rho_A(\mathbf{x})\rho_B(\mathbf{x}+\mathbf{r})\right] \qquad (4.2\text{-}20)$$

$$\xi_l[\rho_A,\rho_B] = \mathcal{W}\left[\rho_A^*(\mathbf{x})\rho_B^*(\mathbf{x}+\mathbf{r}) - \rho_A(\mathbf{x})\rho_B(\mathbf{x}+\mathbf{r})\right] - \xi_0 \qquad (4.2\text{-}21)$$

In the following discussion we drop the explicit functional arguments for ξ_{nl} and ξ_l unless they are essential to the meaning. Both terms are negative as they reflect the reduction in U_{AB} through additional correlations. Consequently, the terms depend on the macroscopic state of the system, specified by $\rho_A(\mathbf{x})$, $\rho_B(\mathbf{x})$ and ϵ_{AB}. Thus, the correction terms ξ_l and ξ_{nl} make the relationship between χ and ϵ_{AB} non-linear.

The long-range contribution may be estimated using a Taylor expansion, as explained

in the Appendix of [49], yielding

$$\xi_{nl} = -\frac{\sigma^2}{2\lambda^2} - O\left(\frac{\sigma^4}{\lambda^4}\right) \tag{4.2-22}$$

$$\sigma^2 = \int K(r) r^2 4\pi r^2 \, \mathrm{d}r \tag{4.2-23}$$

$$1/\lambda[\rho_A, \rho_B]^2 = -\frac{\int \nabla \rho_A(\mathbf{x}) \cdot \nabla \rho_B(\mathbf{x})}{\int \rho_A(\mathbf{x}) \rho_B(\mathbf{x}) \, \mathrm{d}\mathbf{x}} \tag{4.2-24}$$

Here λ is the length scale of variations in the macroscopic component density fields modulated by the amplitude of these variations. For example, for plane wave composition fields with the wavelength L_z and the direction given by a normal vector $\mathbf{e}_z$: $\rho_A(\mathbf{x}) = 1/2 + \alpha \sin(2\pi \mathbf{x} \cdot \mathbf{e}_z/L_z), \rho_B(\mathbf{x}) = 1 - \rho_A(\mathbf{x})$. For $\alpha \ll 1$, as is the case near and above the critical temperature in block copolymers [2],

$$\frac{1}{\lambda^2} \approx \frac{8\pi^2 \alpha^2}{l^2} \quad \text{for} \quad \alpha \ll 1 \tag{4.2-25}$$

When $\alpha = 1/2$, characteristic of moderately segregated block copolymer systems,

$$\frac{1}{\lambda^2} \approx \frac{4\pi^2}{l^2} \quad \text{for} \quad \alpha = 1/2 \tag{4.2-26}$$

The amplitude dependence of $1/\lambda^2$ ensures that ξ_{nl} becomes important only in systems with significant macroscopic phase segregation. Overall, ξ_{nl} quantifies how close the scale of the microscopic scale of the intrinsically model-dependent interparticle potentials, σ, compares to the macroscopic scale of composition variation.

The value of the local excess correlation integral, ξ_l, generally requires numerical evaluation. The key feature of this quantity, measured for a number of common potentials in [49], is that it generally decays in amplitude with increasing $\sigma^3 \bar{\rho}$. For Gaussian potentials, we find that $\bar{\rho}\sigma^3 \approx 2 - 3$, ξ_0 may be systematically reduced to a few percent of ξ_0. Further, ξ_l generally decreases as the concentration of either component in the binary fluids is reduced below 50%. Consequently, ξ_l tends to stabilize more homogeneous phases. Fortunately, we find that the critical miscibility values for different potentials with the same value of $\bar{\rho}\sigma^3$ are consistent to within several percent. Moreover, the critical values of the Flory-Huggins χ parameter for $\bar{\rho}\sigma^3 > 1$ are within 15% the $\bar{\rho}\sigma^3 \to \infty$, or the mean-field limit for the potentials examined. This suggests that the corrections to phase behavior due to ξ_l should

be small and systematic if the potentials are sufficiently wide compared to the interparticle spacing.

Calculation of the precise values of the three components of the correlation integral using Eq. 4.2-18 requires an explicit definition of the smooth density fields in the bead-spring model. Moreover, it requires a mechanism for sampling only particle coordinates consistent with a prescribed set of fields (see Eq. 4.2-14). While the latter is a technical problem, the former poses a fundamental challenge since there is generally no unique way to separate macroscopic and microscopic components of the density fields. One analytically convenient way to do so, proposed by us in [49], involves local averaging of the exact instantaneous density fields. The smoothing filter that accomplishes this, however, is itself not uniquely determined by any physical considerations. This reflects the more general and long-standing problem of picking the cutoff wavelength that defines the boundary between "microscopic" and "macroscopic" in field theories. Wang [17] and Bates and Fredrickson [48] find that the miscibility parameter χ strongly depends on the specific choice1e of the cutoff wavelength in the context of fluctuation corrections to GCM. In practical field-theoretic simulations the cutoff frequency is introduced implicitly by discretizing density and chemical potential fields. The methods for regularizing the ultraviolet divergence of some thermodynamic averages with increasing resolution of the discretization grids in GCM models at finite chain density are just starting to be addressed [15, 47].

An alternative approach to regularizing the density fields explicitly is to consider the identity of full ensemble averages of the excess non-bond energies in Eq. 4.2-10 rather than their instantaneous values. Unfortunately, computational properties of the current field theoretic simulation methods are limited to extremely high chain densities $C \gg 10$ [15, 23] where explicit simulations become difficult, limiting the usefulness of this approach to regularization.

The above approach is practical if we make the mean field approximation for the ensemble average non-bond excess energy

$$\langle U_{AB}[\rho_A(\mathbf{x}), \rho_B(\mathbf{x})]\rangle \approx U_{AB}(\langle \rho_A(\mathbf{x})\rangle, \langle \rho_B(\mathbf{x})\rangle) \qquad (4.2\text{-}27)$$

where the ensemble average fields are given by

$$\langle \rho_K(\mathbf{x}) \rangle = \int \rho_K^*(\mathbf{x}) P(\Gamma) \, \mathrm{d}\Gamma \tag{4.2-28}$$

This approximation generally holds for miscibility that is either substantially higher or lower than the critical value. The critical range of miscibility is known to be relatively narrow in blends and block copolymers when $C \rightarrow \infty$. In block copolymers of realistic molecular weights, however, the critical region is spanning the ranges of experimental interest [3, 42].

In block copolymer literature, it is common to assume that the mean-field approximation holds under all conditions. Adopting this assumption we may define the mean-field miscibility parameter, χ^{MF}. Substituting Eq. 4.2-27 into Eq. 4.2-10, we obtain the following definition of the mean-field χ

$$\chi^{MF} \equiv \bar{\rho} \frac{\langle H_{AB} \rangle}{\int \langle \rho_A(\mathbf{x}) \rangle \langle \rho_B(\mathbf{x}) \rangle \, \mathrm{d}\mathbf{x}} \tag{4.2-29}$$

where all the quantities on the right hand side may be evaluated by simple averaging in molecular dynamics simulations. This estimate provides a point of contact with the extensive field theoretic literature on mean-field GCM at the expense of accurate modeling of composition fluctuations in the critical region [18].

In order to study these fluctuation effects, we need a more general definition. Here, we adopt a simple estimate based on very high and very low miscibility where the mean field assumption does apply:

$$\chi \approx \epsilon_{AB} \big(\xi_0 + \xi_{nl}[\langle \rho_A(\mathbf{x}) \rangle, \langle \rho_B(\mathbf{x}) \rangle] \big) \bar{\rho} \tag{4.2-30}$$

Notice that in for $\chi N \ll 10.5$ [2], the average composition fields are constant, therefore $\xi_{nl} = 0$ and we may estimate ξ_0 as $\chi^{MF}/(\epsilon_{AB}\bar{\rho})$. The ξ_{nl} term serves as the best estimate in absence of explicit definition of instantaneous density fields of the change in χ due to emergence of macroscopic order for χN above the critical value. Thus, the consistency of thermodynamic observables at $\chi N \gg 10.5$ provides an important independent test on the validity of the above estimate. This estimate does neglect long-range correlations in instantaneous macroscopic density fields that are known to be important far below and near the critical χN value [3]. We neglect the local correlation integral ξ_l in this estimate

because it cannot be measured without an independent means of estimating the fluctuation contributions to $\langle U_{AB} \rangle$. Instead, we expect to be able to reduce it to an acceptably small value by choosing $\sigma^3 \bar{\rho}$ significantly greater than one.

4.2.3 Compressibility

As we have explained in the context of particle blends [49], the Helfand incompressibility parameter may be estimated as

$$\zeta = \epsilon_h \bar{\rho} \xi_0 \qquad (4.2\text{-}31)$$

The precise value of ϵ_h is unimportant to phase behavior of block copolymers as long as $\epsilon_h \gg \epsilon_{AB}$ [20, 49]. Therefore, in this work we chose $\epsilon_h N = 600$, unless noted otherwise. This value is at least an order of magnitude greater than the $\epsilon_{AB} N$ values in any of the block copolymer simulation here. An order of magnitude difference in these scales has been found to be sufficient for the interfacial composition profiles in GCM blends to be consistent with the zero compressibility limit to within order of one percent [20] and for doubling of ϵ_h to not produce a statistically significant changes in the the phase diagrams of binary blends of monomers [49].

4.2.4 Bond model

The radius of gyration of an N monomer chain with harmonic spring bonds of average length a_0 in a dense, homogeneous melt is [19]

$$R_g = a_0 \sqrt{\frac{N}{6}} \qquad (4.2\text{-}32)$$

This allow us to deduce the harmonic spring constant for such a chain as

$$k = \frac{3}{2a_0^2} \qquad (4.2\text{-}33)$$

for unit mass monomers. This, in turn, may be related to the dimensionless chain density, C, through the bond length,

$$a_0 = \sqrt{6}(C/(\bar{\rho}\sqrt{N}))^{1/3}. \qquad (4.2\text{-}34)$$

Repulsive interactions between the monomers are likely to expand the bonds somewhat

compared to this estimate. If this swelling is significant, the spring constant may have to be calibrated to attain a desired radius of gyration. Such calibration complicates both the practical application of the model as well as the connection to the GCM, where the Eq. 4.2-34 applies exactly by definition.

Therefore, in this work we use only the value of the spring constant, given by Eq. 4.2-33, and calculate the value of C based on the ideal bond length. This approximation is explored in some detail in the following simulations. To distinguish the actual mean bond length measured in simulations from the *unperturbed* bond length, a_0, we refer to the former using the symbol a.

4.3 Methods

We perform a number of simulations on monomers, dimers, homopolymers, and finally block copolymers to test the limits of the theory presented above. All but the block copolymer simulations are simple canonical MD, with periodic boundary conditions and random walk initial conditions described below. The temperature is controlled using the Kremer-Grest Langevin thermostat with a friction constant set to one in simulation units [60]. Unless noted otherwise, simulations are conducted at unit particle density, $\bar{\rho} = 1$, at unit temperature, $k_B T = 1$, and with unit particle mass, $m = 1$. A Verlet-like integrator was used, with a time step sufficiently small to reduce the error in the temperature to less than 0.5% in all cases. Typical values of the time step were between 0.04 and 0.1, with larger values used for wider potentials.

The phase behavior of physical block copolymers is typically studied by performing temperature scans across critical or phase transition points. Increasing the temperature has the effect of decreasing the importance of energetic non-bond interactions relative to the conformational and translational entropy of the chains. Following Fried and Binder [11] and Grest *et al.*[12], we study this trade-off in series of independent simulations with different values of the excess repulsion, ϵ_{AB}, but with fixed homogeneous repulsion strength ϵ_h and bond constant, k. Note that since energies are expressed in units of $k_B T$, increasing the ϵ_{AB} is equivalent to increasing the inverse temperature. Neglecting the temperature dependence of the homogeneous repulsion, ϵ_h, and the dimensionless chain density, C, is a rough approximation for many experimental systems, but is consistent with the assumptions of the GCM. In practice, if the temperature dependence of ϵ_h and C may be measured and

incorporated in to the model as described, for example, by Bates *et al.*[16],.

In order to save computational time in diblock simulations, we use a relatively small systems of $4.5^3 C$ chains. This corresponds to simulation cells of linear dimensions comparable to a typical lamellar spacing in well-segregated block copolymers. We address the possible effects of using such small cells in the following sections. We also use an external fields to generate lamellar initial conditions. Each simulation is performed in triplicate in order to estimate the confidence intervals on the measured averages.

The specific steps for each simulation in such ϵ_{AB} scans are as follows. First, the lamellar structure is established by imposing an external excess potential $U_{ext}(\mathbf{x}_i) = 2.5(1 + J_i \sin(2\pi\mathbf{x} \cdot \mathbf{e}_z/L_z)/2$, where J_i is 1 when the i-th particle is of type A and -1 when the particle is of type B; L_z is the dimension of the simulation cell in the z direction; and $\mathbf{e}_z$ is the Cartesian unit vector in the z-direction. This step is performed for 50 time units, starting from random initial conditions. Second, the dimensions of the simulation cells are relaxed for 10^4 time units to minimize the virial stress tensor components in all three Cartesian directions using a slight modification of the box-search algorithm of Schultz *et al.*[61]. At each time step, each dimension of the the simulation cell was updated as, $L_i \leftarrow L_i(1+0.1P_i/P)$, where P is the average pressure in the system, and P_i is the magnitude of the diagonal pressure tensor component in the i-th dimension. Although standard isobaric molecular dynamics may be a better approach to such pressure equalization, the Schultz algorithm has the advantage of maintaining constant system volume generally assumed in GCM. The pressures used to calculate the update are exponential moving averages with a decay time of 10 time units. The duration of this relaxation step is an order of magnitude greater than the typical relaxation time of the cell dimensions. Nevertheless, we must note that some much longer lived metastable states were also observed, possibly resulting in incomplete pressure equalization. In these stable and metastable states, the cell dimensions fluctuated by no more than 0.1%, with the magnitude of the fluctuations decreasing with increasing χN. Finally, the system was sampled for $10^5/C$ time units in a straightforward canonical MD. The initial conditions for the sampling runs were created by rescaling the final particle positions after the pressure-equalization steps so that the dimensions simulation cell length, L_z, along the wave-vector of the structure imposed by the external field was equal to its average value over the last 5000 time units of the pressure equalization simulation. Such averaging generally resulted in lower excess energies and more consistent critical points that

those obtained from simply using end point of the pressure-equalization step.

This choice of the sampling time is based on in several test runs (data not reported), for simulations of lamellar block copolymer systems starting with different box sizes to converge to the same lamellar spacing. The sampling time is scaled by the dimensionless chain density to compensate for the growth in the absolute number of chains per simulation box, and consequently the computational time per time step, with increasing dimensionless chain density. Note that the number of chains per simulation cell the dimensions of which are fixed with with respect to the unperturbed radius of gyration, R_g, is proportional to C. While this increases the amount of computation per time step, the relative magnitude of the thermal fluctuations in thermodynamic averages also decreases because the number of molecules in the cell increases. The uncertainty in thermodynamic averages scales approximately as the $1/\sqrt{\tau n}$, where τ is the sampling time and n is the number of chains in the system. Therefore, neglecting the changes in autocorrelation times of thermodynamic variables with C, this implies that the uncertainty in thermodynamic averages maybe kept constant with increasing C if the simulation time is reduced in proportion to the increase in n, which itself is proportional to C. Note that while it is unlikely that the correlation times are independent of the chain density, the effect should be at least partly compensated by the overall reduction in thermal fluctuations with increasing chain density. Still, it is important to note that at least in the ϵ_{AB} scans we do not rely on fluctuations in individual simulations to estimate error bounds on averages.

The unit cell simulations described above are not adequate in cases where the structure functions must be measured. In these cases, much larger simulation cells of $16^3 C$, or approximately $3 - 4$ lamellar periods in each direction, were used. These simulations were particularly time intensive, especially for disordered systems where the fluctuations in the scattering functions are large. Therefore, we limited these simulations to disordered and near-critical systems, forgoing the cell relaxation step. All simulations were started from unperturbed random walk initial conditions and equilibrated for 1500 time steps, and subsequently sampled for 500 time units. The equilibration time is comparable, but greater, than the relaxation time of the systems above the critical point. All simulations were repeated in triplicate.

4.4 Results

4.4.1 Bond model

The first challenge to be addressed by simulations is to quantify the degree of coupling between bond and non-bond interactions. We start by examining the effect of non-bond repulsion on the bond length and radii of gyration of whole chains. This is a crucial step in understanding how to select the bond spring constant in order to achieve a given chain density and ensuring that the Gaussian bond statistics assumed in GCM apply to the particle model.

First, we simulate several A_2 dimer systems with different values of the homogeneous repulsion scale, ϵ_h, as well as bond spring constant. Figure 4-1 indicates that significant deviations from the Gaussian chain bond statistics exist when the repulsion is strong and bonds lengths are close to the interparticle distance. Note that the ideal bond length, a_0,
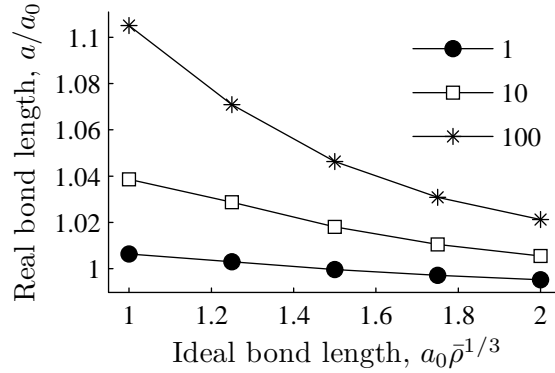
Figure 4-1: Average bond length as a function of the strength of homogeneous repulsion, ϵ_h (in the legend) and the unperturbed bond length in a system of single component dimers with $\sigma\bar{\rho}^{1/3} = 1.3$.

is related to chain density as $(a^3\bar{\rho}) = 6^{3/2}C/\sqrt{N}$. Consequently, the implication of this results is that the ideal bond spring constants may be assumed only when the chain density is sufficiently high and resolution is sufficiently low to guarantee that $(a^3\bar{\rho}) \gg 1$. The effect of non-bond interaction on bond length may be reduced by increasing the range of the potentials, σ, as indicated in Figure 4-2. The reduction is significant only for bond lengths close to $a_0\bar{\rho}^{1/3} = 1$. This highlights a trade-off between computational speed and the expense of additional calibration of the bond model which may be necessary for small σ.
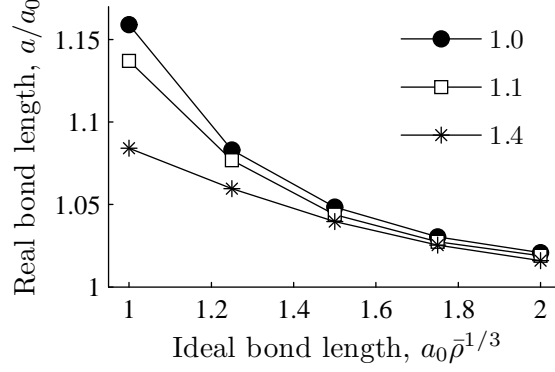
Figure 4-2: Effect of the non-bond potential range, $\sigma\bar{\rho}^{1/3}$, (indicated in the legend) on the bond length in A_2 dimers with $\epsilon_h = 100$. Compare this to Fig. 4-1.
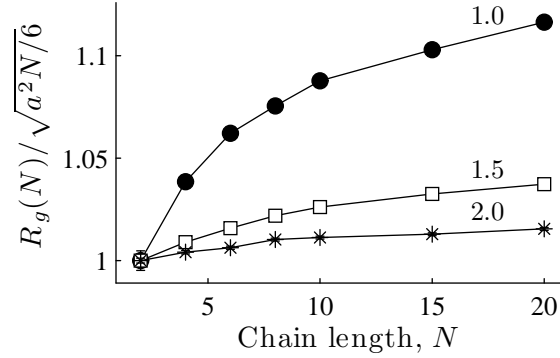
Figure 4-3: Radius of gyration *versus* with the chain length for homopolymers with a fixed unperturbed bond length, $a_0\bar{\rho}^{1/3}$, marked on the curves, showing deviations from the ideal random walk scaling. Note that the radii of gyration are normalized using the bond lengths, a, measured in the dimer systems, rather than the ideal bond lengths, a. Here, $\epsilon_h = 100$, $\sigma\bar{\rho}^{1/3} = 1.0\bar{\rho}^{-1/3}$.

While the stretching of the bonds is a practical challenge, what matters in comparing the bead-spring model to GCM is the scaling of the overall chain dimensions. In GCM, the average radius of gyration of an single component N-mer in a homogeneous melt scales as $\sqrt{N}$. Fig. 4-3 suggests that for resolutions N of order 10, chains are swollen compared to the ideal random walk scaling under the same conditions when individual bonds deviate from ideal statistics. Such non-Gaussian scaling of R_g may be a more appropriate model for behavior of real macromolecules [19], but should be avoided for the purposes of comparison with GCM.

With the effects of the non-bond interaction on the properties of bonds briefly characterized, we proceed to examine the effect of bonds on the correlation integral, ξ in Eq. 4.2-18. We start with a single component system, where $\xi = \xi_0$ by definition. Fig. 4-4
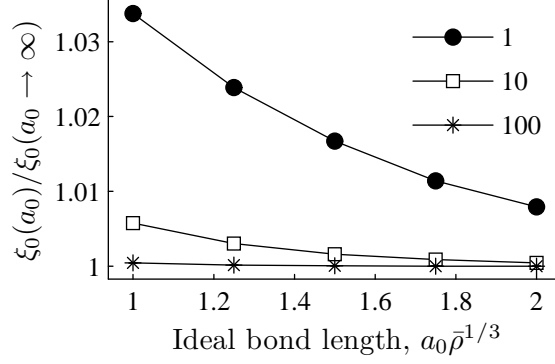
Figure 4-4: Effect of bonds on homogeneous interparticle correlations. The data is for an A_2 dimer system with $\sigma \bar\rho^{1/3} = 1.3$.

indicates in this case the effect of bonds on ξ_0 is significant only when the scales of the bond and non-bond interactions are comparable. For completeness, we also calculate the effect of the potential range σ on this increase in ξ_0. Fig. 4-5 indicates that the value of σ does not play a significant role, at least for relatively high ϵ_h.
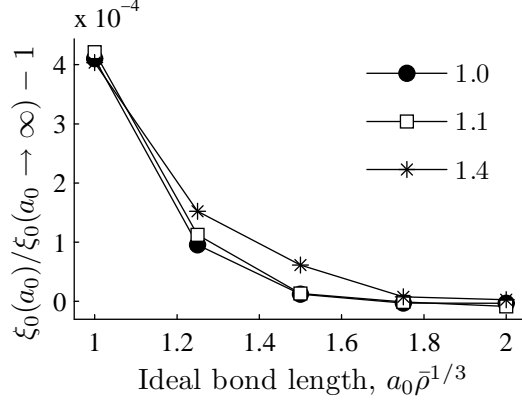
Figure 4-5: Effect of the potential width, σ, on the bond-related artifacts in homogeneous particle position correlation. Data for a A_2 dimer system with $\epsilon_h = 100$.

These conclusions, however, do not apply directly to multi-component systems, as indicated by Fig. 4-6. In this simulation, we measured ξ in an equimolar, single phase mixture of two types of dimers, A_2 and B_2, significantly below and comparable to the critical values of the critical repulsion strength. (The critical repulsion strength in such blends is expected to be somewhat above $\epsilon_{AB} N = 2/\xi_0$ [49].) The significant difference between the correlation integral in the single component mixture and this blend is explained by the effective increase in the local concentration around each particle of its bonded neighbors. Since in this case each particle is bound to one of the same species, the overall effect is to reduce

84
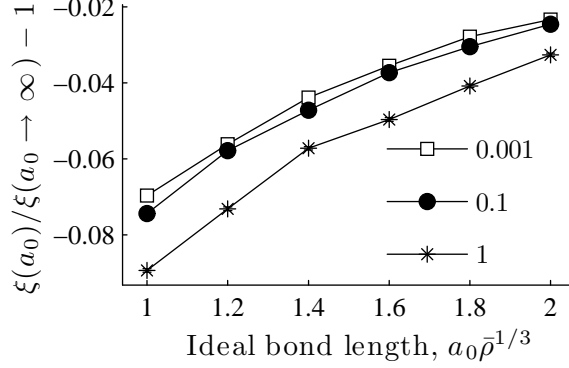
Figure 4-6: Effect of bonds on the correlation integral in a mixture of A_2 and B_2 dimers with values of ϵ_{AB}, indicated in the legend. Here, $\epsilon_h = 100$ for all measurements. Lines connecting the dots are guides to the eye.

the degree to which A and B particles interact. The additional decrease in energy observed for $\epsilon_{AB} = 1$ may be attributed to the excess correlations, ξ_l, close to the critical point, as discussed in detail in [49]. The practical implication of this result is that ξ measured in monomer simulations is a good approximation for polymers only when $a^3 \bar{\rho} \gg 1$. More generally, these result suggest that ξ may be different in blends and in block copolymers. This effect should be negligible when $N \gg 1$ when most bonds are of the same type – either AA or BB – in either kind of system.

4.4.2 Miscibility model

The above results provide sufficient information to formulate a well-parametrized block copolymer model. Our aim here is to quantify the differences among models with different resolutions and potential widths but the same macroscopic (GCM) parameters. We focus on the phase behavior of symmetric diblocks, $A_{N/2}B_{N/2}$ composed of equal number, $N/2$, of A and B beads. Specifically, we consider the time averages of the excess energy, U_{AB}, and the order parameter that is the normalized variance of the time-averaged density of A monomers, $\langle \rho_A^2 \rangle / \langle \rho_A \rangle^2 - 1$. Here, the angle brackets indicate averages of ensemble average fields over the system volume rather than ensamble averages of instantaneous fields. For this study we use a system with a chain density of $C = 2$, corresponding to at least two systematically studied physical materials [32, 33].

The general features of the phase behavior in these systems are illustrated by the data in Fig. 4-7 and are qualitatively similar to the observations in previous studies [11, 12].

(a) Order parameter (b) Excess non-bond energy
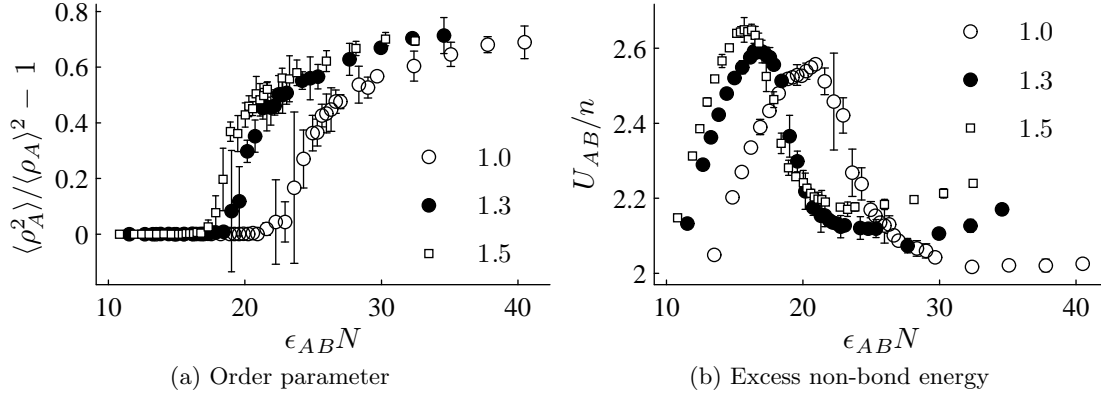
Figure 4-7: Dependence of the variance of the time-averaged density of A particles over the system volume (a) and of the average excess non-bond repulsion energy, U_{AB} per chain (b) on the the excess repulsion, ϵ_{AB}, in $A_{10}B_{10}$ diblocks with $C = 2$ and the values of $\sigma\bar{\rho}^{1/3}$ indicated in the legends. The order parameter used here is the variance in the time-averaged density field of A monomers, $\rho_A(\mathbf{x})$, over the system volume, normalized by the average squared density of A monomers. Error bars are 90% confidence intervals from three independent trials.

As the excess repulsion increases (Fig. 4-7a), the order parameter stays near zero until it begins to rise sharply at the critical point. Notice that the critical values closely correspond to maxima in the excess non-bond energy U_{AB}/n in Fig. 4-7b. These maxima indicate a qualitative departure from random particle mixing, where increasing repulsion strength raises the excess non-bond energy. Increasing the system size to roughly 27 times the size used in these simulations shows no significant change in the width of the energy peak or the position of its maximum (data not shown). This indicates that the correlation length of the fluctuations is significantly smaller than the single lamellar period of the ordered structure (the cell dimension). As the ϵ_{AB} increases further, U_{AB}/n drops sharply while the order parameter continues its sharp rise, signalling the emergence of stable structure where A and B monomers are no longer in contact throughout the entire volume but only at relatively well-defined interfaces. The subsequent minimum in the U_{AB}/n is consistent with the emergence of stable interfaces. The monotonic increase of U_{AB}/n beyond the minimum is consistent with lack of any qualitative changes in the system. The significantly weaker rate of increase in U_{AB} with ϵ_{AB} beyond the minimum reflects the reduced access of the monomers of different types to each other in the phase-segregated state compared to the homogeneous case.

While the overall features of the transitions are qualitatively similar for different σ, they

(a) Order parameter   (b) Excess non-bond energy
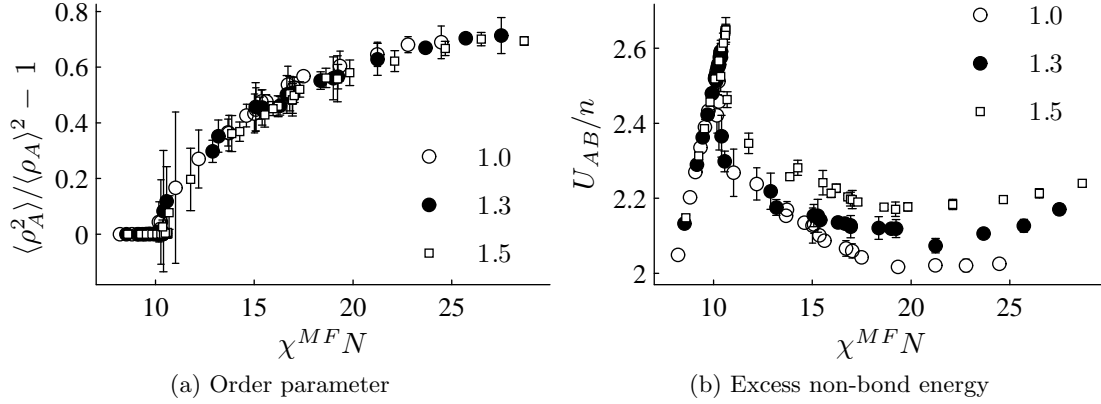
Figure 4-8: The order parameter and average excess non-bond energy data for the symmetric diblocks in Fig. 4-7 plotted against the mean field χN values (Eq. 4.2-29). Note that the order-disorder transition appears at Leibler's mean-field estimate of $\chi_c N = 10.5$ [2].

do show significant quantitative dependence on σ and in this respect are model-specific. These differences, however, nearly disappear when the energy and wavelength data are plotted against the mean-field $\chi^{MF} N$ instead of $\epsilon_{AB} N$ in Fig. 4-8. While the excess non-bond energies U_{AB}/n do show some σ dependence in the ordered regime (Fig. 4-8b), the order parameters agree to within the statistical tolerance of the data in Fig. 4-8a. Note that the critical value of the mean-field $\chi^{MF} N$ is found to be precisely at Leibler's mean-field GCM estimate of $\chi_c N = 10.5$ [2].

The lower values of U_{AB} for lower σ in the ordered regimes reflect the higher degree of local correlations and, consequently, accessibility of more low energy conformations. The differences in energies of the ordered states may indicate that the nature of the ensemble averaged composition profiles across the interfaces depend on σ. An alternative explanation is that for the same average macroscopic composition profiles, the correlations in the positions of A and B particles are different for σ. Specifically, we expect that increasing σ also increases the exposure of each A monomer to B monomers, raising U_{AB}.

As we previously mentioned, the mean-field approximation also allows us to provide a estimate of the local and long-range contributions to the correlation integrals. They are shown in Fig. 4-9 for the diblock with $N = 20$ and $\sigma \bar{\rho}^{1/3} = 1.3$. As expected, the mean-field model does not account for the significant degree of spatial correlations in composition fields, reflected by the drop in ξ_l well below the critical point. This is consistent with the experimental data [42] and field theoretic calculations [3] and generally reflects long-range correlations which are excluded from the mean-field estimate of ξ_{nl}. Notice that above the

87
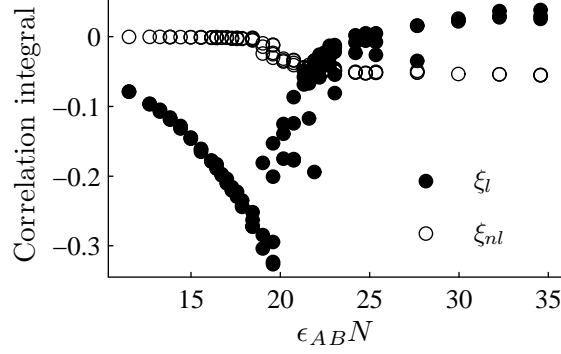
Figure 4-9: Mean-field estimates of the local, ξ_l and long-range, ξ_{nl}, correlation integrals for the symmetric diblock system with $C = 2, N = 20, \sigma\bar{\rho}^{1/3} = 1.3$. The order-parameter and excess energy data for this system are found in Fig. 4-7. For comparison, the homogeneous correlation integral, $\xi_0 \approx 0.82$ here.

(a) Order parameter

(b) Excess non-bond energy
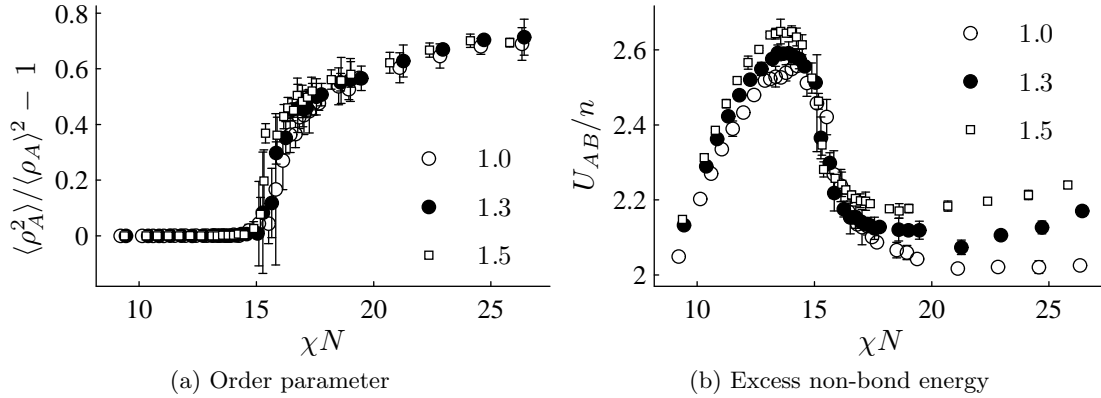
Figure 4-10: Effect of potential width, $\sigma\bar{\rho}^{1/3}$ (indicated in the legends), on the phase behavior of symmetric diblocks with $C = 2, N = 20$. Here, the data from Fig. 4-7 plotted against χN values calculated using Eq. 4.2-30.

critical point, where most of the system consists of relatively pure domains separated by interfaces, ξ_l quickly reaches a positive value in agreement with our previous observations that local correlations stabilize more homogeneous phase [49]. Note that the mean-field estimate is likely to overestimate the correlation corrections, since they are explicitly neglected in the mean-field limit, particularly below the critical χ.

Fig. 4-9 reflects an observation common to all the systems studied here that ξ_l represents only approximately 5% or less of the correlation integral even well above the critical point. This should make any artifacts of our rough mean-field estimate of ξ_{nl} negligible compared to typical uncertainty in experimental data and ξ_l, which is neglected here.

Finally, we discard the mean-field assumption and examine the simulation data in terms
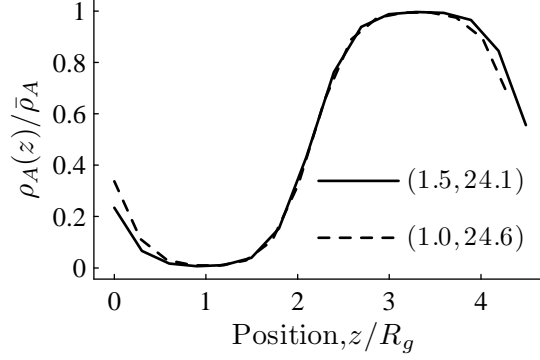
Figure 4-11: Comparison of time-averaged composition profiles ($\rho_A(\mathbf{x})$ along the wavevector of the field) in two diblock simulations with different σ but comparable χN. The legend indicates the pair of values ($\sigma \bar{\rho}^{1/3}, \chi N$) for the two examples.

of the χN as given by Eq. 4.2-30. Fig. 4-10 indicates that the models with different potential widths retain a similar degree of consistency in terms of χN as in terms of χ^{MF}. As expected, the thermal fluctuations excluded by the mean-field approximations increase the critical values of χN [3]. The significant dependence of U_{AB}/n on σ may suggest that the macroscopic states of the systems also significantly depend on σ, despite the close correspondence of the order parameters. Fig. 4-11 indicates that the average density fields in models with different σ but the same χN are nearly identical, in agreement with the order parameter data. Therefore, the differences in U_{AB}/n above the critical point in Fig. 4-10b should be attributed to instantaneous correlations in composition fields, rather than properties of average composition fields. This is consistent with the observation that the energies tend to be higher for wider potentials, which should increase the length-scale of instantaneous correlations between $\rho_A(\mathbf{x})$ and $\rho_B(\mathbf{x})$.

We conclude this section by examining the effect of resolution on the phase behavior of diblocks with the same macroscopic parameters. Fig. 4-12 indicates that decreasing the resolution from $N = 20$ used in the previous scans to $N = 8$ has a negligible effect on the order parameter or the critical point, but does appear to lower U_{AB}/n appreciably above the critical point. This is surprising, since lowering the resolution at fixed $\sigma \bar{\rho}^{1/3}$ effectively increases the width of the interaction potentials relative to the molecular scale. This may be attributed to the failure of the simple Taylor expansion used to obtain Eq. 4.2-22 for high σ/R_g. Fortunately, U_{AB}/n increases, as expected, from $N = 20$ to $N = 14$, indicating that $N = 20$ is indeed sufficiently high for Eq. 4.2-22 to be a reasonable estimate of ξ_{nl}.

(a) Order parameter   (b) Excess non-bond energy
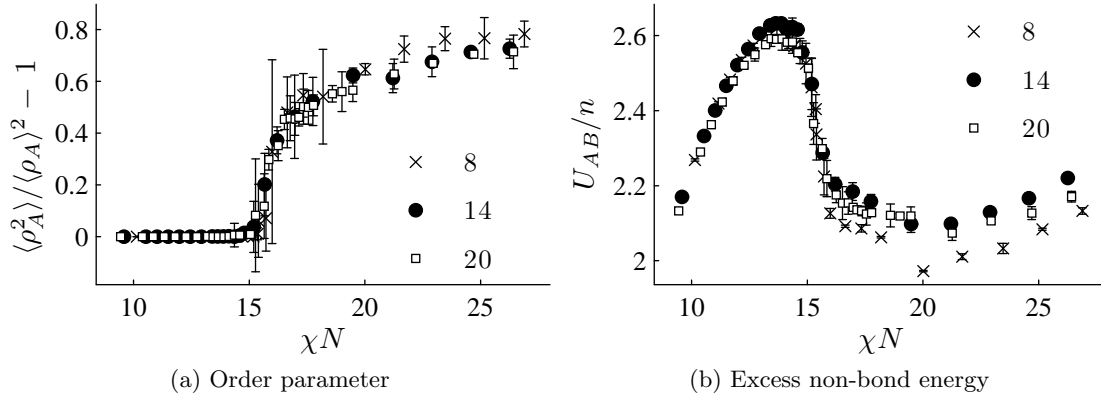
Figure 4-12: Effect of resolution, N, marked in the legend of each plot, on the order parameter (a) and average excess non-bond energy per chain, U_{AB}/n (b) in a symmetric diblock melt with $C = 2$ and $\sigma\bar{\rho}^{1/3} = 1.3$. Note that the data for $N = 20$ is the same as that for $\sigma\bar{\rho}^{1/3} = 1.3$ in Fig. 4-10.

4.4.3   Comparison to experimental results

The consistency of the simulations with different potential widths and resolutions demonstrated above provides a reasonable assurance that the properties of the our bead-spring diblocks indeed reflect universal features of diblock copolymers. This finally allows us to carry out a meaningful comparison of the model with GCM and experiments for which the GCM parameters have been measured.

First we compare our predictions of the critical value of $\chi_c N$ as a function of chain density, C, to those of the perturbation treatments of GCM for finite density. The so called BLHF estimate of this value is commonly used to measure χ values experimentally [16, 24]. The central assumption of the BLHF theory that only the amplitude of thermal composition fluctuations of a constant wavelength need be considered has been subsequently relaxed by Barrat and Fredrickson (BF), resulting in a more general prediction of the critical value [3].

We define the critical point in the simulations as the smallest χN where the order parameter $\langle \rho(\mathbf{x})^2 \rangle / \langle \rho_B(\mathbf{x}) \rangle^2 - 1$ surpasses 0.01 indicating the emergence of stable order [21]. Increasing this threshold value to 0.1 resulted in an increase of roughly 0.5 (data not shown) in $\chi_c N$, however, the lower threshold is more in line with traditional definition of the critical points. Confidence intervals on critical values are estimated using three independent estimates for each density.

Fig. 4-13 shows the results. Overall, the simulations fall on the BLHF curve to within
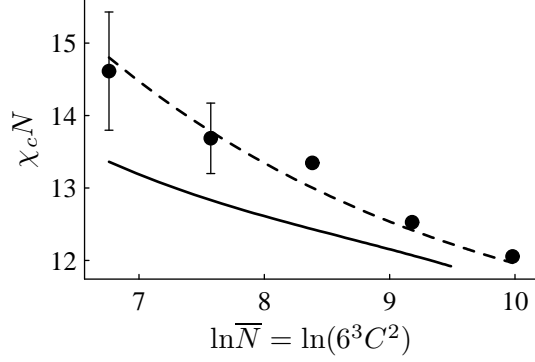
Figure 4-13: Comparison of the critical χN values for symmetric diblocks as a function of dimensionless chain length, $\bar{N} \equiv 6^3 a_0^3 \bar{\rho} N$. Dashed line: BLHF theory; solid line: Barrat-Fredrickson theory [3]; points: simulation data, with 90% confidence intervals based on three independent sets of simulations.

measurement precision. To our knowledge, this is the first test of either theory where the χ parameters were measured independently. The Barrat-Fredrickson theory is a generalization of the BLHF theory and should be more precise, although, its assumptions of neither theory are strictly justified at chain densities considered here [3]. One reason the simulations results may be higher than the Barrat-Fredrickson theory is that we have chosen the order parameter threshold to be too high. Another possibility is that the simulations allow for three-dimensional long-range composition correlations which stabilize the disordered phase relative. The Barrat-Fredrickson theory considers only plane-wave composition fluctuations, which would tend to underestimate the critical point.

Next we consider the wavelength of the position in the scattering peak of poly(ethylene-propylene)–poly(ethyl-ethylene), or PEP-PEE, diblock copolymers as a function of molecular weight at a fixed temperature, shown in Fig. 4-14. This experiment has been also studied by Barrat and Fredrickson, providing not only a GCM perturbation prediction for the wavelength but also experimental values for monomer density and statistical bond lengths. This allows a comprehensive test of our model.

We conduct comparable measurements on a series of $A_{10}B_{10}$ diblocks with $\epsilon_h = 30, \sigma\bar{\rho}^{1/3} = 1.3$. The excess repulsion strength is set to $\epsilon_{AB} N = \chi N' / \xi_0 (C/C_c)^2$, where $\chi = 0.0168$ is the experimentally measured value and N' is the polymerization index in terms of the chemical repeat as described by Barrat and Fredrickson [3]; $\xi_0 = 0.87$ is the estimate of the correlation integral measured in simulations of a homogeneous system of disconnected
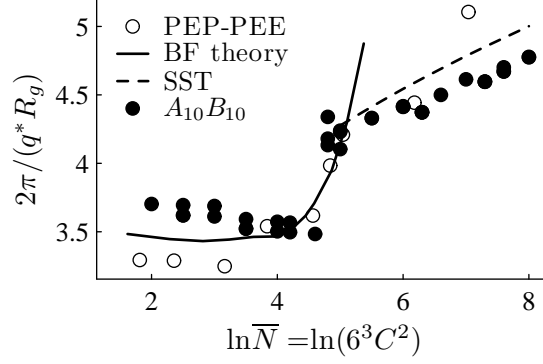
Figure 4-14: Wavelength of the structure function peak position as a function of the dimensionless chain density for PEP-PEE [4] compared with predictions of the field theoretic perturbation treatment of GCM [3], the strong segregation theory of Helfand *et al.*[2], and simulation data. Data below the critical point were obtained from smeared scattering function peaks, while above they were taken as the lamellar periods in pressure-equalized unit-cell simulations.

model monomers; $C_c = 4.6$ is the experimental value of the critical density measured in the PEP-PEE experiment. (Subsequently, we determined that the bonds reduce the value of ξ_0 to approximately 0.82. This discrepancy shifts the critical chain density slightly in our simulations.) Here the disordered state peak positions were obtained from structure factors. To emulate the smearing due to the bandwidth of the X-ray source in the experiment, we convolve the measured structure factors with a Gaussian filter with a standard deviation equal to 0.25 of the value of the wavelength at the peak of the filter function [42]. Above the critical point, we used the lamellar period in pressure equalized samples as the estimate of the structure function peak position. This allowed us to use significantly smaller simulation cell sizes and avoid the artifacts associated with fast Fourier transform calculations in finite cells.

Considering the uncertainty of the experimental values and the fact that no adjustable parameters were used, the agreement of our results with the data and BF predictions is remarkable. Notice that the BF theory starts to deviate significantly from the experimental data for ordered samples, reflecting the limitations of the perturbation treatment. Simulation data, however, remain consistent with the experiment. Remarkably, our results indicate that the peak position achieves the narrow interphase approximation, NIA, scaling behavior even at weak segregation even though NIA is based on the assumption of sufficiently strong segregation that the interface width is negligible compared to the domain widths [2, 20]. This is significant not only in confirming the universality of the behavior of

the particle model, but also indicates that the simple, explicit NIA prediction may turn out to be accurate well outside of its rigorous range of validity.
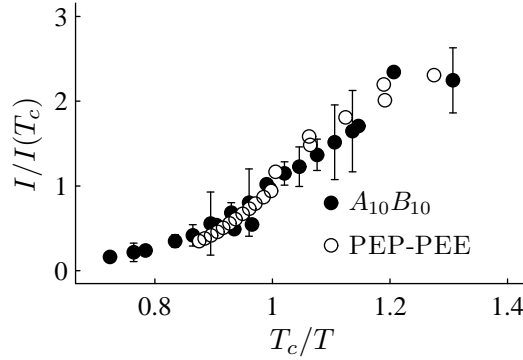
Figure 4-15: Include comparison of the peak scattering intensity between simulated ($A_{10}B_{10}$) and PEP-PEE-5 system described by Bates *et al.*[4]. Note that in the simulated model, $\chi/\chi_c = T_c/T$.

Finally, Fig. 4-15 compares the simulation precision of the the peak scattering intensity, I, as a function of inverse temperature to those measured for a PEP-PEE sample by Bates *et al.*[4]. Recall that under the assumptions of our model, varying χN at constant temperature is equivalent to varying the inverse temperature. To minimize the uncertainty in the experimental data due to the smearing of the scattering function, we normalize both the intensity and inverse temperature by their critical values. The critical value of χ_c used to normalize the simulation data was used as an adjustable parameter to superimpose the curves. Minimizing the sum of squared residuals between linear interpolations of the two curves resulted in $\chi_c N = 13.6$. This value is only approximately 5% higher than the prediction $\chi_c N \approx 13$ predicted independently in Fig. 4-13, further establishing the reliability of our simulation approach.

4.5 Discussion

The main implication with regard to particle-based models is that attaining straightforward and explicit mapping among models with different resolutions and interaction potentials is possible only within certain bounds on the resolution of the model. On one hand, the resolution must be sufficiently high to allow for a meaningful separation of the macroscopic and microscopic features. On the other hand, the resolution must be sufficiently low to allow decoupling of bond, homogeneous non-bond, and excess non-bond interactions. The upper

bound on resolution is set by the requirements that the width, σ, of the potentials is such that $\sigma\bar{\rho}^{1/3} > 1$ and the number of particles per chain, N, is such that $a^3\bar{\rho} = \sqrt{6}^3 C/\sqrt{N} \gg 1$. Here, we have successfully used values of $a^3\bar{\rho}$ as low as 3, which was possible due to relatively soft and wide-ranged repulsion potentials. As we have previously discussed [49], not meeting the first condition results in the dominance of local correlations over the homogeneous ones. Consequently, the value of χ associated with a given excess repulsion depends on the local composition. Moreover, this composition dependence depends on the nature of the monomer interactions, rather than universal, macroscopic model properties.

It is interesting to note that if each monomer is interpreted literally as a representation of long section of a flexible macromolecule [49], the lower bound on bond length and σ become identical. In this case, it is reasonable to assume that σ is comparable to the unperturbed radius gyration, $R_g/\sqrt{N}$, which is equal to $\sqrt{6}a_0$.

Despite this similarity between the restriction on bond lengths and potential ranges, the artifacts of violating the two conditions compound as increasing resolution eventually shortens bonds to the point where bond interactions strongly affect local particle position correlations. This also leads to the breakdown of ideal Gaussian chains statistics of the whole chain radius of gyration. Consequently, both the miscibility parameter and the bond strength become resolution dependent and must be calibrated numerically at each resolution to attain a particular dimensionless chain density. This observation is particularly significant for lattice chain simulations, where bond lengths are often exactly equal to the lattice spacing.

The fact that the bead-spring models are meaningful only at a coarse resolution, corresponding to a upper bound on N, is hardly a new idea in itself [20]. However, our analysis highlights some notable details particularly important for coarse-grained bead-spring models, where the microscopic length scale is typically much larger than the dimensions of a chemical repeat unit. First, we introduce the concrete definition of the microscopic and macroscopic length scales, σ and λ, and define precisely how the macroscopic contribution to the miscibility parameter scales with the ratio of the two. In contrast, a quantity analogous to σ, the cutoff frequency, arising in field theoretic approaches of GCM is generally left as a free parameter [17, 48]. Second, while similar to our previous analysis, the definition of λ here relies on purely macroscopic density fields, rather than the instantaneous local fields. This has a third, practical, consequence in that the macroscopic contribution,

ξ_{nl}, to the correlation integral ξ is negligible. In contrast, our previous definition not only had the drawback of relying on the implicitly defined smoothing kernel but potentially non-negligible values of ξ_{nl} even in disordered states.

While these problems may be addressed, in principle, by the recently developed field theoretic polymer simulations methods (FTPS) of Fredrickson *et al.*[18], the explicit chain simulation methodology developed here emerges as a viable and necessary complement to such methods. As noted by Fredrickson *et al.*, sampling thermal fluctuations becomes more difficult in FTPS at lower chain densities. As a result, to our knowledge, there are no systematic studies of block copolymers in the GCM-FTPS framework for $C < 10$, which accounts for a significant part of experimentally work on block copolymers [4, 16, 32, 33]. In contrast, the explicit chain simulations require fewer calculations for lower chain densities as the number of chains per unit cell of an ordered structure is proportional to the dimensionless chain density. Moreover such simulations in the experimentally relevant range of chain densities are feasible on readily available computers, as demonstrated by the results reported here.

Our results are distinguished from from similar studies of Fried and Binder [11] and Grest *et al.*[12] by the thorough characterization of the chain densities and miscibility parameters in our model with respect to GCM. While qualitative trends in domain sizes and critical behavior observed in our simulations are the same as in the previous works, the reliable definitions of the model parameters allows us to compare our results to the predictions of the GCM and observations on real polymers directly and quantitatively across a range of conditions.

At this point it is appropriate to discuss several issues raised, but unresolved by our results. First, we must note the systematic difference between the critical χ values observed in particle simulation and BLHF predictions. The discrepancy may be explained by the fact that local correlations in the disordered state are not allowed in the BLHF theory, but are explicitly considered here. As discussed in [49], these correlations stabilize disordered phases, raising the apparent critical χN somewhat. In the meantime, the discrepancy should not prevent application of the explicit chain simulation methodology we propose to the study of GCM since it is systematic and appears to follow the same qualitative trend as the GCM estimates. Moreover, at less than 10% of the value of χ_c, the discrepancy is small compared to the typical uncertainty in measured polymer parameters as well as the

rigorous error bounds on the BLHF predictions [3].

Second, it is important to whether the bead-spring models are as consistent transitions between different field symmetries observed in asymmetric block copolymers as they are near the critical point of the symmetric diblocks [2, 32]. It is commonly assumed that the effect of thermal fluctuations in asymmetric block copolymers may be adequately described by shifting the mean-field diblock phase diagram of Matsen and Bates [2] to attain the correct critical point. This assumption has not been tested in any framework that adequately sampled the effects of thermal fluctuations and is of practical importance.

Third, our composition field averaging method, in principle, may be confounded by translational or rotational drift of an ordered structure with respect to the simulation cell. This observation also applies to other explicit chain simulation methods as well as FTPS. Fortunately, the high degree of consistency between independent simulations of identical systems, and those differing in resolution, potential width, and density reported here indicate that proper momentum conservation is sufficient to eliminate the artifacts of drift. Nevertheless, it is important to consider other order parameters in addition to $1/\lambda^2$, such as average of instantaneous composition correlation functions. Alternatively, we may introduce a sampling methodology based on boundary conditions that force a particular structural orientation. Yet another means of avoiding drift and rotation are available in field theoretic calculations, where the basis set used to represent density fields to be explicitly restricted to attain particular orientation and phase shift of periodic structures.

Fourth, this study focuses on a practically important but rather small range of resolutions and potential widths. Although extending our study to a broader range of resolutions and potential widths, particularly high resolutions, is important, we may anticipate some challenges of such extensions. Increasing the resolution at constant density must either be accompanied by an increase in the interaction range or a break-down in the universality of the model behavior and increasingly composition-dependent miscibility. The former should lead to increased computational demands while the latter would required additional calibration calculations for rigorous estimates of the macroscopic parameters. Nevertheless, it is interesting to note that the excess energy observed by Grest *et al.*in a diblock copolymer systems with a resolution of $N = 100$ and hard-core potentials is very close to our estimates, obtained at a much lower resolution [12].

Finally, we must mention the issue of finite size effects since we effectively simulated

systems only a single lamellar period across. While this may be important in absolute measurements, here our main concern was with consistency of observations for different explicit chain models with GCM. Notably, both results on fluctuation-corrected GCM to which we could compare our work also rely on single harmonic representation of ordered phases. Therefore, the unit cell simulations performed here are in fact appropriate. Moreover, as we have mentioned some limited test comparison between large cell simulations and unit-cell simulation revealed no differences in the excess energy dependence on χN up to the critical point, including the position of the maximum. At the same time, we must emphasize that pressure equalization is absolutely crucial for consistency of simulation of ordered phases, even those near the critical point.

While these issues warrant further investigation, there are a number of theoretical and practical considerations emphasized by this study that are relevant in the broader context of polymer science and physics. For instance, it is interesting to note that explicit chain simulations of the kind studied here are literally a discrete version of the GCM. The relationship between the two is analogous to that between the discrete representation of path integrals and Shr odinger's wave function equations in quantum mechanics [22, 31, 62]. In fact, for infinite chain density, $C \rightarrow \infty$, we may follow Feynman in taking the limit of infinite resolution, $N\sigma \rightarrow \infty$, and recover the exact traditional formulation of GCM [18]. This is possible because when $C \rightarrow \infty$ interparticle spacing may be treated as infinitesimally at any resolution, removing the upper bounds on resolution described here.

More generally, our study formalizes the assumption involved in taking the limit of infinite resolution, N, at finite dimensionless chain density. This is a significant fundamental problem considering the recent emergence of FTPS methods for sampling GCM, where the resolution is infinite by definition, at finite dimensionless chain density. In providing a consistent way to compute miscibility and bond strength as function of resolution we have provided an explicit scheme for determining the parameters of the bead-spring model as functions of resolution. This is, in effect, a concrete renormalization procedure. The limits on resolution discussed in the first paragraphs of this section allow us to specify explicitly the values of the repulsion and bond strengths as functions of resolution. Our analysis suggests that the limit of infinite resolution may be carried out for finite chain density explicitly as long as the potential widths are kept sufficiently high. The same effect has been achieved in FTPS by sampling the density fields on finite grids or explicitly subtracting contribution

of high-frequency field correlations to thermodynamic averages [47]. However, a systematic understanding of the issue in the FTPS framework is only starting to emerge.

In the meantime, the explicit chain simulation methodology developed here offers the first practical way to eliminate the uncertainty due to the unrealistic approximations, such as the RPA, often necessary in evaluating the GCM. It is well known that traditional approximate treatments of GCM result in considerable inconsistencies of measured χ parameters, limiting the quantitative application of the theory [16]. As our results indicate, using explicit chain simulation for prediction and parameter estimation allows us to eliminate these approximations at realistic chain densities.

Finally, a well-parametrized particle model may offer unprecedented opportunities in studying rheology of heterogeneous melts. For example, straightforward non-equilibrium molecular dynamics sampling algorithms may be applied directly to our model to assess the low frequency contribution of composition correlations to viscoelasticity [18, 63]. More detailed reptation effects may also be addressed either by increasing the resolution [12] or explicitly disallowing chain crossing in a low resolution model [64]. While such simulations have previously in themselves have been possible, now they may be firmly placed in the thermodynamic context.

4.6 Conclusions

Overall, we may conclude that it is indeed possible to construct a coarse-grained bead-spring block copolymer model that is precisely parametrized in terms of the standard Gaussian model. The existence of such a relationship, and universality of the phase behavior of the particle model, however, requires that, on one hand, the resolution of the model be sufficiently low that the bonds and range of the non-bond interaction potentials are greater than the characteristic interparticle distance and on the other, sufficiently high for the length scale of macroscopic composition fluctuations to be significantly lower than the range of the potentials. As we have demonstrated, this balance may be effectively struck for even relatively low molecular weight block copolymers. Thus, continuous-space coarse-grained particle-based simulations emerge as a straightforward, viable, and rigorous alternative to field theoretic simulations, particularly in addressing thermal fluctuation and, potentially, non-equilibrium properties of block copolymers of realistic molecular weights.

5

Concentric lamellar phase of block copolymers confined in cylinders

Abstract

This article reports a detailed modeling investigation of the concentric lamellar (CL) phase of block copolymers confined in cylinders. It is motivated by recent experimental observations of the CL phase in electrospun fibers and the reported failure of the classic strong stretching theory (SST) in the CL case. The equilibrium morphology and dimensions of CL phases are explored in detail as functions of the cylinder diameter. Quantitative results are obtained in a series of molecular simulations of bead-spring chains and explained in terms of a free energy model based on the narrow interphase approximation (NIA). The analysis brings into focus the importance of interpenetration between monolayers of diblocks and variation in interfacial chain density and, hence, interfacial energy density, with domain widths in determining the properties of the CL phases. Simulations reveal three keys features of CL systems. First is that the dimensions of the domains closer to the axis vary with the overall cylinder diameter significantly more than those farther out, in agreement with similar observations in other computational works. Second is that the domains tend to be thinner and chain dimensions smaller in CL phases than in the unconfined flat film cases. Third is that increasing the cylinder diameter produces periodic second order symmetry-breaking transitions where the central monolayers flatten from cylindrical into ribbon-like concentric monolayers. These phenomena are explained in terms of the interplay of chain conformational entropy and interfacial energy, including effects specific to curved interfaces. (At the time of writing, this material in this chapter is review for publication as an article in the *Journal of Chemical Physics*.)
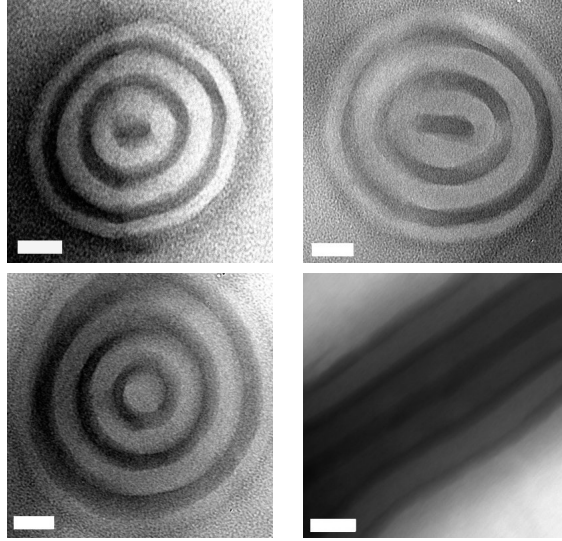
Figure 5-1: Typical axial and longitudinal electron transmittance (TEM) views of polystyrene–polydimethylsiloxane fibers [5, 6]. Polydimethylsiloxane is dark; scale bars are 56 nm, corresponding to the lamellar period, L_0, of this material in the unconfined case.

5.1 Background and introduction

Confining block copolymers to cylinders, such as pores or fibers, has been shown to expand the range of self-assembled morphologies of these materials [37]. While active theoretical [37, 65, 66] and experimental [6, 67] research efforts are under way to explore the full range of these morphologies, one of the simplest and commonly observed cases reveals some remarkable properties. This morphology is described as the concentric lamellar (CL or $L_{||}$) phase and is illustrated in Fig. 5-1. The CL phase forms in nearly symmetric block copolymers when one of the blocks preferentially adsorbs to the confining wall [37, 66]. It is made up of concentric monolayers of diblocks.

One notable property of CL systems is that only the central one or two domains change their thicknesses in response to changing cylinder diameter, while the widths of the rest of the domains remain fixed. Similarly, the number of concentric monolayers in the equilibrium structure remains constant over a range of cylinder diameters comparable to chain dimensions. Such behavior has been reported in lattice chain models [66] and confirmed experimentally in fibers [6]. These properties are important from the technological point of view, as they could allow production of materials with very consistent properties without requiring precise control of the confining medium. The way CL phases adapt to incom-

100

mensurable confinement is also interesting from the point of view of fundamental polymer science, since it is a qualitative deviation from the case of thin films. In contrast to CL systems, all of the layers in flat films are more or less equivalent and adapt equally to changes in film thickness [68, 69].

At first glance, the CL phase appears to be a trivial modification of the exhaustively studied lamellar phase. However, the effects of confinement mentioned above have defied attempts at precise explanation. The currently accepted theory of block copolymer films confined between flat substrates is based on the strong stretching theory (SST), which has successfully accounted for the experimental observations [68, 69]. Extending this approach to the CL phase fails, as has been recently demonstrated by Wang [70]. Specifically, the SST model incorrectly predicts the order and location of transitions between CL phases with different number of concentric monolayers. Moreover, the SST does not account for the one property of CL phases on which there is a reasonable agreement in the literature: the disproportionate sensitivity of the central domain widths on the diameter of the confining cylinder.

It is difficult to diagnose these shortcomings of SST based on the available simulation and experimental data largely because the data is sparse and inconsistent. For example, there is no agreement on whether the confinement causes an increase in domain width or whether the chains themselves are compressed or expanded. The experimental study of Shin *et al.*[67], as well as lattice chain simulations of Yu *et al.*[66] show that the domain widths are increased by confinement. More recently, Ma *et al.*[6] found that in CL-forming polystyrene–polydimethylsiloxane electrospun fibers the central domains are relatively large, but the rest are slightly smaller than in the unconfined case [6]. In contrast, Li *et al.*[65] concluded on the basis of mean field calculations that under confinement all domains are thinner than in the unconfined case, although the central domains are wider than the outer ones. Similar calculations by Sevink *et al.*[71] indicate that the chains near the axis are considerably compressed with respect to the unconfined copolymer. Such compression is also suggested by the lattice chain study of Wang [70]. These simulations indicate that the increase in domain widths relative to the unconfined copolymer values does not necessarily correspond to stretching of the chains themselves. For example, Yu *et al.*[66] have found end-to-end distances both above and below the unconfined copolymer values in systems with significantly expanded central monolayers.

These disagreements may simply reflect the focus of the studies to date on exploring the variety of morphologies stabilized by confinement rather than detailed investigations of any single morphology. The lattice chain simulations of Wang are a notable exception in this regard [70]. Another limitation of existing studies, including Wang's, is that they consider no more than two to three concentric monolayers. Finally, inconsistencies in the literature may stem from the differences in model assumptions, particularly with regard to the extent of thermal fluctuations [18]. While mean field calculations ignore these fluctuations entirely, lattice chain studies typically allow them to be unphysically large, since computational demands restrict these studies to chain densities characteristic of systems with very low molecular weights.

To address these concerns, we conduct a molecular dynamics study of the CL phase in a model system of bead-spring block copolymers inspired by the Kremer-Grest models [12, 55, 60]. Specifically, we conduct a series of independent simulations for a range of cylinder diameters. The data on variation of equilibrium morphology with cylinder diameter obtained from these simulations is then used to construct and validate a high-level free energy model. The ultimate aim of this high-level description is to understand how interfacial curvature affects the free energy balance determining the domain dimensions and morphology as well as chain conformations in the CL phase.

5.2 Definitions

We consider a system of AB diblock copolymers enclosed in an infinitely long cylindrical cavity inside a rigid matrix, illustrated in Figure 5-2. The wall of the cavity is a perfect cylinder of radius R and diameter D. The A and B blocks are assumed to have the same partial volume, compressibility, mass, and unperturbed radii of gyration. The matrix is made up of B homopolymers of the same molecular weight as the diblock, ensuring that B blocks adsorb to the cylinder wall in all cases considered here. In order to simulate a solid matrix, the homopolymer is kept from diffusing into the system as described in the Methods section.

The system is made up of Z diblock chains, and each chain consists of N monomers. When the CL phase is stable, the chains self-assemble into n concentric monolayers. This CL system is characterized by total and component monomer density fields, $\rho(\mathbf{x}), \rho_A(\mathbf{x})$, and $\rho_B(\mathbf{x})$, as well as the average monomer and chain densities, $\bar{\rho}$ and $\bar{\rho}/N$. While all simulations
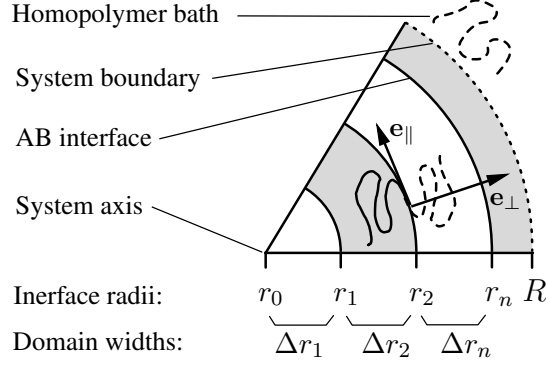
Figure 5-2: A schematic view of a slice of a CL system viewed along the axial direction, illustrating the definitions used in this paper.

are carried out in three dimensions, we focus on the radial and azimuthal variation in domain shapes. Thus, reported density fields are averages over the axial dimension.

Of particular interest here are the radii, r_i, of the AB interfaces and the domain widths $\Delta r_i = r_i - r_{i-1}$ as functions of the cylinder diameter. We define an interface as the radial position r_i where the average concentrations of A and B monomers are equal: $\rho_A(r_i) = \rho_B(r_i)$. Also, for consistency of notation, we let $r_0 \equiv 0$. An unfortunate property of this definition is that r_0 does not correspond to an interface. Thus, the width of the central domain, $r_1 - r_0$, is more closely analogous to a half-width of a domain enclosed between two parallel interfaces in the unconfined lamellar phase.

Note that for systems that are not perfectly cylindrical, r_i is a function of the azimuthal angle, θ. To avoid the resulting ambiguity of definitions, we define r_i as the radius of a circle with the same area as that enclosed by the projection of the i-th interface onto the cross sectional plane of the cylinder. Thus, $\pi r_i^2 h$ is the volume enclosed by the i-th interface. We will also use the notation $r_i(\theta)$ when the interface radius is specified as a function of the azimuthal angle, θ.

We also examine the surface density, $s(r)$, of chains at a given radial position, r, from the fiber axis. This is defined as the number of chains crossing a cylindrical shell of radius r around the axis divided by the area of the shell. A shorthand notation is used for surface densities at the interfaces: $s_i \equiv s(r_i)$.

Properties of single chains are described using a local Cartesian coordinate system, whose tangential and normal unit vectors, $\mathbf{e}_\parallel$ and $\mathbf{e}_\perp$, are indicated in Fig. 5-2. The origin of this coordinate system is chosen to be at the center of mass of the chain and the axial

103

unit vector is parallel to the cylinder axis. The $\mathbf{e}_\perp$ lies along the normal to the AB interface at the point nearest to the chain center of mass.

Unless noted otherwise, energies are reported in units of $k_B T$, lengths in units of $\bar{\rho}^{-1/3}$, and masses in units of m, the mass of a single particle, or a monomer, in the simulated molecules. This implies a time unit of $\sqrt{m/k_B T}\bar{\rho}^{-1/3}$. For reference, the Rouse relaxation time of the chains in homogeneous systems, where A and B blocks are equivalent, is of order 10–100 time units.

5.3 Simulation method

We conduct canonical molecular dynamics simulations of bead-spring polymers with soft non-bond interactions, following Kremer *et al.*[57, 60], along with a novel implementation of the impenetrable wall boundary condition. Each chain is made up of $N = 10$ particles. The dimensionless chain density, $C = (\bar{\rho}/N)R_g^3 = 2$ was used in all simulations reported here, where R_g is the unperturbed radius of gyration of the chains. This chain density corresponds, for example, to polystyrene chains of roughly 21 kg/mol. R_g may be calculated from the statistical monomer, or bond, length a, as $a\sqrt{N/6}$.

Using a realistic value of C is a significant distinguishing feature of this study. As discussed by Fredrickson *et al.*[18], the C is a Ginsburg parameter characterizing the importance of thermal fluctuations in the thermodynamics of the system. The classic self-consistent field theory of Gaussian chains corresponds to $C \to \infty$, while typical experimental systems have $C = 2-10$, allowing significant fluctuations. At the same time, in common lattice chain studies C is less than 1, often corresponding to systems with molecular weights of order 1 kg/mol.

5.3.1 Energy model

The particles, or monomers, of each molecule are connected by harmonic springs. The particles also interact through non-bond potentials that describe the incompressibility of the system as well as the immiscibility of the blocks. Specifically, the effective Hamiltonian

used here was

$$U(\{\mathbf{x}_i\}) = \sum_{i,j>i} u(r_{ij}) + \sum_{(i,j)\in\mathbf{B}} Kr_{ij}^2 \qquad (5.3\text{-}1)$$

$$r_{ij} = |\mathbf{x}_i - \mathbf{x}_j| \qquad (5.3\text{-}2)$$

Here, $\mathbf{x}_i$ is the position of the i-th particle, $\{\mathbf{x}_i\}$ is the set of all particle coordinates, and the indices i, j in the first sum run over all the particles. The second sum is carried over the unique pairs of indices of bonded particles, denoted by a set $\mathbf{B}$.

The spring constant, K, is calculated assuming that the particles represent equally spaced points along an ideal Gaussian chain [19]:

$$K = \frac{N}{4R_g^2} \qquad (5.3\text{-}3)$$

Here R_g is the ideal radius of gyration, measured in homopolymer simulations where no distinction between A and B monomers was made. In the system used here, this choice of K is self-consistent in that the radii of gyration observed in the homopolymer simulations are very close to the value of R_g used to set K.

The non-bond interactions are purely repulsive and Gaussian in shape:

$$u(r_{ij}) = \epsilon(i,j) \left(\frac{3}{2\pi\sigma}\right)^{\frac{3}{2}} \exp\left(-\frac{3r_{ij}^2}{2\sigma^2}\right) \qquad (5.3\text{-}4)$$

$$\epsilon(i,j) = \epsilon_h \quad \text{if} \quad \tau(i) = \tau(j) \qquad (5.3\text{-}5)$$

$$\epsilon(i,j) = \epsilon_h + \epsilon_{AB} \quad \text{if} \quad \tau(i) \neq \tau(j) \qquad (5.3\text{-}6)$$

where $\tau(i)$ is the type, A or B, of the i-th monomer. Such a Gaussian potential has been used in coarse-grained polymer simulations by Jendrejack et $al.$[59] and is similar to the cosine potential used by Kremer and Grest [60]. The standard deviation of the potential, $\sigma = 1.3\bar{\rho}^{-1/3}$. This value is a compromise between maintaining the spatial resolution of the model and suppressing high-frequency density fluctuations and correlations (Chapter 3).

The repulsion energy scale, ϵ, consists of a homogeneous term, ϵ_h, which is the same for all particle pairs, and an additional energy penalty, ϵ_{AB}, for pairs consisting of different types of particles. Strong homogeneous interactions maintain the low compressibility of the

system, while the heterogeneous penalty introduces the immiscibility of the two monomer types. For this system, we chose $\epsilon_h = 30$ and $\epsilon_{AB} = 3$.

We estimate that $\chi N \approx 24$ for this choice of ϵ_{AB}, where χ is the Flory-Huggins parameter, as discussed in Chapter 3 and Appendix 5.8.1. This corresponds to an intermediate segregation regime, where the system is sufficiently immiscible to self-assemble while maintaining interfaces that are relatively wide compared to the model resolution set by σ. The homogeneous repulsion is then chosen to be an order of magnitude larger to suppress the variation in total density near AB interfaces while maintaining relatively low absolute values of interparticle forces [20].

The unconfined lamellar period was found to be $L_0 \approx 4.7 R_g$, using the box length search algorithm of Schultz *et al.*[61]. Finally, note that the total interfacial energy in this system may be estimated as

$$U_{AB} = \sum_{i,j>i} u(r_{ij}) \frac{\epsilon_{AB}}{\epsilon(i,j)} \tag{5.3-7}$$

5.3.2 Boundary model

The cylindrical system was placed inside a square prism simulation cell. The width of the prism was $2\bar{\rho}^{-1/3}$ greater than the cylinder diameter, and the height was equal to $2L_0$. To simulate the matrix material, the space between the cylinder boundaries (in the radial direction) and the cell boundaries was filled with B_{10} homopolymer.

In order to keep the matrix chains outside the system, the position and momentum of any matrix particle that crossed into the system was exchanged with those of a nearby system particle that was farther from the axis than the trespassing matrix particle. Only particles within a radius $r_c = 1.2\bar{\rho}^{-1/3}$ of each other were used in such exchanges. This cutoff radius was found to be effective, but not systematically optimized. If no suitable system particle was detected within r_c, the coordinates of the matrix particle was left unchanged. Keeping the matrix particles out of the system was sufficient to keep the system particles out of the matrix and vice versa due to the low compressibility of the system. Periodic boundary conditions were used for all particles and interactions. To simplify implementation and to minimize the volume of the matrix necessary to contain the cylindrical system, the system particles crossing the cell boundaries were elastically reflected back into the cell. These events were rare and did not affect observed properties of the system. This fact was verified

both by directly counting such reflections and observing the effect of changing the matrix volume in several test systems.

The exchanges of coordinates described are not generally consistent with canonical ensemble sampling, leading to a rise in the temperature of the system and bath. This temperature increase was mitigated by rescaling the momenta of the particles within $r_c/2$ of the cylinder boundary after every time step. While this method of controlling the temperature could be much improved [43], it was deemed acceptable in this case because it was applied to a relatively small volume of the system. Moreover, in experimental systems, the structure of and interactions in the boundary monolayer are not usually characterized precisely.

This boundary condition implementation is designed to minimize the effect of the cylinder boundary on the total density of the system. Fixed wall boundary conditions, such as those obtained by elastic reflections or by freezing the matrix particles, result in a dramatic change in total density near the wall (data not shown). This is explained by the fact that the two-particle correlation functions are different near the wall and away from it. Swapping matrix and system particles rather than placing them at independently determined positions guarantees that each is found where a particle is to be expected in bulk. This minimizes the distortion in the pair density functions of the nearby particles due to the cylinder boundary. In homogeneous systems of monomers, this method conserves the radial distribution functions exactly, eliminating all boundary artifacts. Addition of bonds and, to a lesser extent, distinguishing particle types makes the system and matrix particles non-equivalent. Thus, swapping the particles leads to artifacts, requiring the additional thermostat.

5.3.3 Equilibration and sampling

Stochastic dynamics was used with a friction constant of one in simulation units for sampling and equilibration [60]. A time step of 0.1 was used in all simulations, with a Verlet integrator for the conservative forces. The initial conditions were generated by randomly placing all the chains into their respective domains (system or matrix). Simulations were allowed to continue until there were no visually detectable differences in the radial component density profiles, measured at least 1000 time units apart. Systems comprised of two concentric monolayers typically equilibrated in less than 1000 time units, while the larger ones required as long as 6000 time units. After equilibration, average composition fields and other system
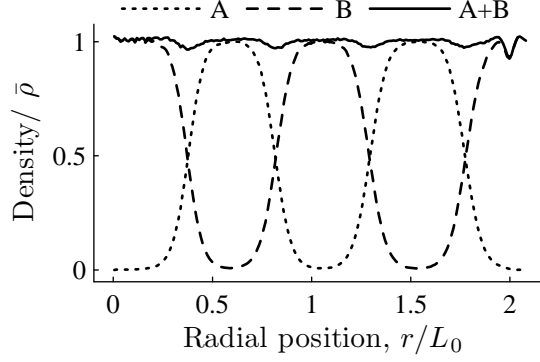
Figure 5-3: Typical radial density profiles, averaged over the azimuthal and axial dimensions. Here, the system contains four monolayers, $n = 4$, and has a radius $R = 2L_0$. Total density dips by no more than 3% at interfaces and by 7% near the cylinder boundary.

parameters were sampled over 1000 time units for all systems.

5.4 Results

5.4.1 Domain size and shape

As an initial validation of the simulation method, Fig. 5-3 shows a typical radial volume fraction profile of A and B components, as well as the total volume fraction relative to the bulk average density. The profiles are averaged in azimuthal and axial dimensions. The results confirm that the total density is reduced by no more than a few percent at A-B interfaces and by as much as 7% at the cylinder boundary. These errors are negligible for the current purposes since they are smaller than differences between block densities in many real polymers and the site occupancy variations commonly admitted in lattice chain simulations [70].

Further, domain widths vary periodically with cylinder diameter, as shown in Fig. 5-4. As the diameter of the system increases all domain sizes grow almost linearly up to a discontinuous transition, where a new concentric monolayer forms, incrementing n. The amplitude of the change in the domain size during this process is smaller for domains located farther from the axis. This is in agreement with the lattice chain systems [66, 70].

The mean domain widths were obtained by averaging the width of the i-th domain for cylinders of different diameter, for each i. They are generally less than the unconfined domain width, $L_0/2$, as indicated in Figure 5-5. Recall that the central domain width, Δr_1, corresponds to a half-width of a domain in the unconfined lamellar phase. Since the half of
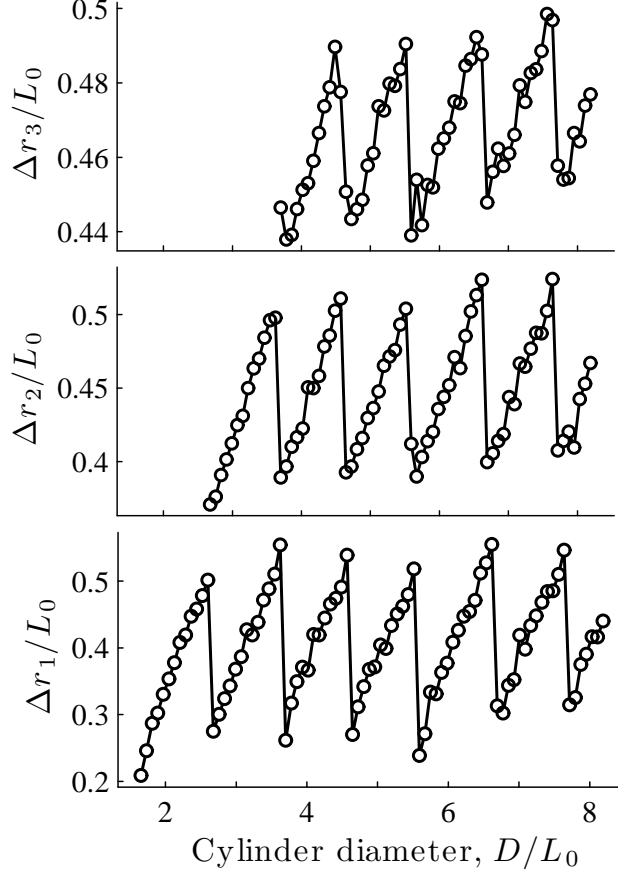
Figure 5-4: Periodic variation of the widths of inner three domains with system diameter. Note the differences in width scales among the figures.

a domain width in the unconfined case is $L_0/4$, the values of Δr_1 observed in simulations are comparatively high.

Next, we examined the critical cylinder diameters, D_n, at which the CL phases with $n-1$ concentric monolayers become unstable with respect to one with n concentric mono-layers. The value of D_n for each n was found by locating the two consecutive values of cylinder diameter D for which the equilibrium CL phases consisted of $n-1$ and n concentric monolayers. The value of D_n was then taken to be the average of these two diameters. Fitting the results to a linear function of n yielded

$$D_n^*/L_0 = 1.00n - 0.36 \qquad (5.4\text{-}1)$$

The standard error in the slope – or the period of the transitions – was found to be only
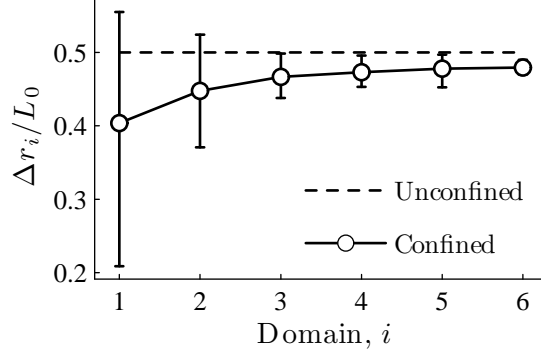
Figure 5-5: Averages (○) and ranges (vertical bars) of domain widths observed for all cylinder diameters, including samples with $n = 2$ to 7. Widths of domains in direct contact with the matrix were excluded. The solid line connecting the points is a guide to the eye.

0.01. Thus, despite the curvature, transitions between states with different n happen with a period in cylinder diameter very close to the unconfined lamellar spacing. The intercept suffers from a much larger standard error of 0.05. Note that the value of the intercept depends on the properties of the outermost domain, which is qualitatively different from the rest in that it directly interfaces with the matrix. As a consequence, the value of the intercept may be sensitive to the specific choices of the boundary conditions in models and the materials in real systems. Overall, Eq. 5.4-1 accurately describes the number of concentric monolayers in all simulations reported here.

The periodicity in critical diameter provides a convenient basis for a more detailed discussion of the changes in the morphology of the concentric monolayers with diameter. We define the surplus diameter, ΔD_n, as the increase in the system diameter over the minimum value required for the n concentric monolayers to be the equilibrium state,

$$\Delta D_n \equiv D - D_n^* \approx D - (n - 0.36)L_0 \tag{5.4-2}$$

The simulations with the surplus diameter between 0 and approximately $0.65L_0$ showed the expected axially symmetric shape. For larger ΔD_n, however, the axial symmetry was broken as the cross sectional profile of the inner domains increasingly flattened into a ribbon-like structure with increasing ΔD_n. This is illustrated in Fig. 5-6. This behavior was observed for all n, indicating that the symmetry breaking is a function of the the surplus diameter, not the total diameter. This symmetry breaking has not been previously reported. The flattened states are very stable, persisting several times longer than the time required to

$\Delta D_3/L_0$	Instantaneous	Time average
0.67		
0.83		
0.98		
1.06		

Figure 5-6: Simulated axial transmittance images of the transition from $n = 3$ to $n = 4$ monolayers as a function of cylinder diameter. Length of each system in axial dimension is $2L_0$. B block is assumed to have zero absorption. Interfaces positions are indicated by white lines, and the cylinder wall position by the black line. Time averages are from 1000 time unit simulations.

equilibrate a random initial state into the final structure. This is reflected in the high degree of consistency between instantaneous and time-averaged transmittance profiles shown in Fig. 5-6. This flattening appears to have the same dependence on surplus diameter in systems with $n = 2$ through $n = 7$.

To quantify the symmetry breaking more precisely, we introduce the acylindricity, A, of the AB interfaces as the order parameter. Uniformly spaced sets of points along each interface for each sample were obtained from time and axially averaged composition fields. The acylindricity of such a set of points $\{\mathbf{x}_i\}$ in the plane is defined in terms of its gyration matrix,

$$G_{\delta\gamma} = \frac{1}{m} \sum_{i,j=1}^{m} x_{i\delta} x_{j\gamma} \tag{5.4-3}$$

where $x_{i\delta}$ is the δ-th component of $\mathbf{x}_i$. The eigenvalues, λ_δ, of this matrix are the squares of the principal components and the eigenvectors are the principal axes of the point set. Thus, in two dimensions, the difference of the eigenvalues is a measure of how much longer the set of points is than it is wide. The acylindricity is defined as

$$A \equiv \frac{\lambda_1 - \lambda_2}{\lambda_1 + \lambda_2} \tag{5.4-4}$$

where $\lambda_1 \geq \lambda_2$. Thus, $A = 0$ only for a set of points uniformly distributed on a circle, and $A > 0$ otherwise.

Fig. 5-7 shows A for each of the three inner monolayers as a function of surplus diameter. Breaking of the axial symmetry is evident near $\Delta D_n / L_0 \approx 0.65$, as the A begins to rise. The constant value of A for $\Delta D_n < 0.65$ characterizes the fluctuations in the monolayer profiles. We expect these values to be attenuated with further time averaging of the composition profiles.

An important aspect of the acylindricity data revealed by Fig. 5-7 is that the values for different n coincide closely when plotted against the surplus diameter. This fact agrees with the results of visual inspection, indicating that the symmetry breaking and monolayer insertion transitions do not depend on the total number of concentric monolayers in the system.

Next, we examine the dimensions of the domains in more detail. Figure, 5-8a shows the dimensions of the first interface, which corresponds to the average radius of the central domain as well as the radii along the principal component axes. As is the case for
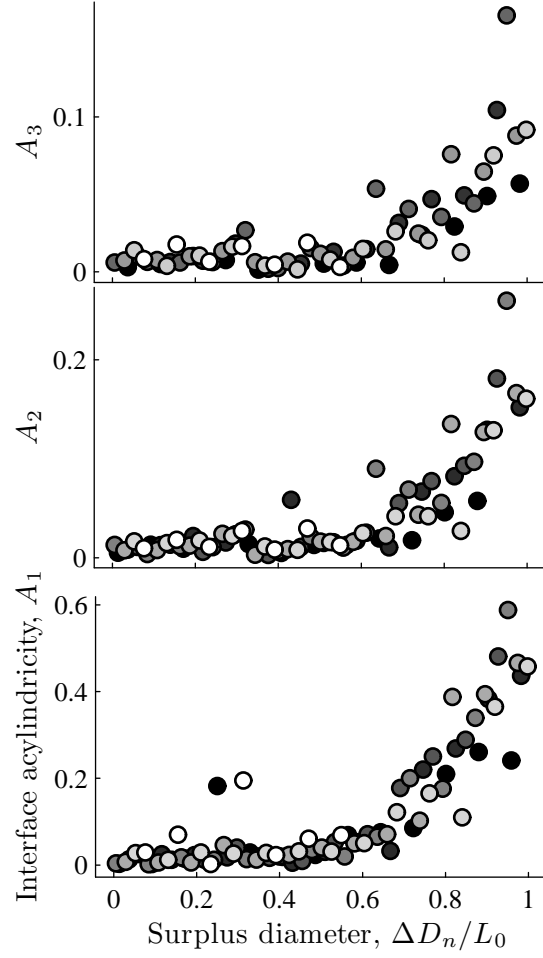
Figure 5-7: Acylindricity of the three innermost interfaces as a function of surplus diameter. Note the difference in scales among the plots. Symbols are shaded according to the number of monolayers in the sample, n, varying between black for $n = 2$ and white for $n = 8$. Symmetry breaking is apparent near $\Delta D_n \approx 0.65$
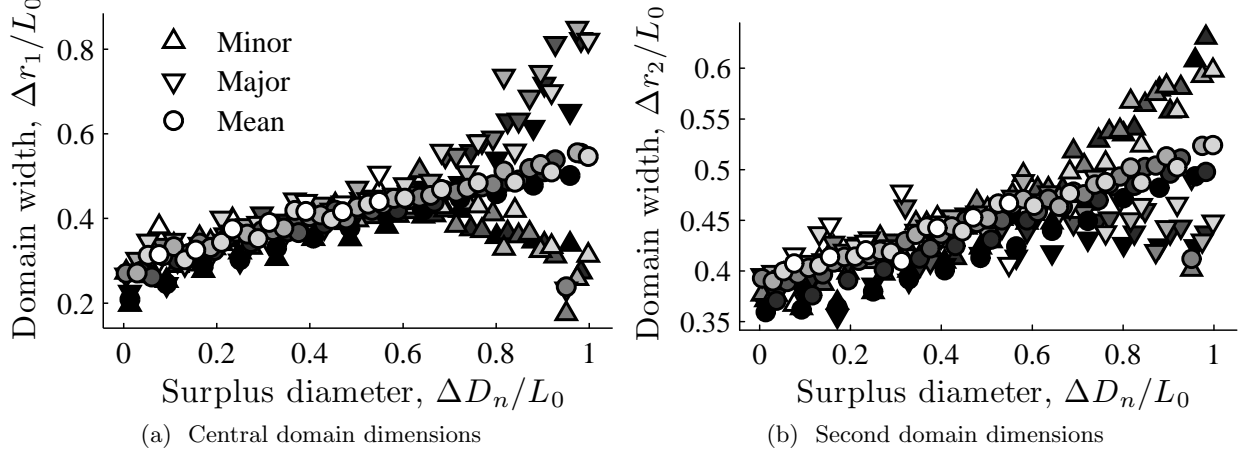
Figure 5-8: Width of the two central domains as functions surplus diameter, ΔD_n. Points are shaded according to total number of monolayers in the system, $n = 2$ to 8, with darker points corresponding to lower n. "Mean" is the average widths (area based); "Minor" and "Major" are domain widths measured along the two principal axes of the innermost AB interface, $r_1(\theta)$, for both plots. Note the difference trends of the widths along the minor and major axes between Δr_1 and Δr_2.

the acylindricity, the data for different n coincide very closely when plotted against ΔD_n, reflecting the periodicity of domain shape with cylinder diameter. The figure shows clearly that the central domain flattens after the symmetry breaking transition, with the narrow dimension of the domain reaching the unconfined domain width just before the critical diameter. At this point, the radius of the domain along the minor principal component axis, which corresponds to half the extent of the domain along the narrowest dimension, reaches a quarter of the unconfined period, $L_0/4$. The variation in width of the second domain, Δr_2, with D is shown in Fig. 5-8b. Here the width of the monolayer along the narrower dimensions increases with ΔD_n towards the unconfined value $L_0/2$. Unlike in the central domain, however, it is the thickness along the major principal component that is smaller. This is a result of a much greater degree of flattening of the central domain, compared to the second one. As in the case of Δr_1 and acylindricity, the Δr_2 for different n appear to fall on the same curve when plotted against ΔD_n.

The azimuthal average width of the third and other monolayers is also generally slightly below the unconfined value of $L_0/2$ (see Fig. 5-5). The variation in the domain widths along the principal axes for these outer domains is too small to distinguish from the noise in the data.

5.4.2 Chain conformation

We proceed to examine how changes in domain morphology affect the chain conformations. Specifically, we measure the radii of gyration, $R_{g\perp}$ and $R_{g\parallel}$, of the chains in the local coordinates introduced in Section 5.2 and illustrated in Fig. 5-2. Thus, $R_{g\perp}$, indicates the degree to which the chains are stretched normal to the AB interfaces, while $R_{g\parallel}$ indicates the degree of stretching in the direction tangent to the interface and normal to the cylinder axis.

Figures 5-9 and 5-10 show average $R_{g\perp}$ and $R_{g\parallel}$ for the chains in the inner two mono-layers as functions of surplus diameter, ΔD_n. The data is normalized by the corresponding values in unconfined copolymer simulations, $R_{g\perp}^* = 0.81\sqrt{a^2 N/6}$ and $R_{g\parallel}^* = 0.53\sqrt{a^2 N/6}$. As the surplus diameter increases, the chains stretch in the normal direction, along with increasing domain width, until the symmetry-breaking transition is reached. After the symmetry breaking occurs, the stretching slows and even reverses. This relaxation of the chains is consistent with the observation that the domain cross section narrows along one of its the principal axes while elongating along the other. The chains are also slightly compressed in the tangential direction. As the domains become increasingly flat past the symmetry-breaking transition, the chain dimensions in the tangential direction relax to the corresponding unconfined copolymer value. Thus, as the domain narrows and flattens, the local environment of a large fraction of the chains approaches that found in the unconfined case.

Fig. 5-11 and 5-12 present a broader view of the chain dimensions. First, Fig. 5-11 shows the relative dimensions of the chains in the three local directions for each monolayer, averaged over all cylinder diameters. This data indicates that the chains are compressed in the normal and tangential dimensions, but slightly expanded in the axial direction. Second, Fig. 5-12 shows the slopes of the best fit lines to the component radii of gyration as functions of ΔD_n in the axially symmetric regime ($\Delta D_n < 0.65$). Note that since $\Delta D_n \in (0,1)$ these slopes also reflect the amplitude of variation in the corresponding radii of gyration. The slope data indicates that the amplitude of chain stretching with cylinder diameter in the normal direction is largest for the monolayers closest to the axis, but this sensitivity quickly decays with increasing monolayer index. In the axial and tangential dimensions, statistically significant correlation between chain dimensions and the surplus diameter is detectable
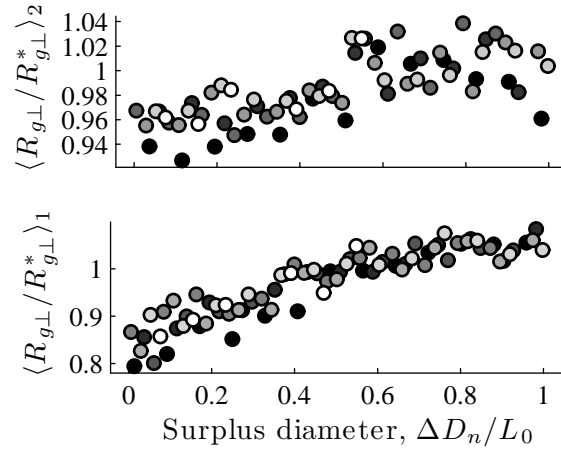
Figure 5-9: The normal component of the chain radius of gyration, $R_{g\perp}$, averaged over all the chain in each of the two inner two monolayers, as indicated by the subscripts of the y-axis labels. Data is normalized by the corresponding measurements in the unconfined lamellar case. The points are shaded according to the total number, n, of concentric monolayers in the sample, with lighter shade corresponding to larger n .
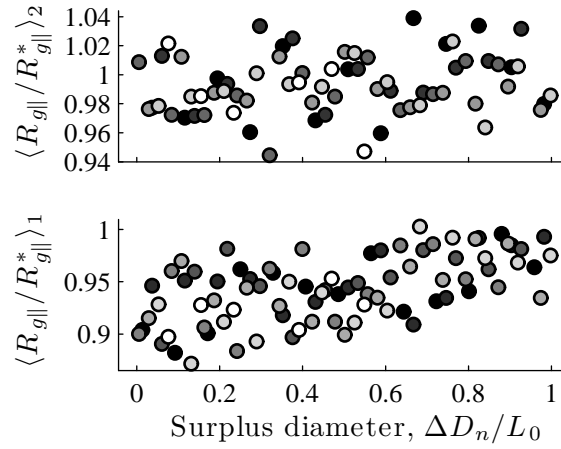
Figure 5-10: The tangential component of the chain radii of gyration, calculated analogously to the data in Fig. 5-9.
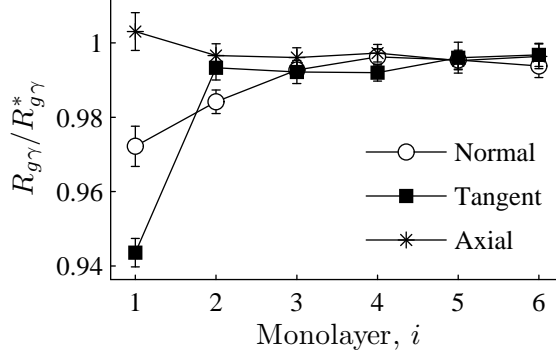
Figure 5-11: Radius of gyration components, $R_{g\gamma}$, along interface normals, tangents, and in the axial dimension for each monolayer averaged over all system diameters. Values are normalized by the corresponding quantities in unconfined case.
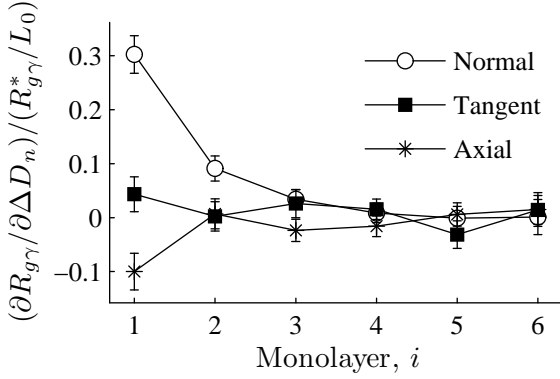
Figure 5-12: The slopes of the radius of gyration components, $R_{g\gamma}$, along interface normals, tangents, and in the axial dimension with surplus diameter for each monolayer. Only samples for $\Delta D_n \in (0, 0.65)$ were included.

only in the central monolayer. This data indicates that the chains expand slightly in the tangential direction, while contracting axially towards the unconfined case value as the surplus diameter grows.

5.4.3 Interfaces

Finally, Fig. 5-13 shows the excess interfacial energy, U_{AB}, per chain, normalized by its value in the unconfined lamellar phase, as a function of system diameter. Like the domain sizes and radii of gyration, the interfacial energy shows sharp discontinuities as the new monolayers are inserted. Unlike those quantities, however, the interfacial energy per chain decreases with the overall system diameter, commensurate with the decrease in the average curvature of the interfaces in the system. Between the transitions the interfacial energy
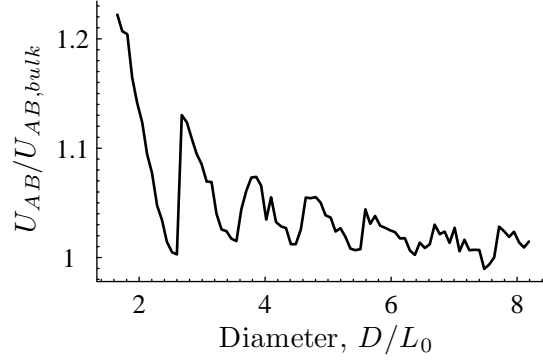
Figure 5-13: Excess energy of non-bond AB interactions per chain relative to the unconfined lamellar phase value, as a function of cylinder diameter.

decreases with diameter; as the chains stretch, the interfacial area per chain and the amount of contact between the two blocks decreases as well. Interestingly, the interfacial energy per chain is always greater than the value in the unconfined case, but approaches the unconfined value as the diameter approaches a critical value from below.

A deeper insight into the structure of the cylindrical domains is possible by examining the surface density of chains. Fig. 5-14 shows the number of chains that cross a cylindrical shell of radius r, concentric with the system axis, per unit area for two axially symmetric systems. Notice that the surface density of chains is lower for $\Delta D_n/L_0 = 0.1$ than for $\Delta D_n/L_0 = 0.65$. At the interfaces (marked by bullets in Fig. 5-14), the surface density decreases below the unconfined value with decreasing radius. This agrees with the observation that the interfacial energy in the CL phase is consistently higher than that of the unconfined lamellar phase. Also interesting is the observation that surface densities at all interfaces converge to the unconfined value near the onset of symmetry-breaking at $\Delta D_n \approx 0.65$.

In summary, the simulation results presented here reveal several properties of the CL systems that have not been described before. First is the fact that dependence of chain and domain dimensions is not only periodic with diameter, but to a large extent independent of the overall number of monolayers in the system. Second, we discover a symmetry breaking transition before the discontinuous transition corresponding to insertion of a new concentric monolayer. This symmetry breaking transforms the central domains of the CL phase into a locally flat lamellar morphology, resembling the lamellar phase observed in the unconfined case, for surplus diameters, $\Delta D_n/L_0$ above approximately 0.6-0.7. Third, we also find that the chains are generally compressed in the normal and tangential directions, with the degree

118
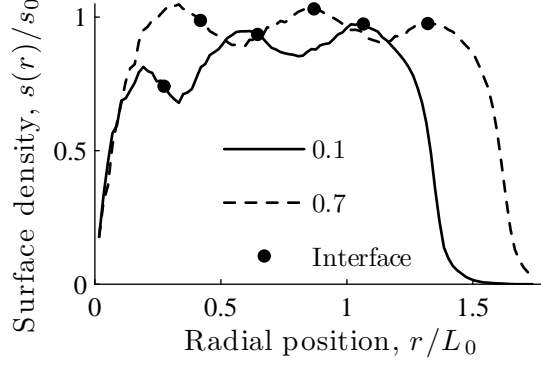
Figure 5-14: Radial dependence of surface density for a three monolayer system, $n = 3$, just above a critical value of the diameter, $\Delta D_n/L_0 = 0.1$ and near the symmetry breaking transition $\Delta D_n/L_0 = 0.65$. Points indicate indicate domain interfaces; s_0 is the interfacial surface density for this system in the unconfined lamellar phase. Chain density drops off near the cylinder wall, as expected.

of compression increasing with curvature of the interfaces. Finally, we find that the average interfacial energy is greater than the value in the unconfined case, while the interfacial chain densities are less than the unconfined value.

5.5   Narrow interphase theory

As mentioned earlier, in the CL case the SST approach fails to predict the discontinuous nature of the transitions between states with different numbers of concentric domains. SST also fails to predict the decrease in the amplitude of variation of domain widths for domains farther away from the axis. The key assumption of the strong stretching theory is that the chains are stretched to the point where chain contour fluctuations are negligible and monolayers comprised of diblock chains are nearly impenetrable to each other.

Evidence indicates that this is not the case in neat block copolymers. It has been shown both theoretically and experimentally that the scaling exponent of the lamellar period in block copolymers with molecular weight is roughly between 0.6 and 0.8 [42]. This is qualitatively different from the linear scaling required by SST, indicating considerable fluctuations in chain contours and interpenetration between monolayers of diblocks. SST is also inconsistent with the very large amplitude of change in domain sizes and chain radii of gyration observed in the simulations reported here.

Therefore, we develop a theory of the CL phase based on a less restrictive narrow interphase approximation, NIA. This approximation merely requires that the interfaces between

the blocks are narrow relative to the width of the domains and the domains themselves are pure. Unlike SST, NIA allows large fluctuations in chain contours. NIA is the basis for the most widely-used and accurate high-level free energy model of unconfined diblock systems, particularly for understanding the scaling behavior of domain sizes [40, 42]. Note that the assumption of sharp interfaces between blocks generally implies that the blocks are confined to their respective domains. Therefore, to avoid confusion in definitions, we emphasize that the terms "monolayer interpenetration" used in the context of SST will generally refer to overlap between monolayers of diblocks, rather than such crossing of the domain interface by blocks within the same monolayer.

As usual [18], we describe the behavior of the block copolymers in terms of the interplay of the interfacial energy, U_{AB}, which drives segregation and reduces contact between the blocks at the expense of stretching them, and loss of conformational entropy, S_s, associated with this stretching. In addition, an extra term, F_c, is introduced to account for the curvature of interfaces. Thus, the free energy of a CL system per unit length of the cylinder is

$$F = U_{AB} - S_s + F_c \qquad (5.5\text{-}1)$$

As usual, we assume that the melt is incompressible and the total monomer density is everywhere equal to its bulk value [18, 72]. Further, we assume that all the monolayers are concentric and axially symmetric. The assumption of axial symmetry limits the validity of the theory to $\Delta D_n < 0.65$.

Thus, we focus mainly on accounting qualitatively for the following observations from the simulations: the domains and chains are generally compressed compared to the unconfined case; the interfacial energy is increased compared to unconfined case; and the inner monolayers are much more sensitive to the system diameter than the outer ones.

5.5.1   Interfacial energy

The interfacial energy, U_{AB}, corresponds to the extent to which A and B blocks interact with each other. Correspondingly, the interfacial energy per chain should increase with decreasing interfacial surface density of chains, s_i. Therefore, we assume the following

linear model for the interfacial energy per chain:

$$f_i = -\alpha \frac{s_i - s_0}{s_0} \tag{5.5-2}$$

Here s_i and s_0 are interfacial chain surface densities in the i-th interface and in the un-confined lamellar phase, respectively, α is a positive constant with units of energy, and the unconfined lamellar phase is taken as the reference state. We expect α to be comparable to the interfacial energy per chain in the unconfined case, which was determined to be $2.02 k_B T$ for the system used here. Note that f_i is positive whenever the surface density is lower, or the surface area per chain is larger, than that in the unconfined case. This is consistent with the observed decrease in U_{AB} with increasing cylinder size (Fig. 5-13), since interfacial density increases with increasing domain width.

The surface density is directly related to domain widths through the incompressibility assumption. Specifically, we can equate the number of chains contained in a domain written in terms of the domain volume and chain density to that in terms of the surface chain density and the area of interfaces of the domain

$$(2\bar{\rho}/N)\pi(r_i^2 - r_{i-1}^2) = 2\pi(s_i r_i + s_{i-1} r_{i-1}) \tag{5.5-3}$$

where we use the fact that the block density is twice the chain density, $\bar{\rho}/N$. In the limit $i \to \infty$, the surface densities tend to their value for flat lamellae, $s_i \to s_0$, and Eq. 5.5-3 may be solved for the surface density in the unconfined lamellar phase, $s_0 = \bar{\rho}/N(L_0/2)$. For finite i the equation may be solved approximately

$$s_i \approx s_0 \frac{2\Delta r_i}{L_0} \tag{5.5-4}$$

The estimate is exact for CL systems with $i = 1$ and $i \to \infty$; more precise relationships may be derived but are not essential at this point.

We may now calculate the excess interfacial energy of a CL system in terms of domain

widths by summing the contributions from all monolayers

$$\frac{U_{AB}}{2\pi h k_B T} \approx \sum_{i=1}^{n} s_i r_i f_i \qquad (5.5\text{-}5)$$

$$\approx -\sum_{i=1}^{n} s_0 \frac{2\Delta r_i}{L_0} r_i \alpha \left(\frac{2\Delta r_i}{L_0} - 1 \right) \qquad (5.5\text{-}6)$$

$$\approx -\frac{4\alpha s_0}{L_0^2} \sum_{i=1}^{n} r_i \Delta r_i (\Delta r_i - L_0/2) \qquad (5.5\text{-}7)$$

where h is the length of the system along the axis. This implies that decreasing the domain widths below $L_0/2$ leads to an increase in interfacial energy compared to the unconfined case. This is consistent with the observations that the interfacial energies in the CL simulations are larger than in the unconfined case and that they decrease with increasing domain width. More importantly, the amplitude of the energy penalty increases with radius (roughly as r_i^2 for $i \approx 1$ and linearly for $i \gg 1$). This accounts for the drop in the sensitivity of domain widths to the cylinder radius as a function of domain index.

This result is also in contrast with the implications of the constant interfacial energy per interfacial area, σ_{AB}, used by Wang [70]. In that case, the interfacial energy of the i-th monolayer is $2\pi r_i h \sigma_{AB}$. The energy penalty for perturbing r_i by a fixed amount is independent of i. Consequently, under Wang's assumptions, there is no benefit in distributing a small surplus diameter among different monolayers non-uniformly.

5.5.2 Tangential compression due to curvature

The reason why the cylindrical confinement tends to decrease domain widths, at the expense of increased interfacial energy, remains to be discussed. Here, we offer an explanation based on the loss of chain conformational entropy due to curvature, reflected in the compression of the average chain dimensions in the azimuthal direction.

Under NIA, each block behaves as an ideal chain attached to a solid wall by one end. Curving this wall expands the volume available to a block on the convex side, but also reduces the volume accessible to the block on the concave side. To quantify this effect, consider the number of conformations accessible to a block whose center of mass lies within a restricted range of azimuthal angles on the concave side of the interface. If the number is approximately independent of the azimuth, the total number of conformations accessible to
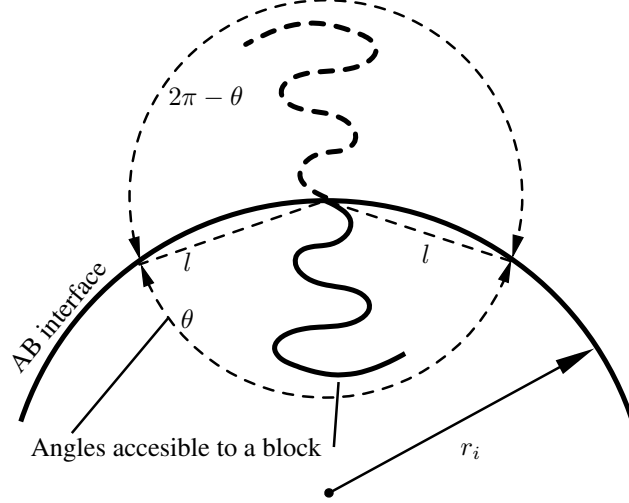
Figure 5-15: Curvature of the interface restricts the range of angles accessible to the block on the concave side and expands it for the block on the convex side. Overall, entropy is lost. The range of accessible angles is estimated using points of intersection between the interface and a shell of radius comparable to characteristic chain dimension l.

the block is proportional to the range of angles its center of mass may explore, illustrated in Fig. 5-15. In reality, chains with centers of mass closer to the wall have fewer conformations than those farther away. Also, the conformational entropy depends on how far the chain is stretched and other factors. We neglect these effects as a first approximation.

Now, the range of azimuthal angles accessible to a block may be used as a measure of the number of conformations accessible to that block and therefore, its conformational entropy. If θ is the range of azimuthal angles accessible to the block on the concave side, the corresponding range of angles accessible to the block on the convex side is $2\pi - \theta$. Since under NIA, the two blocks are effectively independent chains anchored at the same point, the number of conformations of the chain as a whole should scale as the product of the two angles, $\theta(2\pi - \theta)$. The logarithm of this product, therefore, is the corresponding conformational entropy:

$$S_{c,i}(\theta) = \ln[\theta(2\pi - \theta)] - \ln(\pi^2) \tag{5.5-8}$$

where the flat interface case, $\theta = (2\pi - \theta) = \pi$ is used as the reference state.

To estimate θ, we introduce a characteristic distance, l, from the block junction to the block center of mass. A reasonable value of θ may now be obtained from the intersection points between a circle of radius l, and the AB interface of radius r_i, as illustrated in Fig. 5-15, yielding $\theta = 2\arccos[l/(2r_i)]$. Linearising this expression in terms of curvature, $1/r_i$,

yields

$$S_{c,i} \approx -\left(\frac{l}{\pi r_i}\right)^2 + O\!\left(1/r_i^4\right) \qquad (5.5\text{-}9)$$

Finally, we estimate l in terms of the domain width as $l = k\Delta r_i$, where k is a dimensionless constant $O(1)$. This assumption is justified by the observation that in the simulations reported here both the domain sizes and normal radii of gyration of the blocks are approximately linear with ΔD_n for axisymmetric systems. This leads to

$$S_{c,i} \approx -\left(k\frac{\Delta r_i}{\pi r_i}\right)^2 \qquad (5.5\text{-}10)$$

Thus, the net effect of curvature is a loss of conformational entropy. This explains the relatively small tangential $R_{g\parallel}$ in high curvature monolayers, observed in simulations. As in SST, here the free energy associated with curvature is quadratic in curvature [70, 73]; however, in contrast to SST, the numerator of $S_{c,i}$ scales with the second, rather than fourth, power of the domain widths [70]. This weaker dependence reflects the higher degree of chain contour fluctuations and of monolayer interpenetration – both of which are related mechanisms for relaxing curvature-induced stresses – under NIA than under SST.

The total free energy increase in an axisymmetric CL system due to the conformational entropy loss resulting from interfacial curvature is

$$\frac{F_c}{2\pi h k_B T} = -\sum_{i=1}^{n} r_i s_i S_{c,i} \qquad (5.5\text{-}11)$$

$$\approx \sum_{i=1}^{n} r_i s_0 \frac{2\Delta r_i}{L_0} \frac{k^2 \Delta r_i^2}{\pi^2 r_i^2} \qquad (5.5\text{-}12)$$

$$= \frac{2k^2 s_0}{\pi^2 L_0} \sum_{i=1}^{n} \frac{\Delta r_i^3}{r_i} \qquad (5.5\text{-}13)$$

As expected, the bending free energy penalty decreases with decreasing average curvature in the system. More importantly, the bending free energy is reduced by decreasing domain widths, Δr_i. Thus, minimizing conformational entropy loss due to bending provides the driving force behind the observed reduction in domain widths compared to the unconfined lamellar phase surface density value, $\Delta r_i = L_0/2$. Evidently, the reduction in this entropy loss compensates for the increase in the interfacial energy associated with decreasing domain widths.

Note also that the dependence of curvature free energy on domain width is strongest for small r_i, contributing to the higher sensitivity of inner monolayers to the cylinder diameter. This effect should be even stronger in the SST. The fact that no such difference is observed in SST may be attributed to the much higher cost for monolayer interpenetration.

5.5.3 Normal chain stretching

Chain stretching normal to the interfaces and the corresponding loss of conformational entropy is due to the need to maintain constant total monomer density across the domains [18]. Evaluation of this conformational entropy loss is the central problem of coarse-grained polymer models. In unconfined phases, the extent of chain stretching may be parametrized in terms of a single characteristic length scale of the structure, such as the unit cell dimension in periodic phases of block copolymers or interface width in binary mixtures. Such a relationship has been obtained by Helfand and Wasserman for the unconfined lamellar case under the NIA, suggesting that the stretching contribution to free energy scales roughly as a power of 2.5 with lamellar spacing [40] (also see [39, 41] for spherical and cylindrical phases in bulk). Note that SST requires quadratic scaling of free energy with domain sizes, based on flat film calculations [70]. This highlights the the difference in assumptions about the chain stretching under SST and NIA. The difficulty of applying Henlfand's result to the CL phase is that no unique definition of the lamellar period exists in this case.

Fortunately, there is a reason to believe that the extent of normal chain stretching is mainly determined by the widths of the domains in which the chain is found and is not significantly affected by the curvature of the domains. Consider the effect of curvature in the i-th interface on a block on the convex side of the $(i-1)$-th interface. For the curvature of the i-th interface to alter the conformational statistics of the block originating at the $(i-1)$-th interface, a significant portion the block must be found near the i-th interface. Direct observations in this series of simulations (data not reported) suggest that the domains are sufficiently wide that this is rare and cannot change the overall conformational statistics much. Notice that here this is achieved at a moderate value of $\chi N \approx 24$ and is likely to hold, at least as a first approximation, for more miscible blocks, since the domain sizes in the lamellar phase are generally greater than twice the ideal radius of gyration of a single block [3].

If the chain stretching normal to the interface is indeed independent of the interfacial

curvature, the component of the radius of gyration normal to the interface for the chains forming the i-th monolayer, $\langle R_{g,\perp}\rangle_i$, may be accurately described by some local measure of interface width, without regard to the interface curvature. Since the two blocks of each chain in the i-th interface are found in both i-th and $(i+1)$-th domain, we define the relevant width metric as

$$w_i = \begin{cases} r_1 + \Delta r_2/2 & \text{if } i = 1 \\ (\Delta r_i + \Delta r_{i+1})/2 & \text{if } i > 1 \end{cases} \tag{5.5-14}$$

Notice that for axisymmetric systems ($\Delta D_n < 0.65$) both the domain widths and the average normal component of the gyration tensor for the chains in a given monolayer, $\langle R_{g\perp}\rangle$, are approximately linear with cylinder diameter. This is evident by comparing Figures 5-8 and 5-9. Therefore, we expect that for axisymmetric systems, $\langle R_{g\perp}\rangle_i$ for the i-th monolayer is linear with w_i. A comparison of these slopes for high curvature monolayers close to the axis with those further away and, therefore, with lower curvature, should indicate the degree to which interfacial curvature influences normal chain stretching.

Such a linear relationship would also allow the the free energy due to normal stretching per chain in the i-th monolayer, $f_{s,i}$ to be estimated in terms of the domain widths. In general, increasing w_i should stretch the chains and increase $f_{s,i}$. Characterizing the form of $f_{s,i}$ is beyond the scope of this article, but one reasonable expression is

$$f_{s,i} = \zeta \frac{\langle R_{g\perp}\rangle_i}{R_{g\perp}^*} = \zeta \frac{\partial\langle R_{g\perp}\rangle_i}{\partial w_i} w_i \tag{5.5-15}$$

where ζ is a positive constant with units of energy. This yields the following expression for the conformational entropy associated with normal chain stretching for a whole CL system

$$\frac{S_s}{2\pi h k_B T} = -\sum_{i=1}^{n} r_i s_i f_{s,i} \tag{5.5-16}$$

$$\approx -\frac{2\zeta s_0}{L_0} \sum_{i=1}^{n} \frac{\partial\langle R_{g\perp}\rangle_i}{\partial w_i} \Delta r_i \tag{5.5-17}$$

We obtained the slopes $\partial\langle R_{g\perp}\rangle_i/\partial w_i$ by linear regression of the simulation data. The results are presented in Table 5.1. The observation that $\partial\langle R_{g\perp}\rangle_i/\partial w_i$ shows no statistically significant variation with i is consistent with our hypothesis that chains stretching normal to the interface is independent of the interfacial curvature. Note that the confidence intervals

126

for the estimates are rather wide due to the fact that the range of variation of both $\langle R_{g,\perp} \rangle$ and domain widths themselves rapidly decrease for increasing i.

Monolayer, i	$\partial \langle R_{g,\perp} \rangle_i / \partial w_i$
1	0.68 ± 0.06
2	0.7 ± 0.1
3	0.8 ± 0.3
4	0.8 ± 0.4

Table 5.1: Slope $\langle R_{g,\perp} \rangle_i$ with domain size, w_i (Eq.5.5-14) with standard errors obtain from linear regression. Only axisymmetric samples ($\Delta D_n < 0.65$) were considered.

The situation is more complex in the non-axisymmetric region characterized by $\Delta D_n / L_0 > 0.65$. Figures 5-8 and 5-9 show that while the average domain sizes continue growing with system diameter, $R_{g\perp}$ does not. Thus, a single scalar metric is no longer enough to describe the local environment of the chains. Note that the average $R_{g\perp}$ for acylindric monolayers is not only determined by the local domain width but also possibly by how the chains are distributed among the high- and low-curvature parts of the interface. The precise nature of this dependence is difficult to infer from the available data. Therefore, we do not attempt to construct a quantitative high-level description of normal chain stretching for the non-axisymmetric cases.

5.5.4 Symmetry breaking

This non-linear dependence of normal chain dimensions with cylinder diameter suggests a qualitative explanation for the stability of the non-axisymmetric CL morphologies. Evidently, the flattening of inner monolayers is a way for domain dimensions to increase with fiber diameter without stretching the chains. Notice that the effect of symmetry breaking on the dependence of the interfacial energy and tangential chain dimensions on the cylinder diameter are not readily apparent in the simulation data in Fig. 5-13 and 5-10. This observation indicates that reduction in normal chain stretching is the primary reason for the symmetry breaking.

Unfortunately, a rigorous analysis of stability of the axisymmetric morphology in the CL phase is not possible based on the NIA energy model proposed here since we assumed axial symmetry at the outset. The key difficulty in extending the NIA to angle-dependent interfacial radii is in describing how the interfacial chain density varies with local interface

curvature. The interfacial chain density is determined by a combination of interfacial energy and entropic effects that must be evaluated self-consistently. Establishing the reliability of parametrization of any particular expression for the free energy per chain described above may also turn out to be non-trivial, particularly for non-axisymmetric interfaces. These are challenges for further work.

5.6 Discussion

In this work, we have relaxed the strong stretching approximation to analyze effects of interface curvature. Although SST is the main analytical approach to treating curvature effects in block copolymers (see, for example, references [70, 74, 75]), the NIA appears to be more accurate. As mentioned above, the most compelling evidence for the claim that significant chain contour fluctuations are typical of neat block copolymer systems is the well-known observation that the scaling exponent of domain sizes with molecular weight is significantly smaller than one. The failure of SST and success of the NIA treatment presented here in explaining the properties of the CL phase provide further evidence of the fact.

The NIA free energy model developed here for axisymmetric CL systems highlights the degree to which cylindrical confinement complicates analytical approaches to describing phase equilibria. In the unconfined lamellar and flat film systems, translational symmetry makes it possible to describe the domain dimensions in terms of a single scalar domain width. In contrast, cylindrical confinement makes each domain unique, introducing many more degrees of freedom. These include not only domain widths, but also additional variables required to specify the deviation of domain interfaces from cylindrical morphology. These complications introduce significant uncertainty in the NIA free energy model presented in this report, making it better suited for broad qualitative description of the key physical phenomena in the CL system rather than detailed, quantitative studies. Such quantative studies of the universal features of block copolymers in confinement may be conveniently performed using direct simulation of simplied bead-spring block copolymers, as we have done in the first half of this paper.

Perhaps the most significant departure of the results presented here from other computational studies is the breaking of the axial symmetry in CL phases. Previous reports of symmetric diblocks under cylindrical confinement, including lattice chain simulations and

self-consistent mean field theory calculations, have shown only axially symmetric phases. Several factors lend credibility to our result. First is the fact that the transition appears to be insensitive to the total number of concentric monolayers, happening much the same way in systems with two concentric monolayers as those with six. This excludes any unphysical artifacts of the boundary method employed here. Secondly, flattening of the central monolayers is observed in experiments, as exemplified by Fig. 5-1. We suggest that this symmetry breaking and flattening is favored thermodynamically since it reduces the degree of chain stretching with increasing cylinder diameter.

There are a number of features of this study that may explain why symmetry breaking was observed here, but not in previous studies. First is that our study uses a higher resolution in system diameters than others. Second is the more realistic treatment of thermal fluctuations due to a relatively high chain density. Lattice studies use much lower chain densities, allowing for unrealistically high fluctuations. Large fluctuations may alter the free energy balance or simply make the symmetry breaking less obvious. Since there is no preferred direction to the elongation, the major axis of elongation may also rotate rapidly with respect to the simulation cell in a highly fluid system. Mean-field calculations exhibit the opposite problem, neglecting fluctuations entirely. Unfortunately, we are not aware of any mean field calculations with sufficient resolution in cylinder diameter to draw any definitive conclusions about the symmetry breaking under such assumptions.

Procedurally, another novel aspect of this study is the relatively soft boundary model. While perfectly impenetrable walls are possible to implement in lattice and field-theoretic systems, they are impractical in continuous space particle models. In real systems, the walls of the confining matrix are generally imperfect and, depending on the material, may even allow some mixing of the matrix material with the system. This introduces some uncertainty in the cylinder diameter. Thus, the softer boundary used here may, in fact, be more physically realistic than smooth impenetrable walls. The softer boundary may also give systems with few monolayers slightly more freedom to deform than they would if the walls had been perfectly cylindrical.

An intriguing possibility is raised by the apparently universal behavior of domain sizes, chain dimensions, and acylindricity for systems of different diameters. Simulations suggest that the properties of inner monolayers is indeed largely independent of the total number of concentric monolayers n. This would imply that CL structures with at least eight concentric

monolayers may be manufactured reliably. The stability of CL structure of large diameter is important for practical reasons since the large number of monolayers have the advantage of both insulating the relatively unstable central monolayers from wall imperfections as well as simplifying preparation of the confining cylinder itself. Thus, an extension of this work to larger cylinder diameters as well as a characterization of the stability of the CL phase with respect to wall imperfections are in order.

5.7 Conclusions

The above results may be organized around the three key features of the CL phase discussed here. First, the fact that domains closer to the axis are much more sensitive to the overall cylinder size than those closer to the cylinder boundary is associated with interfacial energy effects. This analysis highlights the importance of the dependence of interfacial chain density and energy density on domain width and radius, often neglected in similar analyses. Second, we find that the domains and chain dimensions are on average thinner in the CL phase than in the lamellar phase under no confinement or under flat film confinement. This reduction is driven by the additional chain conformational entropy loss due to the interfacial curvature. Finally, the periodic second order symmetry-breaking transitions where the central monolayers flatten into a ribbon-like morphology at large surplus diameter is a way to reduce conformational entropy loss due to chain stretching normal to the interfaces. These features appear to be largely universal for CL phases between two and eight monolayers, to within the precision of the simulations reported here. We hope that these findings, along with the simulation methodology used here, will solidify the foundation for further analysis of the rich variety of block copolymer morphologies in confinement.

5.8 Appendix

5.8.1 Estimate of χN

We estimate χN as follows. First, U_{AB} is measured in simulations at $\epsilon_{AB}N = 0.001$ and 0.01. We have previously estimated Chapter 3 that in the absence of long range composition

fluctuations

$$U_{AB} = \epsilon_{AB} N n f_A f_B \xi \tag{5.8-1}$$

$$\xi = \int (u_{AB}(\mathbf{r})/\epsilon_{AB}) g_{AB}(\mathbf{r})\, d\mathbf{r} \tag{5.8-2}$$

where $f_k = \bar{\rho}_k/\bar{\rho}$. Also, from the usual statement of the Gaussian chain model we have

$$U_{AB} = \chi N f_A f_B n \tag{5.8-3}$$

From the simulations, we calculate $\xi = 0.8529 \pm 0.0002$ and 0.8527 ± 0.0002 for $\epsilon_{AB} N = 0.001$ and 0.01 respectively. The error estimates are 90% confidence intervals assuming Gaussian noise (t-test). Histograms of the measured energies are visually consistent with this distribution. Therefore, we estimate $\xi = 0.853$.

Note that for higher values of χN this is likely to be an upper bound, exceeding the actual χ by about 5%. This finally leads to an estimate of χ:

$$\chi N = 0.95 \xi \epsilon_{AB} N = 0.81 \epsilon_{AB} \tag{5.8-4}$$

Finally, the value of the unconfined lamellar period, $L_0 = 4.7 R_g$, measured in simulations may be used to check our estimate of χN. Mean field calculations of Matsen and Bates predict a comparable bilayer width at $\chi N \approx 30$ [2]. Extrapolation of the calculations of Barrat and Fredrickson, who corrected the mean field treatment for thermal fluctuations, indicates that $L_0 = 4.7 R_g$ when $\chi N \approx 19$. Thus, our estimate of $\chi N \approx 24$ falls between these literature results.

5.8.2   Tracing interfaces

The curves describing the AB interfaces in the simulation systems were determined as follows. We start with a set of monomer positions of an equilibrated system, which is used to obtain the axial average volume fraction fields of A and B components in the polar coordinates, (r, θ). Using a grid of 20 points in θ, we calculated the radial positions, r, corresponding to the interfaces, where densities $\rho_A(r, \theta)$ and $\rho_B(r, \theta)$ were equal. To reduce the artifacts of noise, the fields were smoothed with a Gaussian filter with the width comparable to that of the interaction potentials. This produces a set of points, equally

spaced in azimuth, along the countour of the A-B interface of each monolayer. In the overwhelming majority of cases, this procedure yielded a unique interfacial radius for each monolayer. Fig. 5-16 shows a sample result of this procedure.
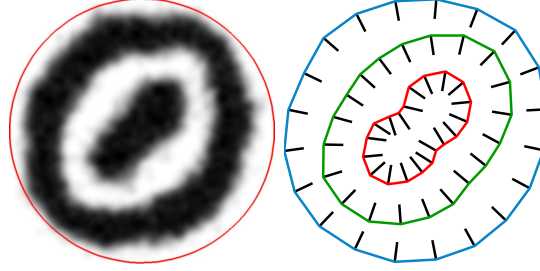

Figure 5-16: Results of interface tracing for a sample with $\Delta D_n = 0.98$, showing estimated interface normals.

6

Conclusions

In summary, the dissertation provides significant contributions towards all three objectives of this work. First, a general framework for interpreting CGPP models as approximations for GCM (rather than mean-field GCM). Specific characteristics of good approximations have been identified as well-defined dimensionless chain density, long-ranged potentials, and harmonic spring bonds significantly longer than characteristic interparticle distance. Second, a specific models meeting these criteria was constructed and validated against existing perturbation theories and experimental data on molecular weight dependence of critical Flory-Huggins parameter values and peak scattering wavelengths in symmetric diblock copolymer. And finally, the model was fruitfully applied to reveal the details of physical phenomena responsible for the peculiar features of concentic lamellar phases arising in block copolymes confined in cylinders. These results establish the model reported here as well as the general approach to constructing particle based models as a convenient and reliable computational technique that useful for calculating fluctuation-related properties of fluid block copolymers and polymer blends of experimentally relevant molecular weights. Thus, explicit simulations of coarse-grained bead-spring polymers become an attractive complimentary method to field theorietic simulations in equilibrium cases. Moreover, this work sets the stage for the development of rigorous non-equilibrium simulations of these systems.

The main idea that emerges from the results above is that if the interaction poten-

tials between particles are sufficiently broad, it becomes possible to define some effective instantaneous thermodynamic state associated with each particle. The existence of such a well-defined instantaneous thermodynamic state is the central assumption of GCM and is what makes it possible to define a composition independent χ parameter with a given model. This conclusion parallels the physical justification of the GCM (Section 2.2.2): the GCM chains are considered to be so long that any finite section of it is also sufficiently long to interact with a very large number of other chains.

For finite molecules, however, there is a trade-off between resolution of molecule scale detail and abstraction from monomer scale detail. Increasing the range of potentials decreases the uncertainty in instantaneous values of thermodynamic state variables associated with a particle but at the price of smoothing out long-range correlations. Evidently, as the dimensionless chain density increases, so does the monomer density at a fixed number of monomers per chain.

These considerations highlight two problems with existing approaches to constructing explicit chain simulation models. First, these models are constructed with intentionally short-ranged potentials, presumably to speed up computation. And second, they are performed at very low chain densities. Consequently, not only are the local fluctuations inflated but they cannot be suppressed significantly without also introducing artifacts into the long-range features.

Fortunately, the results of Chapter 4 indicate that an effective balance may be struck between the uncertainty in local and long-range effects when 10–20 particles are used per molecule even at the lower end of the experimentally relevant chain densities. Thus, we construct an effective bead-spring model that is equivalent to GCM to within some systematic composition-dependent error of several percent in the Flory-Huggins miscibility parameter and chain density. This model provides an effective method for studying phase behavior of block copolymers without excluding fluctuation effects.

Thus, the main goal of this dissertation – construction of a rigorously parametrized explicit chain simulation methodology for complex fluids – has been achieved.

134

7

Future work

7.1 Improvements in methodology

Without a way to compare the accuracy of different simulation methods on the same basis, the question of the computational advantages of different simulation methods was moot. Our results enable a more balanced comparison of various simulation methodologies and interaction models in terms of their efficiency. Subsequent studies should focus on optimizing the interaction range and resolution of continuous space models along with comparisons between Monte Carlo and continuous space approaches.

It is also critical to validate our results using independent means. While agreement with experimental data reported here is a first step, the most direct way of doing this is through comparison between field theoretic simulations and bead-spring calculations of the same system. It appears that such comparison may be practical in the range of dimensionless chain densities C between $10 - 100$, where both particle and FTPS calculations are feasible, although difficult. Of particular interest is the degree to which cutoff wavelength, or grid resolution, in FTPS corresponds to the range of the potentials in particle simulations.

7.2 Applications to complex fluids

While significant improvements may be possible to the simulation methodology presented here, it appears to be sufficient to be fruitfully applied to systems more interesting than symmetric diblock copolymers. An examination of the fluctuation effects on the less stable, spherical phases of block copolymers would be particularly interesting. Also, a detailed comparison of scattering functions observed in simulations and experiments is in order since these are our main source of quantitative information about the morphology of complex fluids.

Perhaps the most exciting application of the model lies in non-equilibrium studies. Both periodic and steady shear may be applied to the bead-spring model through the Lees-Edwards algorithm [44, 63]. It is reasonable to expect that the long time-scale viscoelastic behavior due to ordering in block copolymers may be captured by the model presented here. Preliminary studies (data not shown) have demonstrated that the model follows Rouse relaxation dynamics. Therefore, incorporation of explicit uncrossability constraints or other means of modeling entanglements should better represent shorter time viscoelastic behavior.

7.3 Application in other fields

An interplay between field and particle formulations very similar to that between the bead-spring and GCM has a rich history in other fields, notably in quantum mechanics and, more recently, hydrodynamics. Therefore, an exploration of the ways in which all three fields may be enriched through exchange of ideas may potentially be very rewarding.

7.3.1 Path-integral quantum mechanics

Just as polymer field theory, quantum mechanics allows two views of the world to coexist. While the more traditional quantum field theory generally dispenses with the idea of individual particles – much like FTPS – the path integral formulation shows that equivalent results may be obtained by considering individual paths of individual particles.

In the Feynman path integral formulation of quantum mechanics (QM), the probability density field of a particle position may be estimated by considering all the possible classical paths of a point particle. The action ("energy model") for such a particle is defined so that

its displacement over a small time step, τ, is normally distributed with a variance $\sim \tau$. In other words, the paths in space-time have the same statistics as a polymer of beads with ideal spring bonds.

Feynman has shown that as $\tau \to 0$, for a fixed time interval, these trajectories will sample space time according to the probability density given by the solutions to the Schrödinger's equation [22]. The equation is mathematically identical to the Fokker-Planck equation for the partition function of a Gaussian chain in a field Eq. 2.14.

The derivations of the field equations from the "particle" case are identical except for one important difference. In QM the time step τ is taken to zero in absolute terms, for a fixed total length of a trajectory in time. In contrast, this limit is only relative in the SGC model, with the bond length going to zero only relative to the size of the chain, R_g. Thus, the QM limit applies exactly to finite paths, while the SGC limit applies exactly only to infinitely long chains.

Much like FTPS, solving the Schrödinger equation in the field form is a very difficult computational problem that lead to methods based on essentially the mean field assumption or perturbation (Hartree-Fock) approaches similar to those of Helfand and Fredrickson [3]. These problems have lead to the development of computational methods based on sampling path configuration directly. Just as in polymer theory, these methods boil down to simulating bead and spring polymers using, among others, simple thermostatted molecular dynamics and Monte Carlo methods [76, 77].

7.3.2   Hydrodynamics

The differences between random walk models may, to a large extent, be in the way they represent the monomer density field in terms of the chain conformations. The idea that the a field may be approximated in many different ways – some much more convenient than others – has been explored in at least two other fields: Lagrangian (or "mesh-free") numerical methods for solving the Navier-Stokes equation [78, 79] and particle mesh-methods for solving electrostatic interactions in molecular dynamics [28]. The basic ideas of these methods are the same and generalize readily to any field theory.

Consider a model formulated in terms of a function – or a field – $\rho(x)$. Numerical calculations with this model require a discretized version of the field which may be written

as

$$\varrho(x) = \sum_i \rho_i K(x_i, x; \sigma) \tag{7.3-1}$$

where x_i are positions of a set of grid points, ρ_i is the weight assigned to grid point i (not necessarily the same as $\rho(x_i)$) and K is an interpolation kernel. An interpolation kernel here is just a probability density function in x, normalized to unity and with a standard deviation σ.

With this approximation, the field equations turn into scalar ones for grid point weights and positions. While traditional field methods fix x_i and solve only for the weights, Lagrangian methods relax this restriction and solve for grid point positions as well. Now, if f_i were fixed and only x_i allowed to vary, the grid points turn into particles. Hence, classical particles may be seen as simply a particular choice of grid points.

This statement has one important caveat that is often not recognized in the relevant literature: allowing the grid points to move as particles lead to interparticle correlations and fluctuations in local environment of each. This requires a regularization of the particle formulations to match the essentially mean-field parameters commonly used in the traditional static-grid formulations of hydrodynamic and electrostatic problems. Thus, the literature in these field may benefit from this work. At the same time, the polymer simulation community could potentially benefit from the simulation methodology that has developed in these fields.

A

Improved integrator for Langevin dynamics

In this work, an improved treatment of stochastic and friction forces in Langein dynamics was introduced. This section summarizes the algorithm.

Langevin dynamics is given the Ito SDE

$$\mathrm{d}p = -\nabla U(x)\,\mathrm{d}t - \gamma p\,\mathrm{d}t + \sqrt{2k_B T m \gamma}\,\mathrm{d}W \tag{A.0-1}$$

where p is the momentum vector of a particle, x is the position of the particle, $U(x)$ is a potential; γ is the dimensionless constant effectively determining the strength of the thermostat forces compared to the conservative forces; m is the mass of a particle, that we assume is unity in what follows; and $\mathrm{d}W$ is a three-element vector of Wiener process increments. We found that $\gamma = 0.1 - 1$ is adequate for the diblock copolymer simulations. See references [80, 81] for reviews of SDEs.

The particular choice of the strength of the random forces ensures that the system samples the canonical distribution (see [82] for a full account).

To integrate this equation numerically, at each integration step of length Δt, the αth

component of p is updated as follows

$$p_\alpha\left(\frac{\Delta t}{2}\right) \leftarrow F_\alpha \frac{\Delta t}{2} + TS(0, \Delta t/2)\Delta t \tag{A.0-2}$$

$$x_\alpha(\Delta t) \leftarrow x_\alpha(0) + p_\alpha(\Delta t/2)\Delta t \tag{A.0-3}$$

$$F_\alpha \leftarrow F(x_\alpha(t)) \tag{A.0-4}$$

$$p_\alpha(\Delta t) \leftarrow p_\alpha(\Delta t/2) + TS(\Delta t/2, \Delta t/2) \tag{A.0-5}$$

$$p_\alpha(\Delta t) \leftarrow p_\alpha(\Delta t) + F\Delta t/2 \tag{A.0-6}$$

$$TS(t, \Delta t) = e^{-\gamma \Delta t}\left(p_\alpha(t) + \eta\sqrt{mk_BT(e^{2\gamma\Delta t}-1)}\right) - p_\alpha(t) \tag{A.0-7}$$

$$F \equiv -\frac{\partial U}{\partial x_\alpha} \tag{A.0-8}$$

where η is a random number drawn out a normal distribution with mean zero and standard deviation of 1; these numbers are generated separately for each direction of particle momentum.

TS is the contribution of the friction and random thermostatting forces. This expression is the exact solution to the SDE if the potential is assumed to be constant over the time increment. The time step, Δt, must be sufficiently small for the simulation results to become relatively insensitive to its precise value.

To obtain this expression for TS, consider we consider a simplified form of the SDE

$$\mathrm{d}p = -ap\mathrm{d}t + b\mathrm{d}W$$

where a and b are constants. According to Kloeden and Platen [81] the exact solution to this equation is

$$p(\Delta t) = e^{-a\Delta t}\left(p(0) + b\int_0^{\Delta t} e^{as}\mathrm{d}W(s)\right)$$

where

$$\int_0^{\Delta t} e^{as}\mathrm{d}W(s) = \lim_{\Delta s \to 0}\sum_{j=1}^{\Delta t/\Delta s} e^{a\Delta tj}\Delta W(\Delta s) = z$$

This is a sum of Gaussian random variables with variance $\Delta s e^{2a\Delta tj}$. Therefore, z has a normal probability density with a variance obtained by evaluating the sum over j as an

integral. The result is

$$\sigma^2 = \frac{1}{2a} \left(e^{2a\Delta t} - 1 \right)$$

and

$$p(\Delta t) = e^{-a\Delta t} \left(p(0) + \eta \sqrt{\frac{b^2}{2a} \left(e^{2a\Delta t} - 1 \right)} \right)$$

where η is a normally distributed random number with variance of one and zero mean. This expression an the exact change in the momentum of a particle due to the stochastic and dissipative forces, neglecting the changes due to the conservative forces. The contribution due to these forces must be evaluated separately.

Bibliography

[1] Paul J. Flory. *Principles of Polymer Chemistry*. Cornell University Press, Ithaca, 1953.

[2] M. W. Matsen and F. S. Bates. Unifying weak- and strong-segregation block copolymer theories. *Macromolecules*, 29(4):1091–1098, 1996.

[3] Jean-Louis Barrat and Glenn H. Fredrickson. Collective and single-chain correlations near the block copolymer order-diosorder transition. *Journal of Chemical Physics*, 95(2):1281–1289, 1991.

[4] F.S. Bates, J. H. Rosedale, and G. H. Fredrickson. Fluctuation effects in a symmetric diblock copolymer near the order-disorder transition. *Journal of Chemical Physics*, 92(10):6255–6270, 1990.

[5] M. Ma, V. Krikorian, J.H. Yu, E.L. Thomas, and G.C. Rutledge. Electrospun polymer nanofibers with internal periodic structure obtained by microphase separation of cylindrically confined block copolymers. *Nano Letters*, 6(12):2969–2972, 2006.

[6] M. Ma, K. Titievsky, E.L. Thomas, and G.C. Rutledge. Continuous lamellar block copolymer nanofibers with long range order via electrospinning and confined self-assembly. *Science*, (submitted).

[7] Tao Deng, Cinti Chen, Christian Honeker, and Edwin L. Thomas. Two-dimensional block copolymer photonic crystals. *Polymer*, 44(21):6549 – 6553, 2003.

[8] A.-V. Ruzette and L. Leibler. Block copolymers in tomorrow's plastics. *Nature Materials*, 4:19–31, 2005.

[9] Robert. D. Groot and Timothy J. Madden. Dynamic simulation of diblock copolymer microphase separation. *Journal of Chemical Physics*, 108(20):8713–8724, 1998.

[10] M.W. Matsen, G.H. Griffiths, and R.A. Wickham. Monte carlo phase diagram for diblock copolymer melts. *Journal of Chemical Physics*, 124:024904, 2006.

[11] H. Fried and K. Binder. The microphase separation transition in symmetric diblock copolymer melts: A Monte Carlo study. *The Journal of Chemical Physics*, 94(12):8349–8366, 1991.

[12] G. S. Grest, M.-D. Lacasse, K. Kremer, and A.M. Gupta. Efficient continuum model for simulating polymer blends and copolymers. *J. Chem. Phys.*, 105:10583, 1996.

[13] H. Guo and K Kremer. Molecular dynamics simulation of the phase behavior of lamellar amphiphilic model systems. *J. Chem. Phys.*, 119(17):9308–9319, 2003.

[14] Ian Hamley, editor. *Developments in Block Copolymer Science and Technology.* John Wiley & Sons, 2004.

[15] Glenn H. Fredrickson. Computational field theory of polymers: opportunities and challenges. *Soft Matter*, 3(11):1329–1334, 2007.

[16] W.W. Maurer, F.S. Bates, T.P. Lodge, K. Almdal, K. Mortensen, and G.H. Fredrickson. Can a single function for chi account for block copolymer and homopolymer blend phase behavior? *Journal of Chemical Physics*, 108(7):2989 – 3000, 1998.

[17] Zhen-Gang Wang. Concentration fluctuations in binary polymer blends: Chi parameter, spinodal and Ginzburg criterion. *Journal of Chemical Physics*, 117(1):481, 2002.

[18] G.H. Fredrickson, V. Ganesan, and F. Drolet. Field-theoretic computer simulation methods for polymers and complex fluids. *Macromolecules*, 35(1):16–39, 2002.

[19] A. Yu. Grosberg and A. R. Khokhlov. *Statistical Physics of Macromolecules.* AIP Press, Melville, 1994.

[20] Eugene Helfand and Yukiko Tagami. Theory of interface between immiscible polymers. II. *Journal of Chemical Physics*, 56(7):3592–3601, 1972.

[21] L.D. Landau, E.M. Lifshitz, and L.P. Pitaevskii. *Statistical Physics, Part 1*, volume 5th of *Course of Theoretical Physics.* Butterworth-Heinman, 3rd edition, 2000.

[22] R. P. Feynman. Space-time approach to non-relativistic quantum mechanics. *Reviews of Modern Physics*, 20(2):367, 1948.

[23] M. Müller and F. Schmid. Incorporating fluctuations and dynamics in self-consistent field theories for polymer blends. *Adv. Polym. Sci.*, 185:1–58, 2005.

[24] G. H. Fredrickson and E. Helfand. Fluctuation effects in the theory of microphase separation in block copolymers. *Journal of Chemical Physics*, 87(1):697–705, 1987.

[25] T. Dotera. Tricontinuous cubic structures in abc=a=c copolymer and homopolymer blends. *Physical Review Letters*, 89(20):205502–1–4, 2002.

[26] T. Geisinger, M. Müller, and K. Binder. Symmetric diblock copolymers in thin films. II. Comparison of profiles between self-consistent field calculations and monte carlo simulations. *Journal of Chemical Physics*, 111(11):5251, 1999.

[27] K.Ch. Daoulas and M Müller. Single chain in mean field simulations: Quasi-instantaneous field approximation and quantitative comparison with Monte Carlo simulations. *Journal of Chemical Physics*, 15:184904, 2006.

[28] Roger W. Hockney and James W. Eastwood. *Computer Simulation Using Particles.* McGraw-Hill, 1981.

[29] D.R. Heine, G.S. Grest, and J.G. Curro. Structure of polymer melts and comparison of integral equation and computer simulations. *Advances in Polymer Science*, 173:209–249, 2005.

[30] K.S. Schweizer and G.C. Curro. *J. Chem. Phys.*, 91(8):5059–5081, 1989.

[31] S. F. Edwards. The statistical mechanics of polymers with excluded volume. *Proceedings of the Physical Society*, 85:613–624, 1965.

[32] A.K. Khandpur, S. Forster, F. S. Bates, I. W. Hamley, A.J. Ryan, W. Bras, K. Almdal, and Mortensen. Polyisoprene-polystyrene diblock copolymer phase diagram near the order-disorder transition. *Macromolecules*, 28:8796–8806, 1995.

[33] Mark F. Schulz, Ashish K. Khandpur, Frank S. Bates, Kristoffer Almdal, Kell Mortensen, Damian A. Hajduk, and Sol M. Gruner. Phase behavior of polystyrene-poly(2-vinylpyridine) diblock copolymers. *Macromolecules*, 29:2857–2867, 1996.

[34] D. Düchs, G.H. Fredrickson, V. Ganesan, F. Drolet, and F. Schmid. Fluctuation effects in ternary AB + A + B polymeric emulsions. *Macromolecules*, 36:9237–9248, 2003.

[35] A. J. Schultz, C. K. Hall, and J. Genzer. Computer simulation of block copolymer/nanoparticle composites. *Macromolecules*, 2005.

[36] R. B. Thompson, V.V. Ginzburg, M.W. Matsen, and A.C. Balazs. Block copolymer-directed assembly of nanoparticles: formin mesoscopically ordered hybrid materials. *Macromolecules*, 2002.

[37] G.J.A. Sevink and A.V. Zvelindovsky. Block copolymers conned in a nanopore: Pathfinding in a curving and frustrating flatland. *Journal of Chemical Physics*, 128:084901, 2008.

[38] B. Yu, B. Li, Q. Jin, D. Ding, and A.-C. Shi. Self-assembly of symmetric diblock copolymers confined in spherical nanopores. *Macromolecules*, 40:9133–9142, 2007.

[39] Eugene Helfand and Z Wasserman. Block copolymer theory. 6. cylindrical domains. *Macromolecules*, 13(4):994–998, 1980.

[40] Eugene Helfand and Z. R. Wasserman. Block copolymer theory. 4. Narrow interphase approximation. *Macromolecules*, 9(6):879–888, 1976.

[41] Eugene Helfand and Z. R. Wasserman. Block copolymer theory. 5. Spherical domains. *Macromolecules*, 11(5):960–966, 1978.

[42] K. Almdal, J. H. Rosedale, F.S. Bates, G. D. Wignal, and G.H. Fredrickson. Gaussian-to stretched-coil transition in block copolymer melts. *Physical Review Letters*, 65:1112–1115, 1990.

[43] Daan Frenkel and Berend Smit. *Understanding Molecular Simulation*. Academic Press, Inc, London, 1st edition, 2002.

[44] Hongxia Guo, Kurt Kremer, and Thomas Soddemann. Nonequilibrium molecular dynamics simulation of shear-induced alignment of amphiphilic model systems. *PHYSICAL REVIEW E*, 66:061503, 2002. Dumbell fene representation with LJ forces – very primitive. Good picture of alignment. Intuitive. Wierd shear algorithm.

[45] N. M. Maurits, A. V. Zvelindovsky, G. J. A. Sevink, B. A. C. van Vlimmeren, and J. G. E. M. Fraaije. Hydrodynamic effects in three-dimensional microphase separation of block copolymers: Dynamic mean-field density functional approach. *The Journal of Chemical Physics*, 108(21):9150–9154, 1998.

[46] Frank S. Bates, Jeffrey H. Rosedale, and Glenn H. Fredrickson. Fluctuation effects in a symmetric diblock copolymer near the order–disorder transition. *The Journal of Chemical Physics*, 92(10):6255–6270, 1990.

[47] A. Alexander-Katz, A. G. Moreira, S. W. Sides, and G. H. Fredrickson. Field-theoretic simulations of polymer solutions: Finite-size and discretization effects. *Journal of Chemical Physics*, 122:4904, January 2005.

[48] Frank S. Bates and Glenn H. Fredrickson. Conformational asymmetry and polymer-polymer thermodynamics. *Macromolecules*, 27(4):1065–1067, 1994.

[49] K. Titievsky and G.C. Rutledge. Mixtures of interacting particles with well-defined composition field coupling χ parameters. *Journal of Chemical Physics*, 128:124902, 2008.

[50] Y. Wu, G. Cheng, K. Katsov, S. Sides, J. Wang, J. Tang, G.H. Fredrickson, M. Moskovits, and G. D. Stucky. Composite structures by nano-confinement. *Nature Materials*, 3:816–822, 2004.

[51] O.N. Vassiliev and M. W. Matsen. Fluctuation effects in block copolymer melts. *Journal of Chemical Physics*, 118(16):7700–7713, 2003.

[52] M Muller and K Binder. *Macromol.*, 28:1825, 1995.

[53] M. Muller and M. Schick. Bulk and interfacial thermodynamics of a symmetric, ternary homopolymer–copolymer mixture: a Monte Carlo study. *J. Chem. Phys.*, 105(19):8885–8901, 1996.

[54] Richard M. Jendrejack, Juan J. de Pablo, and Michael D. Graham. Stochastic simulations of DNA in flow: Dynamics and the effects of hydrodynamic interactions. *Journal of Chemical Physics*, 116(17):7752–7759, 2002.

[55] K Kremer and G. S. Grest. Dynamics of entangled linear pollymer melts: A molecular-dynamics simulation. *J. Chem. Phys.*, 92:5057, 1990.

[56] A. Zirkel, S. M. Gruner, V. Urban, and P. Thiyagarajan. Small-angle neutron scattering investigation of the q-dependence of the Flory-Huggins interaction parameter in a binary polymer blend. *Macromolecules*, 35:7375–7386, 2002.

[57] M. Murat, G.S. Grest, and K. Kremer. Statics and dynamics of symmetric diblock copolymers: a molecular dynamics study. *Macromol.*, 32:595–609, 1999.

[58] E. de Miguel, E.M del Rio, and M. Telo de Gamma. Liquid—liquid phase equilibria of symmetrical mixtures by simulation in the semigrand canonical ensemble. *Journal of Chemical Physics*, 103(14):6188, 1995.

[59] Richard M. Jendrejack, Juan J. de Pablo, and Michael D. Graham. Stochastic simulations of dna in flow: Dynamics and the effects of hydrodynamic interactions. *Journal of Chemical Physics*, 116(17):7752–7759, 2002.

[60] G.S. Grest and K. Kremer. Molecular dynamics simulation for polymers in the presence of a heat bath. *Physical Review A*, 33(5):3628–3631, 1986.

[61] AJ Schultz, CK Hall, and J Genzer. Box length search algorithm for molecular simulation of systems containing periodic structures. *J. Chem. Phys.*, 120(4):2049, 2003.

[62] S.D. Bond, B.B. Laird, and B.J. Leimkuhler. On the approximation of Feynman-Kac path integrals. *J. Comp. Phys.*, 185, 2003.

[63] A.W. Lees and S.F. Edwards. The computer study of transport processes under extreme conditions. *Journal of Physics C: Solid State Physics*, 5:1921–1229, 1972.

[64] J. T. Padding and W.J. Briels. Uncrossability constraints in mesoscopic polymer melt simulations: Non-Rouse behavior of $C_{120}H_{242}$. *Journal of Chemical Physics*, 115(6):2846, 2001.

[65] W. Li, R.A. Wickham, and R.A. Garbary. Phase diagram for a diblock copolymer melt under cylindrical confinement. *Macromolecules*, 39:806–811, 2006.

[66] B. Yu, P. Sun, T. Chen, Q. Jin, D. Ding, B. Li, and A.-C. Shi. Self-assembly of diblock copolymers confined in cylindrical nanopores. *J. Chem. Phys.*, 127:114906, 2007.

[67] K. Shin, H. Xiang, S.I. Moon, T. Kim, T.J. McCarthy, and T.P. Russel. Curving and frustrating flatland. *Science*, 306:76, 2004.

[68] N. Koneripalli, N. Singh, R. Levicky, F.S. Bates, P.D. Gallagher, and S. K. Satija. Confined block copolymer thin films. *Macromol.*, 28:2897, 1995.

[69] D.G. Walton, G.J. Kellogg, A.M. Mayes, P. Lambooy, and T.P. Russel. A free energy model f o r confined diblock copolymers. *Macromolecules*, 27:6225–6228, 1994.

[70] Q. Wang. Symmetric diblock copolymers in noanopores: Monte Carlo simulations and strong-stretching theory. *JCP*, 126:024903, 2007.

[71] G.J.A. Sevink, A.V. Zvelindovsky, J.G.E.M. Fraaije, and H.P. Huinink. Morphology of symmetric block copolymer in a cylindrical pore. *JCP*, 115(17):8226–8230, 2001.

[72] Eugene Helfand. Block copolymer theory. III. Statistical mechanics of the microdomain structure. *Macromolecules*, 8(4):552–556, 1975.

[73] S. T. Milner, T. A. Witten, and M. E. Cates. Theory of the grafted polymer brush. *Macromolecules*, 21(8):2610–2619, 1988.

[74] Samuel P. Gido and Edwin L. Thomas. Lamellar diblock copolymer grain boundary morphology. 2. Scherk twist boundary energy calculations. *Macromolecules*, 27(3):849–861, 1994.

[75] Matthew S. Turner. Equilibrium properties of a diblock copolymer lamellar phase confined between flat plates. *Phys. Rev. Lett.*, 69(12):1788–1791, Sep 1992.

[76] DM Ceperley. Path integrals in the theory of condensed helium. *Reviews of Modern Physics*, 1995.

[77] S.D. Ivanov, A. P. Lyubartsev, and A. Laaksonen. Bead-fourier path integral molecular dynamics. *Physical Review E.*, 2003.

[78] Petros Koumoutsakos. Multiscale flow simulations using particles. *Annual Review of Fluid Mechanics*, 37:345–387, 2005.

[79] M. Müller, D. Charypar, and M. Gross. Particle-based fluid interaction. *Eurographics/SIGGRAPH symposium on Computer animation*, 2005.

[80] Hans C. Ottinger. *Stochastic Processes in Polymeric Fluids: Tools and Examples for Developing Simulation Algorithms.* Springer, 1995.

[81] P.E. Kloeden and E. Platen. *Numerical Solution of Stochastic Differential Equations.* Springer-Verlag, Berlin, 1992.

[82] R.L. Stratonovich. *Nonlinear Nonequilibrium Thermodynamics I: Linear and nonlinear Fluctuation-Dissipation Theorems.* Springer-Verlag, 1992.